

# **SIGNAL DESIGN AND PROCESSING TECHNIQUES FOR WSR-88D AMBIGUITY RESOLUTION**

## **Part 8: Phase Coding and Staggered PRT Data collection, implementation, and clutter filtering**

National Severe Storms Laboratory Report  
prepared by: Sebastian Torres, M. Sachidananda, and Dusan Zrnic  
with contributions by: Yannick Dubel, Svetlana Bachmann, and Valery Melnikov

November 2004

NOAA, National Severe Storms Laboratory  
1313 Halley Circle, Norman, Oklahoma 73069



# SIGNAL DESIGN AND PROCESSING TECHNIQUES FOR WSR-88D AMBIGUITY RESOLUTION

## **Part 8: Phase Coding and Staggered PRT Data collection, implementation, and clutter filtering**

### Contents

1.	Introduction.....	1
2.	Clutter filtering for SZ coded signals.....	4
2.1.	Introduction.....	4
2.2.	Filtering the ground clutter from a uniform PRT sequence.....	5
2.2.1.	Optimum window and clutter filter width selection.....	6
2.2.2.	Interpolation to restore lost signal.....	13
2.3.	The GMAP ground clutter filter.....	18
2.3.1.	How does GMAP work?.....	19
2.3.2.	GMAP Performance Evaluation.....	23
2.3.3.	GMAP and Systematic Phase Coding.....	25
a)	Window Effect.....	26
b)	Noise estimation.....	28
c)	Spectral reconstruction.....	30
d)	Filtered time series.....	33
2.3.4.	Summary of recommendations.....	35
2.3.5.	Performance comparison.....	36
3.	The SZ-2 Algorithm.....	38
3.1.	Introduction.....	38

3.2.	Clutter Filtering in the SZ-2 Algorithm .....	39
3.2.1.	Simulation description: .....	41
3.2.2.	Analyzed cases.....	42
3.2.3.	Results.....	43
3.3.	Proposed changes to the SZ-2 algorithm .....	49
3.3.1.	Incorporation of GMAP for clutter filtering .....	49
3.3.2.	Handling of clutter in any of the possible trips.....	50
3.3.3.	Optimization of the processing notch filter .....	51
3.3.4.	Addition of short-PRT spectrum width computation.....	53
3.3.5.	Refinement of censoring rules and thresholds .....	56
3.4.	The recommended SZ-2 algorithm .....	57
3.4.1.	The algorithm fundamentals .....	57
3.4.2.	Censoring rules .....	59
3.4.3.	Examples on real weather data .....	62
3.5.	Future enhancements to the SZ-2 algorithm.....	68
3.5.1.	Anomalous propagation clutter.....	68
3.5.2.	Strongly overlaid echoes.....	69
3.5.3.	Spectrum width computation .....	69
4.	Staggered PRT further results.....	71
4.1.	Evaluation using time series data.....	72
4.2.	Errors in spectral moments, experimental verification .....	85
4.3.	The generalized staggered PRT velocity dealiasing algorithm.....	88
4.4.	Effectiveness of phase coding and staggered PRT .....	89
5.	References.....	97

Appendix A.	Engineering Development and Data Collection for FY04.....	101
A.1.	Tables of VCPs .....	103
A.2.	Summary of collected data.....	108
Appendix B.	Estimates of Large Spectrum Width from Autocovariances .....	113
Appendix C.	Errata for the June 1, 2004 SZ-2 Algorithm .....	115
Appendix D.	Design, Implementation, and Demonstration of the Staggered PRT Algorithm for the WSR-88D .....	117
Appendix E.	Staggered PRT velocity dealiasing algorithm: Analysis of the velocity difference transfer function.....	119
E.1.	The Staggered PRT Technique .....	119
E.2.	Extension of the unambiguous velocity .....	120
E.3.	Analysis of the velocity difference transfer function.....	123
E.4.	Characteristics of the expected velocity difference transfer function.....	144
Appendix F.	Staggered PRT Algorithm (AEL description) .....	147



# SIGNAL DESIGN AND PROCESSING TECHNIQUES FOR WSR-88D AMBIGUITY RESOLUTION

## **Part 8: Phase Coding and Staggered PRT Data collection, implementation, and clutter filtering**

### **1. Introduction**

The Radar Operations Center (ROC) of the National Weather Service (NWS) has funded the National Severe Storms Laboratory (NSSL) to address the mitigation of range and velocity ambiguities in the WSR-88D. This is the eighth report in the series that deals with range-velocity ambiguity resolution in the WSR-88D (a complete list of reports is at the end with the references). It documents NSSL accomplishments in FY04.

The topics we report follow closely the statement of work. Thus, we start with clutter filtering in section 2. First, we examine standard spectral filters and the effects of several window functions. Interpolation of values in places of removed clutter spectrum coefficient is quantified next. Then follows an in depth analysis of Sigmet's Gaussian Model Adaptive Processing (GMAP) clutter filter. This filter has been programmed in Matlab and thoroughly evaluated.

The bulk of effort was in testing and evolving the SZ-2 algorithm into a robust, ready to deploy form. The version suggested in the 2003 Interim report had clutter filter in only the first trip. Inclusion of clutter filter for any trip required considerable testing. That is, the order of operations such as cohering, clutter filtering, recohering had to be determined for all possible cases. This required extensive simulation studies. The description and reasons for our choices are in section 3 wherein the proposed SZ-2 algorithm is also summarized. In this section, a brief

explanation backed by examples is given of the PRT effects on spectrum width measurement. Finally, we propose a few areas worth of improvement for the SZ-2 algorithm.

Section 4 discusses work on the staggered PRT algorithm. It starts with a list of ambitious tasks extracted from the FY04 statement of work and covers one by one each task. Significant are examples of spectral moment fields, verification of predicted errors, and experimental comparison of effectiveness of SZ-2 and staggered PRT in retrieving velocity fields. Generalized velocity dealiasing is briefly discussed; the reader is then referred to appendices D, E, and F for details.

After few months of idle radar (due to changes in hardware to reduce the size of components in the pedestal) we resumed data collection in February 2004. The list of collected data and volume coverage patterns are in appendix A.

Appendix B (a paper by Melnikov and Zrnić published in July 2004) deals with the limitation of measurements of spectrum width from autocovariances if the Nyquist interval is not very large compared to the spectrum width. Such is the case in surveillance scans (lowest two elevation angles) on the WSR-88D. In the legacy system mean velocity and spectrum width are not computed from long PRT (as existing in surveillance scans). Our recommendation is to utilize these spectrum widths in cases there are overlaid echoes in the Doppler (short) PRT scan. Appendix C contains a list of errata for the proposed SZ-2 algorithm described in the NSSL-NCAR report of June 1, 2004.

Appendix D (a paper by Torres et al. published in September 2004) describes a generalized staggered PRT velocity dealiasing algorithm; the interplay between maximum unambiguous velocity, dealiasing errors, and staggered ratio; and how to choose the parameters of the

staggered PRT scheme to achieve optimum results. In appendix E are the derivations of the properties of the velocity difference transfer function that allow definition of generalized dealiasing rules for any staggered PRT ratio. Finally, appendix F contains the Algorithm Enunciation Language for the staggered PRT algorithm with a DC removal in lieu of clutter filter.

## **2. Clutter filtering for SZ coded signals**

### **2.1. Introduction**

Because spectral processing is an integral part of the SZ algorithm, it is natural to remove ground clutter in the spectrum domain. Filtering clutter in staggered sequences also involves spectral processing. As a matter of fact, first steps in clutter filtering for both staggered and uniform sequences are identical. They consist of applying a window to the time series, taking a Fourier transform, and identifying the clutter spectral coefficients at and near zero velocity. Further, the operation of clutter removal (at and near zero velocity) and interpolation with estimates of weather signal may also be the same for the two techniques. The huge difference is that in the staggered PRT, clutter power spills into four additional locations from which it is removed without affecting the remaining signal components (Sachidananda et al. 1999).

Some aspects of spectral clutter filters meant for application to uniformly spaced sequences (SZ coded) have been reported earlier (Sachidananda et al. 1998 and 2002), whereas applications to staggered PRT sequences are contained in reports 3, 4, and 5 (Sachidananda et al. 1999, 2000, and 2001). Herein we deal with selection of optimum clutter filter width and the window weights, and examine ways of reducing the bias error introduced by the clutter filter in the spectral moment estimates. These aspects of clutter filtering are relevant to the SZ phase coded as well as the staggered PRT sequence processing. Furthermore, we present an in depth analysis of the GMAP filter. This filter has been accepted by NWS for uniform sequences on the WSR-88D; hence it is a natural contender for SZ phase coded sequences. Some elements from GMAP are also applicable to the initial stages of clutter removal in the staggered PRT sequence.

## 2.2. Filtering the ground clutter from a uniform PRT sequence

The ground clutter spectrum is generally very narrow and centered on the zero velocity. A typical clutter spectrum width in WSR-88D is estimated to be about  $0.28 \text{ m s}^{-1}$  for scan rates of three rpm (used at the lowest scans in VCP-11). This amounts to less than the spacing between two DFT coefficients in a 64-point DFT spectrum for a typical unambiguous velocity of  $32 \text{ m s}^{-1}$ . However, the inherent rectangular window in any finite length sample sequence spreads the clutter power over all the DFT coefficients via the side lobes of the window function. Because the side-lobes of rectangular window are fairly high, clutter suppression is poor without a weighted window. Hence, we need to apply one of the low side-lobe windows to contain the clutter power. Applying the window is equivalent to convolving the spectrum of the time series with that of the window function. This results in a lowering of the side-lobe power by concentrating the power in the main lobe, which increases the main lobe width, requiring a wider clutter filter. Thus, the clutter filter width and the window function are coupled. Another effect the window produces is the loss of power in the spectrum, and as a consequence of this the estimate variance increases. The lower the side lobe level (SLL) of the window, larger is the power loss.

An optimum choice would be a window function that suppresses the clutter spectrum side-lobes to just the level of the noise floor of the receiver, and a corresponding clutter filter width just sufficient to remove the main lobe of the clutter signal right down to the noise level. The next job would be to restore the lost weather signal components within the clutter filter bandwidth, so that the signal parameters are not unduly biased. Most serious bias happens to the mean power estimate which certainly requires to be corrected. The velocity bias happens to be small because

the weather signal and the ground clutter overlap if the mean velocity itself is near zero. The bias can be minimized by reconstructing the lost signal components by some type of interpolation from the remaining signal coefficients. These aspects are discussed in the following section.

### 2.2.1. *Optimum window and clutter filter width selection*

In weather radar, the clutter-to-noise ratio (CNR) has a large dynamic range (it can be as large as 100 dB). To filter the ground clutter effectively we need to select an appropriate window and a clutter filter width. Although the spectrum width of the clutter is narrow for the normal scan rates (median width for the ground clutter in WSR-88D is estimated to be about  $0.28 \text{ m s}^{-1}$ ), the inherent rectangular window in any finite length sample sequence spreads the clutter power to the entire spectrum. This can be contained by applying a window function with an edge taper to lower the SLL. The rectangular window has the narrowest main lobe and very high side lobes, whereas the window functions with edge taper have lower side lobes, but wider main lobes. Therefore, for a given CNR, we need to apply a window function with a SLL the same as the CNR so that the clutter spectrum side lobes are suppressed to the noise level, and then apply a clutter filter with a width corresponding to the main lobe of the clutter signal. Thus, the optimum combination is dependent on the CNR. The ground clutter spectrum width is much narrower than the main lobe of the window spectrum; therefore, if the window is applied the spectrum would have a width similar to or slightly wider than the window's main lobe.

Two important considerations in determining an optimum window for a given situation are the SLL of the window function and the loss associated with it. While the SLL determines the maximum filterable CNR the loss increases the variance of the estimates. Lowering the SLL not only produces higher loss, it also increases the main lobe width requiring a wider clutter filter.

As the width of clutter filter increases, the bias error due to the signal loss within the clutter filter also increases. Therefore, an optimum combination of the window and clutter filter width would be a window whose SLL is same as CNR (to minimize the loss and filter the clutter efficiently), and clutter filter width which matches the main lobe of the clutter spectra. Further, the window function should have the minimum width for the given SLL.

Another minor point to note is that for small number of samples,  $M$ , the SLL is also dependent on the sequence length; it becomes independent only for large  $M$ . Smaller  $M$  results in a slightly higher SLL. This point has some relevance in the context of the ground clutter filtering from the long PRT transmission sequence ( $M$  is about 17). Here, we examine several windows for a sequence length of 64, which is about the maximum number of samples available in the Doppler mode. We pick a few of the low side lobe windows for the present application. In Fig. 2.1 is discrete spectrum of simulated ground clutter with a spectrum width,  $w_c = 0.28 \text{ m s}^{-1}$ . The windows applied are the von Hann, Blackman, and Chebyshev (80 dB and 100 dB). The spectrum with rectangular window (no window applied) is also shown for comparison. The numbers indicated in brackets are losses associated with the window in dB. In the DFT domain, the clutter filter width can only be in terms of the DFT coefficients, hence, we have shown DFT coefficient (index) along the x-axis; index 1 corresponds to zero Doppler. In terms of the DFT coefficients, the clutter filter width is  $n_c = 2q-1$ . The numbers shown on the x-axis can be treated as the  $q$  values; i.e., if we need to filter a clutter with CNR = 40 dB, we choose either von Hann, Blackman, or Chebyshev(80) window and delete the first 4 and last 3 DFT coefficients (not shown on the figure).

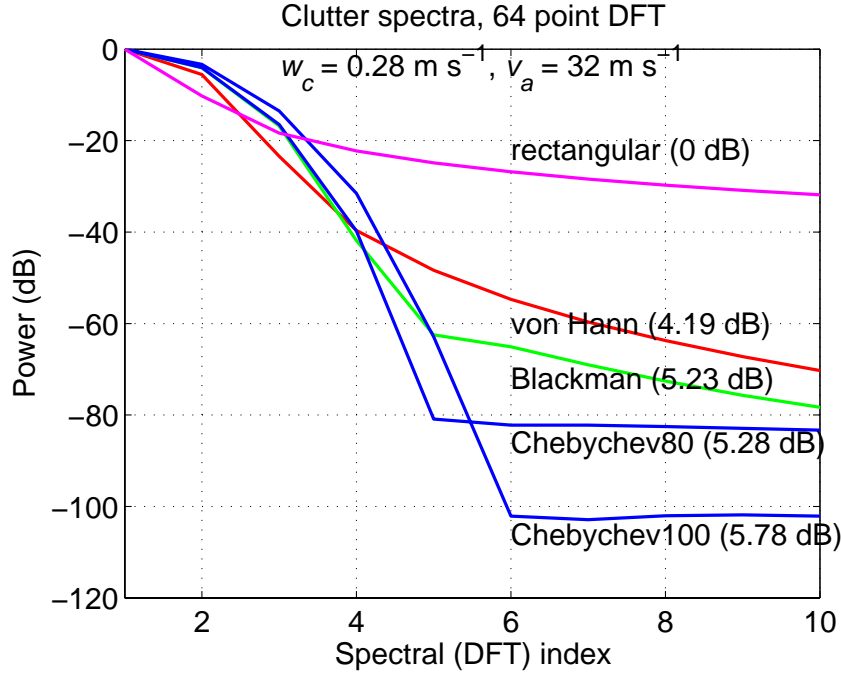


Fig. 2.1. Simulated clutter spectrum. The window functions applied to the time series prior to the Discrete Fourier Transform (DFT) are indicated and losses associated with each window are in parentheses. The total number of points in the DFT,  $M = 64$ . Only region within the main lobe and few near sidelobes is depicted and discrete spectral points are connected for visual clarity.

From Fig. 2.1 we observe that if the  $\text{CNR} = 10 \text{ dB}$ , we are better off with a rectangular window. A clutter filter width  $n_c = 3$  ( $q = 2$ ) is sufficient. The rectangular window has 0 dB loss; hence the estimate variances are the lowest possible for a given number of samples. If we apply von Hann window to this case, we need  $n_c = 5$  to filter the ground clutter. This will incur 4.23 dB loss as well as a larger bias due to increased  $n_c$ . If we consider a case of  $\text{CNR} = 60 \text{ dB}$ , then from Fig. 2.1 the choice would be Blackman window and  $n_c = 9$  ( $q = 5$ ). To get the same suppression using von Hann window we would require  $n_c = 13$  ( $q = 7$ ).

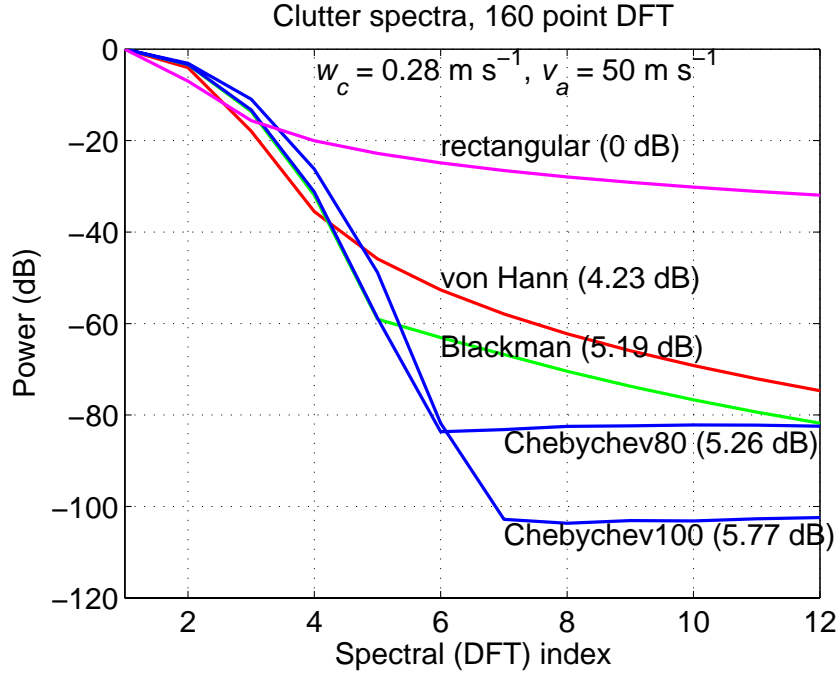


Fig. 2.2. Same as in Fig. 2.1 except the number of DFT points is  $M = 160$ .

As noted earlier, the main lobe width of the window is also a function of the number of samples if  $M$  is small. For large  $M$ , the main lobe widening effect can be neglected. In the staggered PRT sequence, processing is done on the derived time series (see Sachidananda et al. 1999) whose length is much larger than the number of samples (for example, with  $T_1 / T_2 = 2/3$ ,  $N = 5M/2$ ). Fig. 2.2 is similar to Fig. 2.1 but for 160 point DFT corresponding to the 64 staggered PRT sample sequence. It can be seen that the main lobes for all the window functions shown are more or less same, but the *knee* points from where the side lobe envelope starts are different. The knee points are indicative of the effective maximum clutter suppression possible with that window. Increasing the clutter filter width beyond this point will not be very effective. The knee points are: -101dB, -81dB, -58dB, -35dB, and -15dB, for the Chebyshev(100), Chebyshev(80), Blackman, von Hann, and the rectangular windows, respectively. The corresponding clutter filter

widths,  $n_c/N$ , are: 13/160, 11/160, 9/160, 7/160, and 3/160, in the same order. Note that if we select a filter width of 13/160, the clutter suppression available with different windows are: 101 dB, 81 dB, 66 dB, 57 dB, and 26 dB, for the Chebyshev(100), Chebyshev(80), Blackman, von Hann, and the rectangular windows, respectively.

With respect to the optimality criteria delineated earlier in this section, of all the windows, a Chebyshev window with a knee point equal to the CNR is an optimum window. The Chebyshev window has the optimum property that its main lobe is the narrowest for a given SLL (all side lobes are of equal height), hence, has the lowest loss too. However, the statement regarding the loss part is valid only for low side lobe values.

Fig. 2.3 shows the performance of the Chebyshev windows with different knee points (for  $N = 160$ ). The corresponding loss factors are shown in brackets. Note that for SLL = 20 dB, the loss is much larger than for lower SLL levels! The reason for this is that if the SLL is large the weights at the edge start increasing, which is undesirable in practice. Only for low SLL the edge distribution has the required taper. In Fig. 2.4, the window loss is shown as a function of the SLL of the Chebyshev window for three different sample sequence lengths,  $M = 32, 64$  and 160. It can be seen that for  $M = 160$ , the loss abruptly starts increasing below SLL = 35 dB. Therefore, we can use Chebyshev window only for CNR > 35 dB (the lower limits are 30 dB for  $M = 64$ , and 25 dB for  $M = 32$ ).

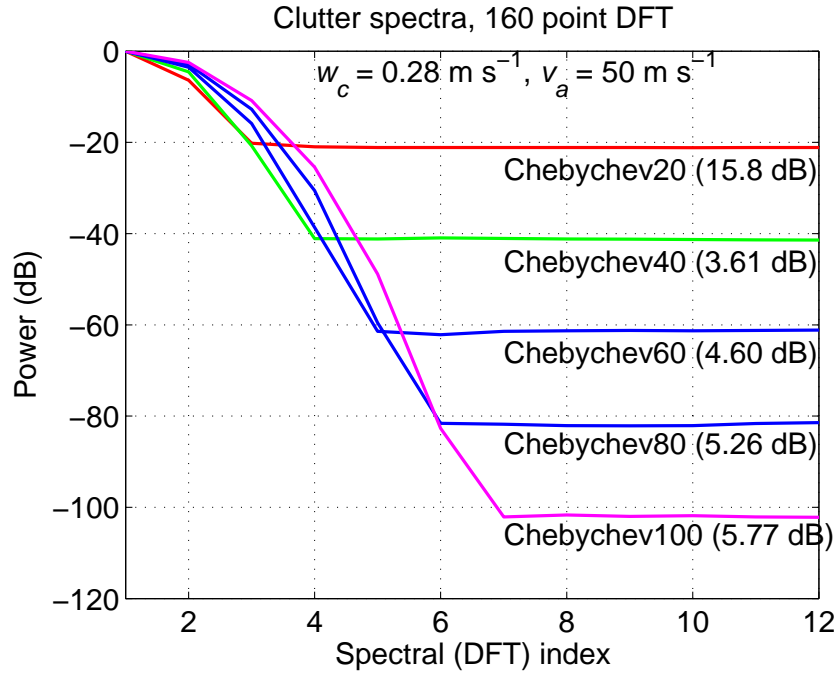


Fig. 2.3 Similar to Fig. 2.2 except the applied window functions are of the Chebyshev type as indicated.

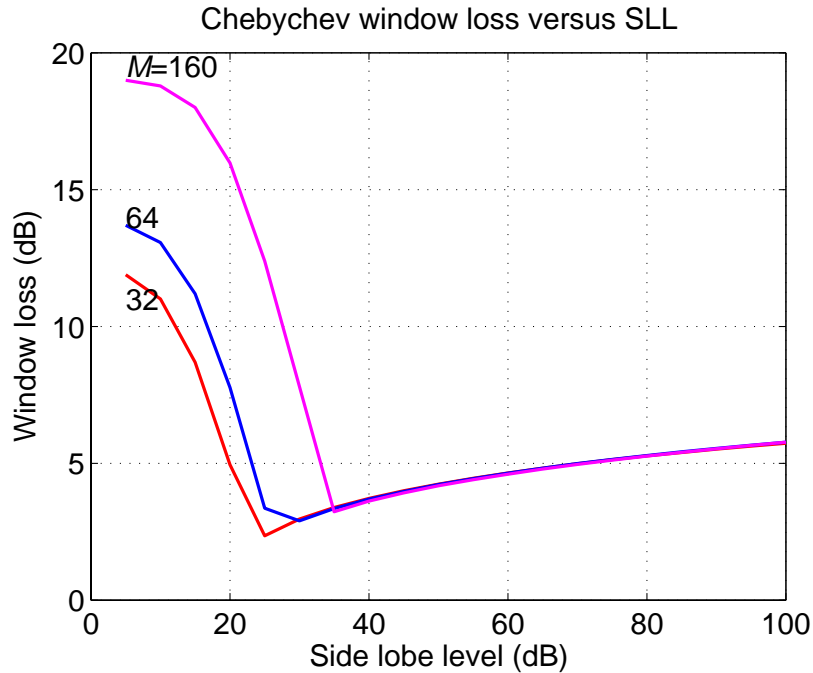


Fig. 2.4. The variation of window loss factor versus the side lobe level (SLL) for the Chebyshev windows. The number of DFT coefficients is a parameter.

In the following, we have prepared a table which gives optimum combinations of the window and filter widths. Because in practice the clutter filter width is in terms of the DFT coefficients, we have given  $q$  and the range of CNR values. It must be emphasized that this is optimum with respect to the criteria explained earlier. (Read the discussion later in this section for other criterion.)

**Table. 2.1.** Optimum window selection table for  $M = 64$  and  $160$ .

$w_c = 0.28$ m/s, $M = 64$ , $v_a = 32$ m/s			$w_c = 0.28$ m/s, $M = 160$ , $v_a = 50$ m/s		
$q$	window type	CNR range in dB	$q$	window type	CNR range in dB
2	rect (no window)	< 10	2	rect (no window)	< 4
3	von Hann	$10 < \text{CNR} < 25$	3	von Hann	$4 < \text{CNR} < 15$
4	von Hann	$25 < \text{CNR} < 40$	4	von Hann	$15 < \text{CNR} < 35$
5	Chebyshev (CNR)	$40 < \text{CNR} < 60$	5	Chebyshev (CNR)	$35 < \text{CNR} < 60$
6	Chebyshev (CNR)	$60 < \text{CNR} < 100$	6	Chebyshev (CNR)	$60 < \text{CNR} < 80$
7			7	Chebyshev (CNR)	$80 < \text{CNR} < 100$

From the Table 2.1, it is clear that if appropriate window is selected, the maximum clutter filter width needed is limited to  $q/M = 6/64$  and  $7/160$  for  $\text{CNR} < 100$  dB. Note that the Blackman window is good up to  $\text{CNR} = 60$  dB so it is almost equivalent to the Chebyshev(60). If one opts for Blackman window up to the  $\text{CNR} = 60$  dB, the clutter rejection would be fine but signal loss would be less than optimum. The von Hann window is good up to  $\text{CNR} = 40$  dB only. Note that the normalized clutter filter width ( $n_c/M$ ) is much narrower for larger  $M$ .

All the foregoing discussion on the ground clutter filtering is based on the assumption that we need to filter the clutter right down to the noise floor of the receiver. This is a theoretical optimality criterion without taking the weather signal into consideration. In fact, our main

purpose is to estimate the weather signal parameters accurately; ground clutter filtering is only an issue in the process. With this standpoint, the optimality criteria also changes; the signal-to-clutter ratio (SCR) becomes important and not the CNR. By filtering the ground clutter we can improve the SCR. With increasing clutter filter width, the SCR improves but not necessarily the weather signal parameter estimates. Depending on the signal parameters, especially the velocity, there is an optimum filter width beyond which the estimate accuracy starts degrading, both in terms of bias and variance. The bias error is a strong function of the overlap of the ground clutter and the weather spectra, whereas, the variance degradation is a function of the window loss. It is difficult to determine the optimum  $n_c$  without knowing the signal parameters. If the weather and the clutter spectra do not overlap then the optimum window and  $n_c$  indicated in Table.2.1 are best choices; however, if there is an overlap, then we need to consider the SCR in determining the clutter filter width as well as the window function.

### 2.2.2. *Interpolation to restore lost signal*

In the spectral domain clutter filtering we delete  $n_c$  DFT coefficients centered on the zero Doppler (or the DFT coefficient # 1); this also deletes all the signal power present in these coefficients. Whenever the signal velocity is near zero, the ground clutter and the weather signal overlap in the spectral domain, and filtering the clutter also removes the weather signal components within the clutter filter width. This produces a bias in the spectral parameter estimates. Although the error in the velocity is small, the bias in the mean power estimate is significant, and needs to be corrected.

One of the methods to restore the signal components is to extrapolate from the unfiltered signal coefficients. Specifically, an approach that gave reasonably good results in a simulation

experiment is a linear interpolation of the spectral power between the two coefficients just outside the clutter filter. If the ground clutter filter width,  $n_c = (2q-1)$ , the first  $q$  and the last  $(q-1)$  coefficients would be deleted by the clutter filter, hence, we take  $(q+1)^{\text{th}}$  and  $(M-q+1)^{\text{th}}$  coefficients and assume that the spectral power varies linearly between these two. This is a very simplistic interpolation, but works well as long as the deleted spectral coefficients are on one side of the Gaussian shaped weather signal spectra. The error becomes significant only if the filter removes the peak of the signal spectrum. One could also fit a Gaussian shape to the residual signal components (such as done by the GMAP), but this involves a lot more computations. This performs slightly better if the peak of the signal spectra is deleted by the clutter filter, but for other cases, the difference in the performance between Gaussian interpolation and the linear interpolation is marginal.

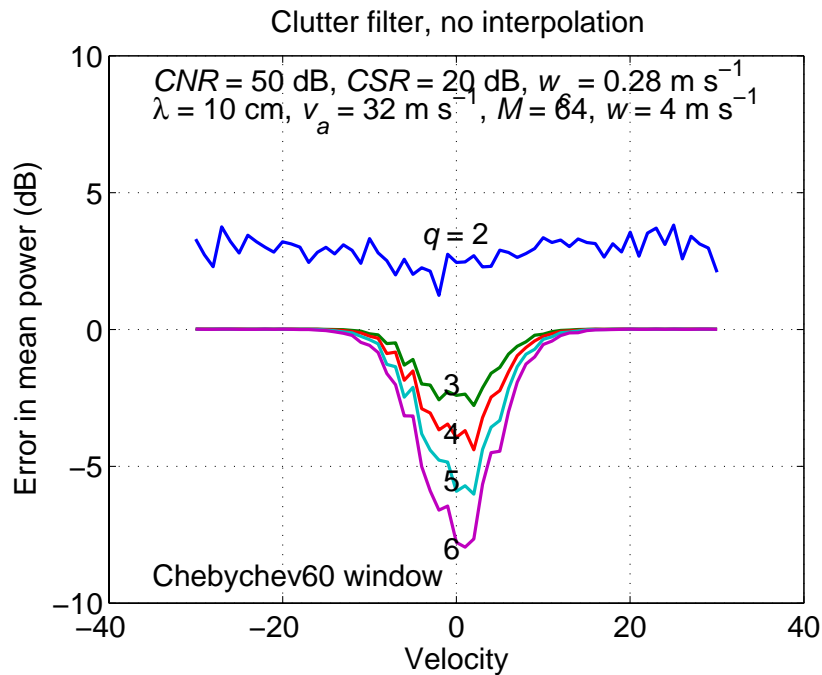


Fig. 2.5.a. Bias errors in the mean power estimate versus velocity for different clutter filter widths.

Figs 2.5a, 2.5b, and 2.5c show the bias error in the three spectral moment estimates as a function of the velocity generated using simulated time series. No interpolation is used to restore the lost signal components. For this simulation we have used  $CNR = 50\text{dB}$ , and  $SCR = -20\text{ dB}$ . The other parameters used in the simulation are indicated in the figure. The curves are an average of 20 simulations at each velocity. The  $q$  values indicate the clutter filter width ( $n_c = 2q-1$ ). For  $|v|$  larger than about  $10\text{ m s}^{-1}$  the bias is independent of  $q$  because the weather and the ground clutter spectra do not overlap. From Fig. 2.5a, it is seen that  $q = 2$  is not sufficient to filter the clutter as seen by the nearly 3dB bias error independent of the velocity. A wider filter with  $q = 3$  is sufficient to filter the clutter as there is no bias when there is no overlap ( $|v| < 10\text{ m s}^{-1}$ ). The window has been judiciously chosen as Chebyshev(60). In this case  $q = 3$  is the best choice; it produces the lowest bias. Note that this width is less than that indicated in the table 2.1 for  $CNR = 50\text{ dB}$ . This is because the  $SCR$  is  $-20\text{ dB}$ , and  $q=3$  produces a  $SCR > 3\text{dB}$  after the ground clutter is filtered. With a further increase in the clutter filter width, the bias error increases.

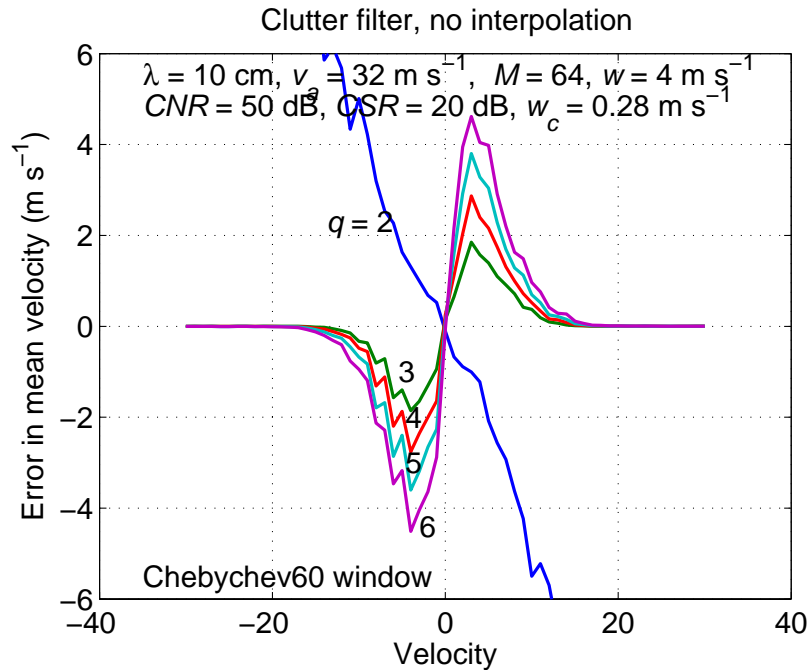


Fig. 2.5.b. Bias errors in the mean velocity estimate.

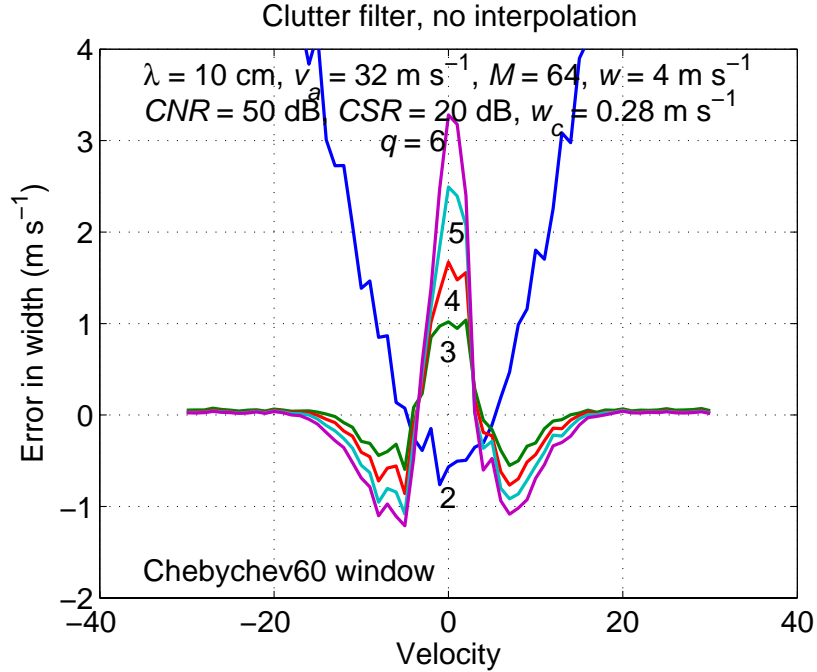


Fig. 2.5.c. Bias errors in the mean spectrum width estimate.

The next set of figures (Fig. 2.6a, 2.6b, and 2.6c) show the bias errors in the mean power, the mean velocity, and the spectrum width estimates after linear interpolation of the signal coefficients within the clutter filter width. All the simulation parameters are the same as in the previous case. Comparing these two sets of figures it is clear that most of the bias is removed by interpolation. For the optimum filter width,  $q = 3$ , the bias error in the mean power is about 0.5 dB only. Even for the widest clutter filter ( $q = 6$ ) the maximum bias is about 3 dB. This is just one example with  $CNR = 50$  dB. In most cases the optimum clutter filter width required is dictated by the SCR and the velocity. The bias error in the mean power estimate is significant only near zero velocity. Similar effects can also be seen in the other two parameters. With the selection of an optimum window and clutter filter combination, the linear interpolation approach is sufficient to estimate the spectral parameters within the acceptable error bounds.

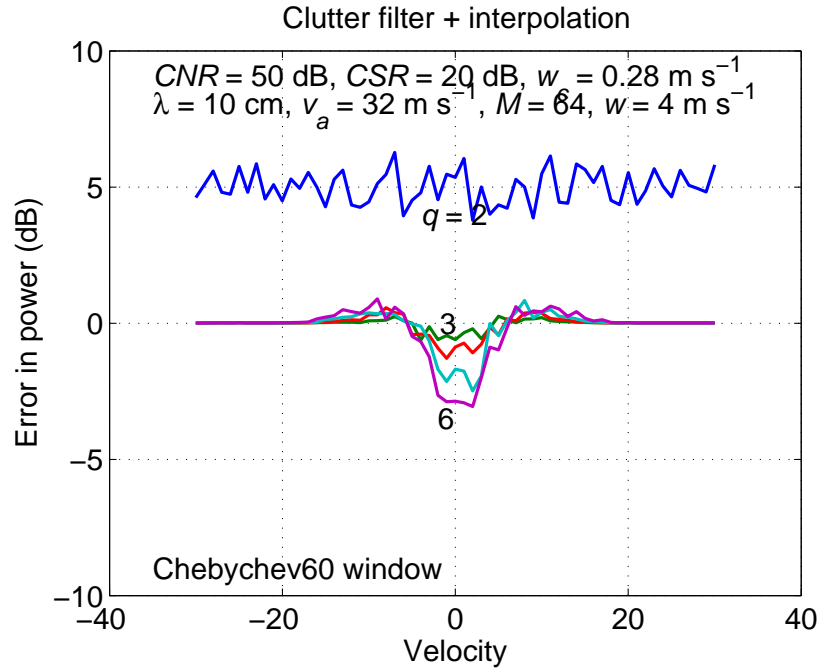


Fig. 2.6.a. Bias errors in the mean power estimate versus velocity for different clutter filter widths. Linear interpolation was used to restore signal spectrum within the clutter filter.

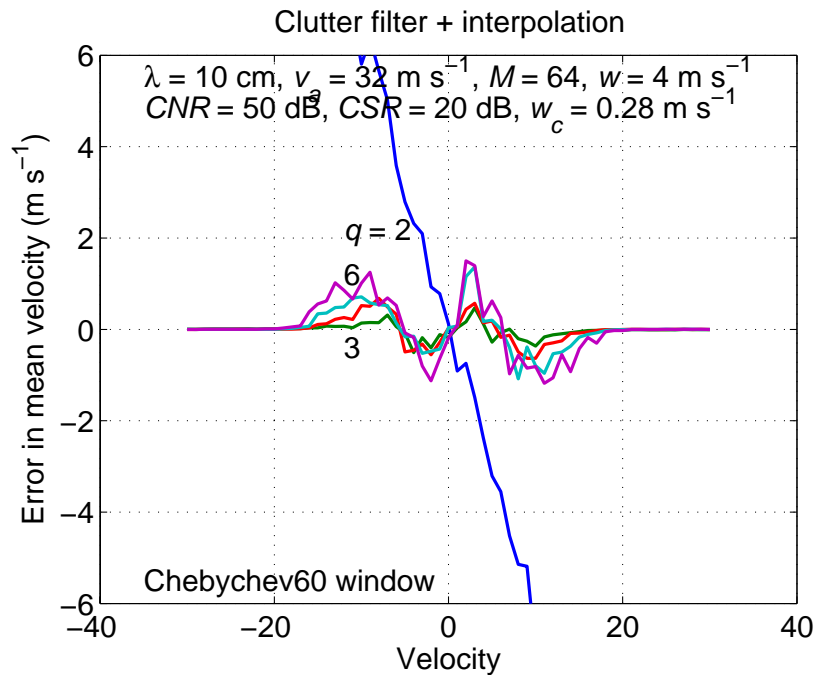


Fig. 2.6.b. Bias errors in the mean velocity. Linear interpolation was applied.

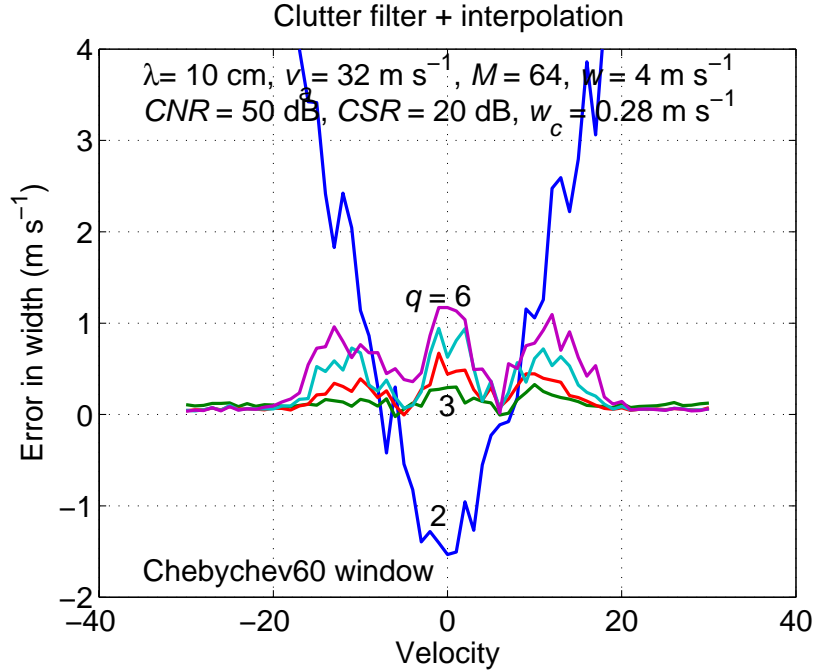


Fig. 2.6.c. Bias errors in mean spectrum width for the same conditions as in 2.6a and b.

### 2.3. The GMAP ground clutter filter

The Gaussian Model Adaptive Processing (GMAP) ground clutter filter was developed by SIGMET for the Open RDA (ORDA) as an alternative to the legacy RDA 5<sup>th</sup>-order elliptic filter. Ice et al. (2004) evaluated this filtering scheme through simulations and determined that GMAP meets or exceeds all performance requirements for the WSR-88D system and hence should be used in the upcoming ORDA. At the same time, studies by NSSL and NCAR determined that the legacy RDA ground clutter filter (as well as almost any other IIR filter) introduces a phase distortion that, without correction, impairs the performance of systematic phase coding for the mitigation of range and velocity ambiguities (Zrníc et al. 2003). Tasking for this year included the evaluation of ground clutter filtering schemes that are compatible with systematic phase

coding. The focus was primarily on GMAP, since this is the only ground clutter filter that will be initially available in the ORDA.

Aside from the notes and comments scattered throughout the SIGMET RVP8's source code, no written documentation of GMAP existed until late in FY04 (Siggia and Passarelli 2004). Initial efforts dealt with understanding GMAP from the source code provided by SIGMET, and accurately porting that code into MATLAB in order to test it with both simulated and real weather data. The results of these tests are presented herein after a brief review of the basic principles behind GMAP.

### 2.3.1. *How does GMAP work?*

The following is a brief description of the basic ideas in the GMAP algorithm as implemented in release RVP8 RDA 8.04 dated November 4, 2003. For a more detailed analysis the reader is referred to Siggia and Passarelli (2004).

Inputs to the ground clutter filter are (1) the power spectrum of the time-series data (obtained after windowing), (2) the noise level (this is an optional parameter), and (3) the expected spectrum width of ground clutter. After processing, GMAP returns (1) the power spectrum of the filtered time-series data, and (2) the amount of power removed in the filtering process. The basic steps of the algorithm are (1) noise power computation, (2) clutter filtering, (3) spectral reconstruction, and (4) computation of removed power; these are discussed next.

If the noise level is not provided to GMAP, a rank-order technique is used to dynamically estimate the noise level from the data. First, the spectral components are sorted according to their magnitude. As shown in Fig. 2.2.1, this distribution is compared with the theoretical curve for

white noise, and the spectral component at which the curves begin to diverge from each other is selected as the boundary between “noise” and “signal” (or “signal plus clutter”) components. Finally, spectral components labeled as “noise” are used to compute the noise power.

A Gaussian clutter model is generated based on the expected ground clutter spectrum width and the actual power in the three central spectral components. The notch width (or “gap”) is determined from this model such that all components that fall within the Gaussian curve are removed.

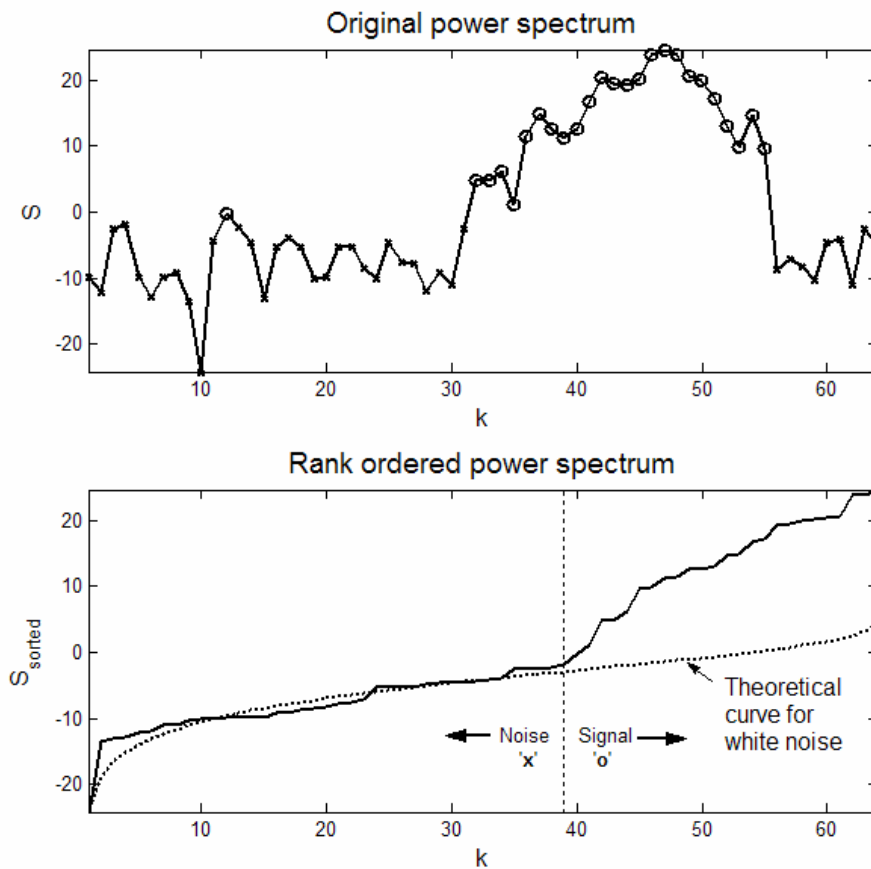


Fig. 2.2.1. Noise power computation using the rank-order technique. (top) Original power spectrum with spectral components labeled as “noise” (‘x’ marker) or “signal” (‘o’ marker). (bottom) Rank-ordered power spectrum and theoretical curve for white noise.

After all clutter components are removed, the algorithm attempts to reconstruct the “signal” spectrum within the gap. An iterative algorithm uses a signal model (generated from estimates of the mean Doppler velocity and spectrum width) to reconstruct the signal within the gap until the spectrum converges within predetermined levels of errors.

Finally, the reconstructed or filtered spectrum is subtracted from the original spectrum to obtain the amount of power removed by the filtering process.

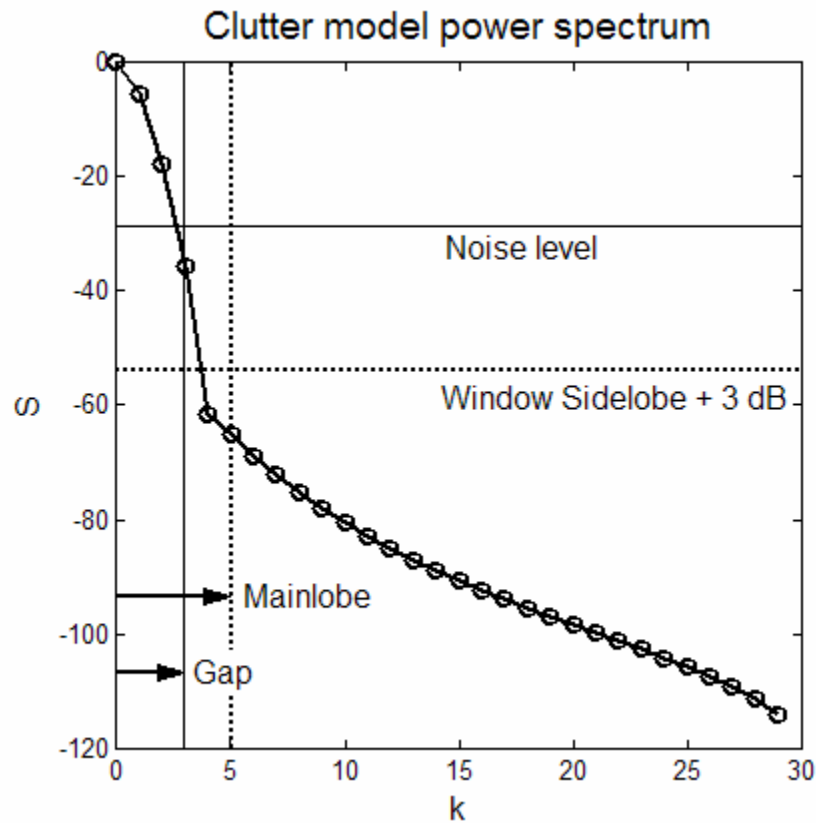


Fig. 2.2.2. Determination of clutter notch width (or gap) from clutter model and noise level. The upper bound for the gap is dictated by the width of the main lobe which depends on the window used to compute the original power spectrum.

Fig. 2.2.3 shows the performance of GMAP using simulated data. A GMAP analysis tool that uses the ported RVP8 code was developed in MATLAB for this purpose. The tool simulates signals consisting of a weather signal, ground clutter, and noise; applies the GMAP clutter filter; and finally estimates the first three spectral moments (power, Doppler velocity, and spectrum width). The user can control all signal parameters including the choice of window and number of samples. This has proven to be a convenient exploratory tool to study the GMAP filter.

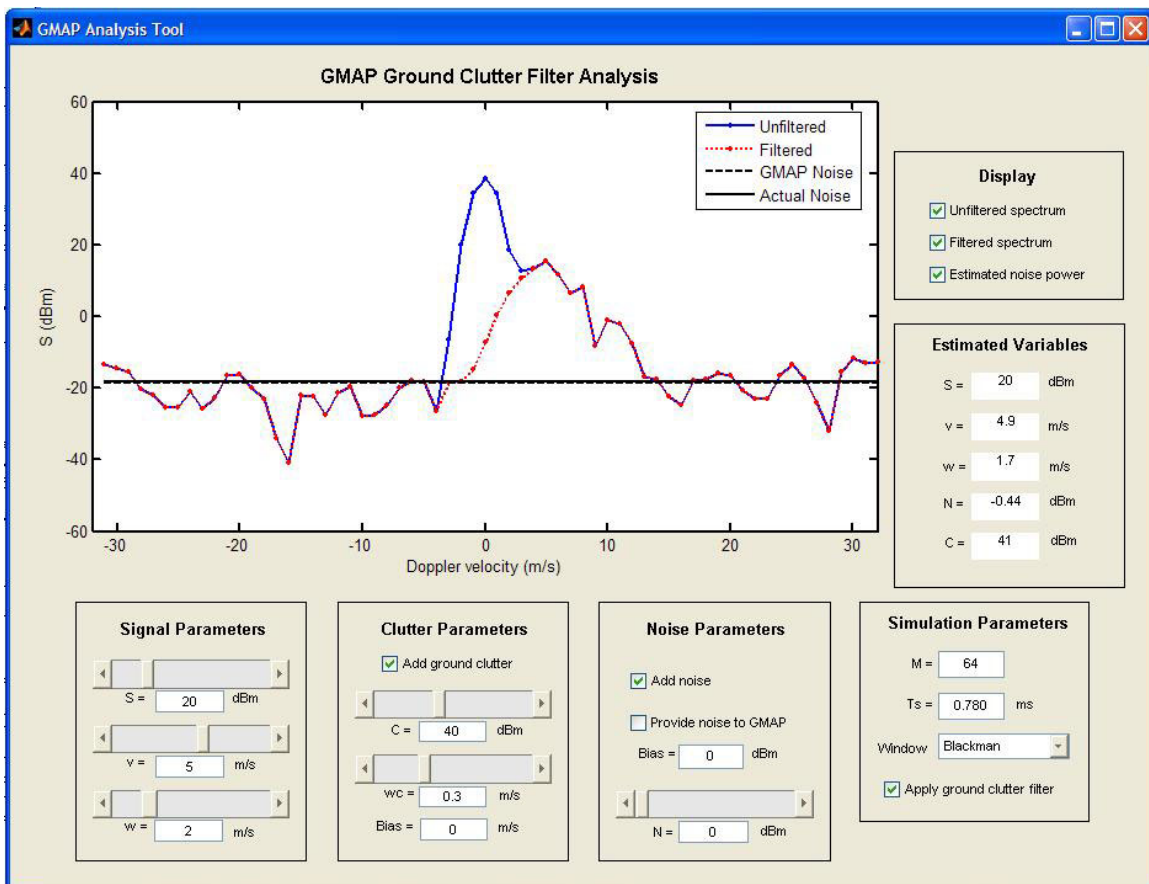


Fig. 2.2.3. GMAP analysis tool screen capture.

### 2.3.2. GMAP Performance Evaluation

As expected, GMAP performs better for large number of samples ( $M$ ). As  $M$  decreases, the noise estimation algorithm breaks down, and it becomes imperative to bypass this step by providing the noise level to the algorithm. Hence, an accurate measurement of the noise level during the calibration stage is required for effective GMAP performance.

It was demonstrated by Ice et al. (2004) that an aggressive window is essential to achieve the required clutter suppression levels. Whereas the Blackman window meets these requirements, it also produces the smallest equivalent number of independent samples, inducing larger errors of estimates.

One of the most attractive features of GMAP is its ability to reconstruct the spectrum of the signal after clutter filtering (see red curve in Fig. 2.2.3). In the presence of ground clutter, the spectral reconstruction minimizes estimators' biases due to clutter filtering for signals with near-zero Doppler velocities. However, if applied in the absence of ground clutter, GMAP may still filter some spectral components and the final signal spectrum could become significantly distorted (Fig. 2.2.4 shows an example of this detrimental effect). In such cases, GMAP falsely indicates that ground clutter power was removed by returning a positive value for the “removed power” ( $P_{REM}$ ).

A simulation was designed to establish the suitability of  $P_{REM}$  as an estimate of clutter power. GMAP was driven with time series composed of (a) a weather signal with Doppler velocity anywhere in the Nyquist range and spectrum width of 1, 2, 4, and 8  $\text{m s}^{-1}$ , (b) a ground clutter signal with clutter-to-signal ratio (CSR) from -30 to 50 dB and a spectrum width of 0.3  $\text{m s}^{-1}$ , and (c) additive white noise with a clutter-to-noise ratio greater than 20 dB in all cases.  $P_{REM}$  was

recorded for 1000 realizations of each set of signal parameters;  $P_{REM}$  was set to zero if no power was removed or if GMAP “added” power in the clutter filtering process.

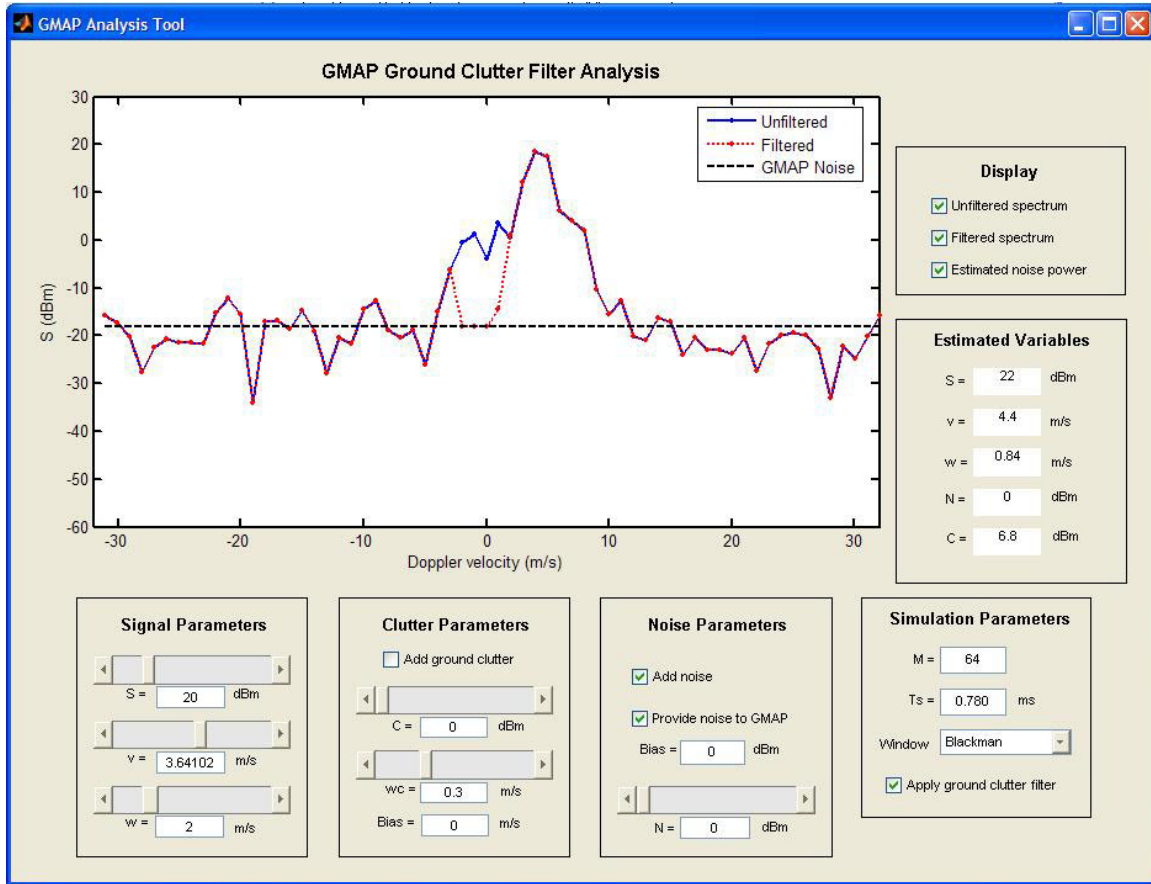


Fig. 2.2.4. An example of GMAP distorting a ground-clutter-free spectrum

Fig. 2.2.5 shows the results of this simulation. It is evident from these plots that GMAP’s  $P_{REM}$  can be used as an estimator of ground clutter power for medium to large CSR ( $> 0$  dB). However,  $P_{REM}$  is considerably unreliable (i.e., exhibits large bias and standard error) as an estimate of ground clutter power for low CSR ( $< 0$  dB). These results were of considerable importance in the design of the SZ-2 algorithm since they establish the limits under which GMAP can be used as an indicator of ground clutter.

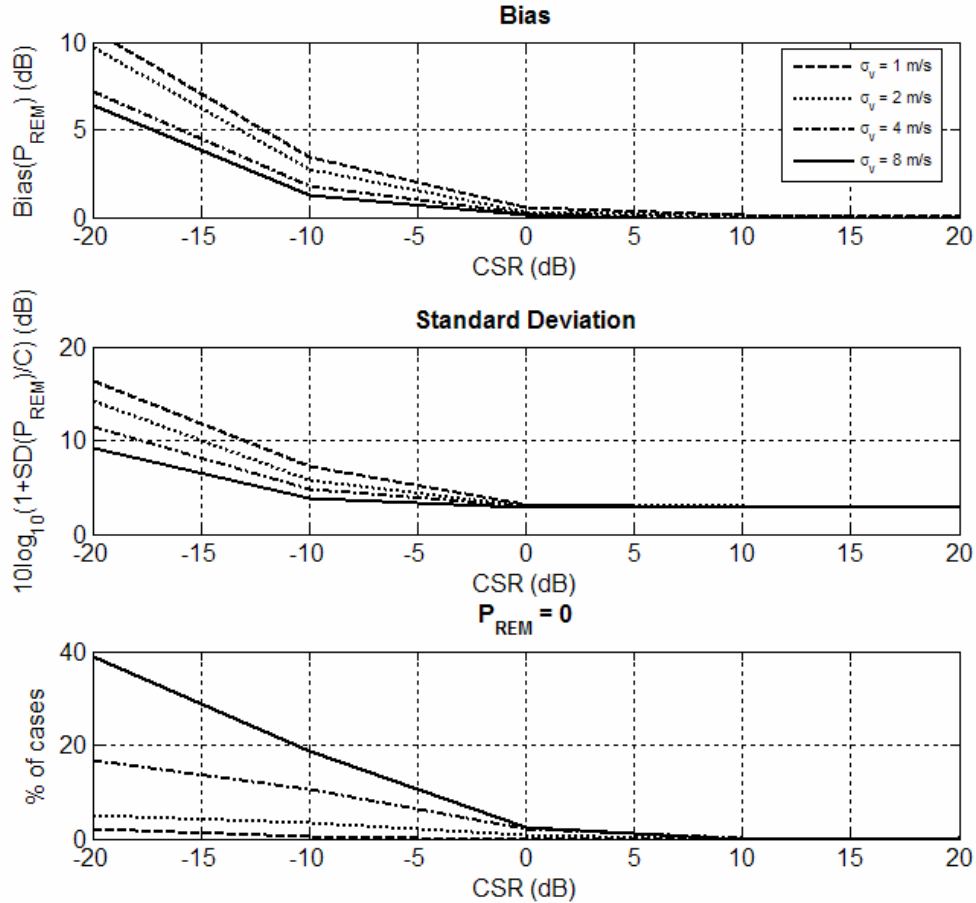


Fig. 2.2.5. Simulation results for the evaluation of GMAP's  $P_{REM}$  as an estimator of ground clutter power. Data was simulated with  $M = 64$ ,  $CNR > 20$  dB, Blackman window, and 1000 realizations per point.

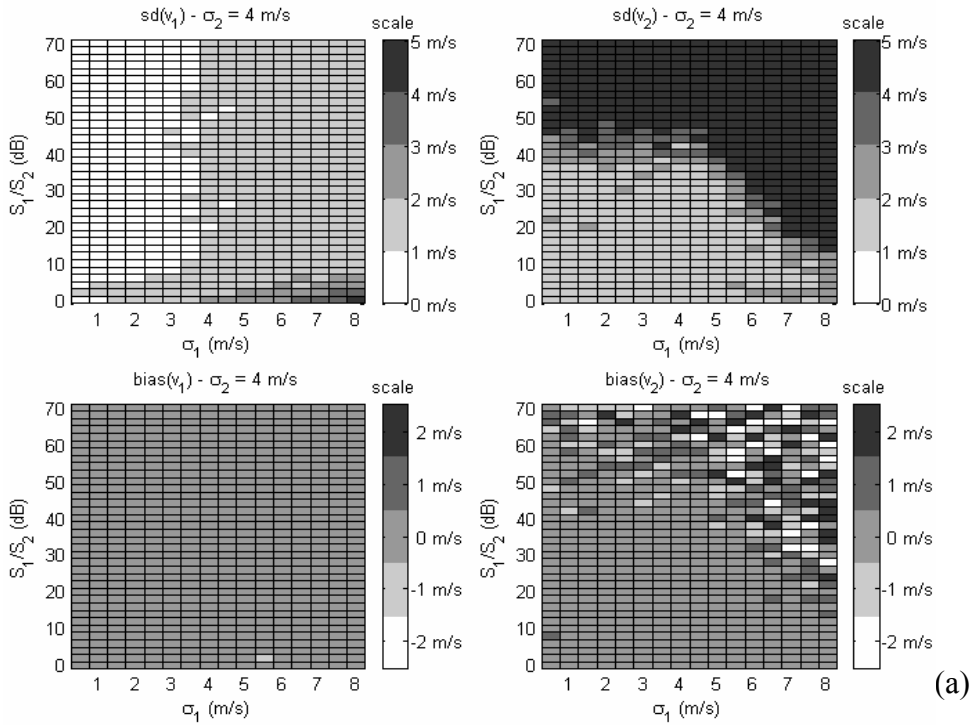
### 2.3.3. GMAP and Systematic Phase Coding

Originally, GMAP was designed for uniformly sampled signals (uniform PRT) with no phase coding. Hence, it is important to establish whether this filter can be used within the systematic phase coding scheme. As opposed to IIR filters like the ones used in the legacy RDA, spectral filters like GMAP do not introduce a phase distortion. As demonstrated in previous reports, this is critical for phase coded signals because the phase information is needed to reconstruct (recohere) the weak-trip spectrum. In what follows, four issues pertaining to the implementation of GMAP in the context of systematic phase coding are discussed.

**a) Window Effect**

In NSSL Report 2 (1998) Sachidananda et al. recommended using the Von Hann window as a way to reduce contamination of signals by clutter residues in the window sidelobes and minimize the standard error of estimates when processing phase coded signals. On the other hand, Ice et al. (2004) determined that required ground clutter suppression levels can only be achieved by GMAP if the time series data are processed with the Blackman window. It is expected that a more aggressive window will cause an increase in errors of estimates because the equivalent number of independent samples is reduced by the window. A simulation was developed to quantify this effect in the context of SZ phase coding. Simulated time series data consist of weather signals in the 1<sup>st</sup> and 2<sup>nd</sup> trips with 64 samples; clutter is not added and the SNR is very large. Simulated signal powers are such that the power ratio  $S_1/S_2$  varies from 0 to 70 dB and velocities are random within the Nyquist interval. The spectrum width of the 1<sup>st</sup>-trip signal ( $\sigma_1$ ) varies from 0.5 to 8 m s<sup>-1</sup>; the 2<sup>nd</sup>-trip signal spectrum width ( $\sigma_2$ ) is fixed in succeeding experiments at 1, 2, 4, and 8 m s<sup>-1</sup>. Time series are windowed with either the Von Hann or the Blackman window and processed via a simple version of the SZ-2 algorithm. Estimates of 1<sup>st</sup>- and 2<sup>nd</sup>-trip velocities are recorded for 100 realizations of each set of parameters. Fig. 2.2.6 shows the statistics (standard deviation and bias) of 1<sup>st</sup> trip and 2<sup>nd</sup> trip velocities ( $v_1$  and  $v_2$ ) for  $\sigma_2 = 4$  m s<sup>-1</sup> using (a) the Von Hann window and (b) the Blackman window. Whereas both windows produce the same performance in terms of bias, as expected, the Von Hann window exhibits better performance in terms of standard errors. This performance deterioration should be considered in the choice of the window within GMAP for application in the SZ-2 algorithm.

**SZ-2 Algorithm - No Clutter, Von Hann Window**



**SZ-2 Algorithm - No Clutter, Blackman Window**

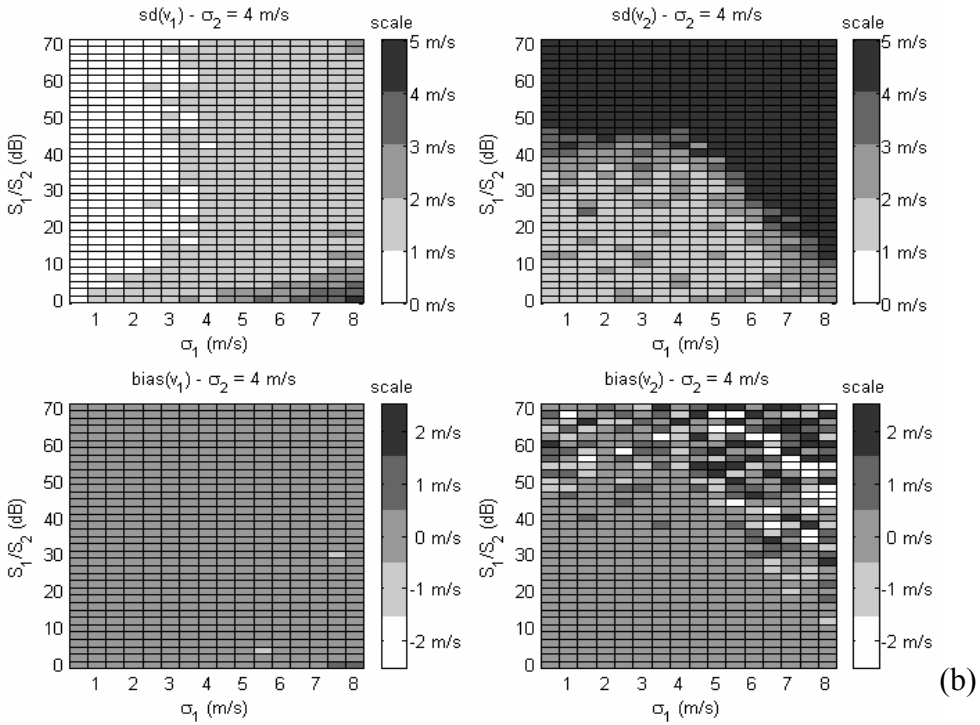


Fig. 2.2.6. Standard error and bias of 1<sup>st</sup>-trip and 2<sup>nd</sup>-trip velocity estimates ( $v_1$  and  $v_2$ ) for the SZ-2 algorithm using (a) the Von Hann window and (b) the Blackman window. In both cases the spectrum width of the 2<sup>nd</sup> trip signal is fixed at 4 m s<sup>-1</sup>.

**b) Noise estimation**

As mentioned before, GMAP can estimate the noise power from the data or, as an alternative, the measured noise level (i.e., through the automatic calibration procedures in the WSR-88D) can be an input to the algorithm. In their report, Ice et al. (2004) recommend the latter to improve the performance of GMAP with fewer samples (e.g., only 17 samples are available for GMAP in the first scan of VCP 11). In the context of phase coded signals the same conclusion is obtained but for different reasons. Because out-of-trip signals look like white noise, GMAP noise estimation algorithm fails in the presence of overlaid echoes. That is, GMAP overestimates the noise power by an amount approximately equal to the sum of overlaid powers (see Fig. 2.2.7). An overestimated noise level produces a filter notch width that is narrower than needed; therefore, impairing the ability of GMAP to effectively remove ground clutter from the signal spectrum.

A simulation was designed to validate this assessment. Simulated time series data consist of weather signals in the 1<sup>st</sup> and 2<sup>nd</sup> trip and ground clutter in the 1<sup>st</sup> trip (in all the cases considered the SNR is very large). Simulated signal powers are such that the power ratio  $S_1/S_2$  is varied from 0 to 70 dB and, in consecutive experiments, the clutter-to-1<sup>st</sup>-trip-signal-ratio  $C/S_1$  is a parameter which increases from -30 to 50 dB in steps of 10 dB. Velocities are random within the Nyquist interval. The spectrum width of the 1<sup>st</sup>-trip signal ( $\sigma_1$ ) varies from 0.5 to 8 m s<sup>-1</sup>; the 2<sup>nd</sup>-trip signal spectrum width ( $\sigma_2$ ) is fixed at 4 m s<sup>-1</sup>. Time series consist of 64 samples windowed with the Blackman window and processed via a simple version of the SZ-2 algorithm with GMAP included. Estimates of 2<sup>nd</sup>-trip velocities are recorded for 100 realizations of each set of parameters. Fig. 2.2.8 shows the statistics of 2<sup>nd</sup> trip velocity ( $v_2$ ) for  $C/S_1 = 30$  dB (the results generalize for all CSR). Two cases are considered (a) GMAP estimates the noise from the data

and (b) the noise is provided to GMAP. Estimates obtained using GMAP with noise estimation exhibit larger errors compared to those obtained when the noise power is provided to GMAP. This is because GMAP overestimates the noise power, which in turn results in a narrower filter notch width and ineffective ground clutter suppression. The presence of a stronger ground clutter residue impairs the recovery of the weak-trip signal, hence the increase in standard errors.

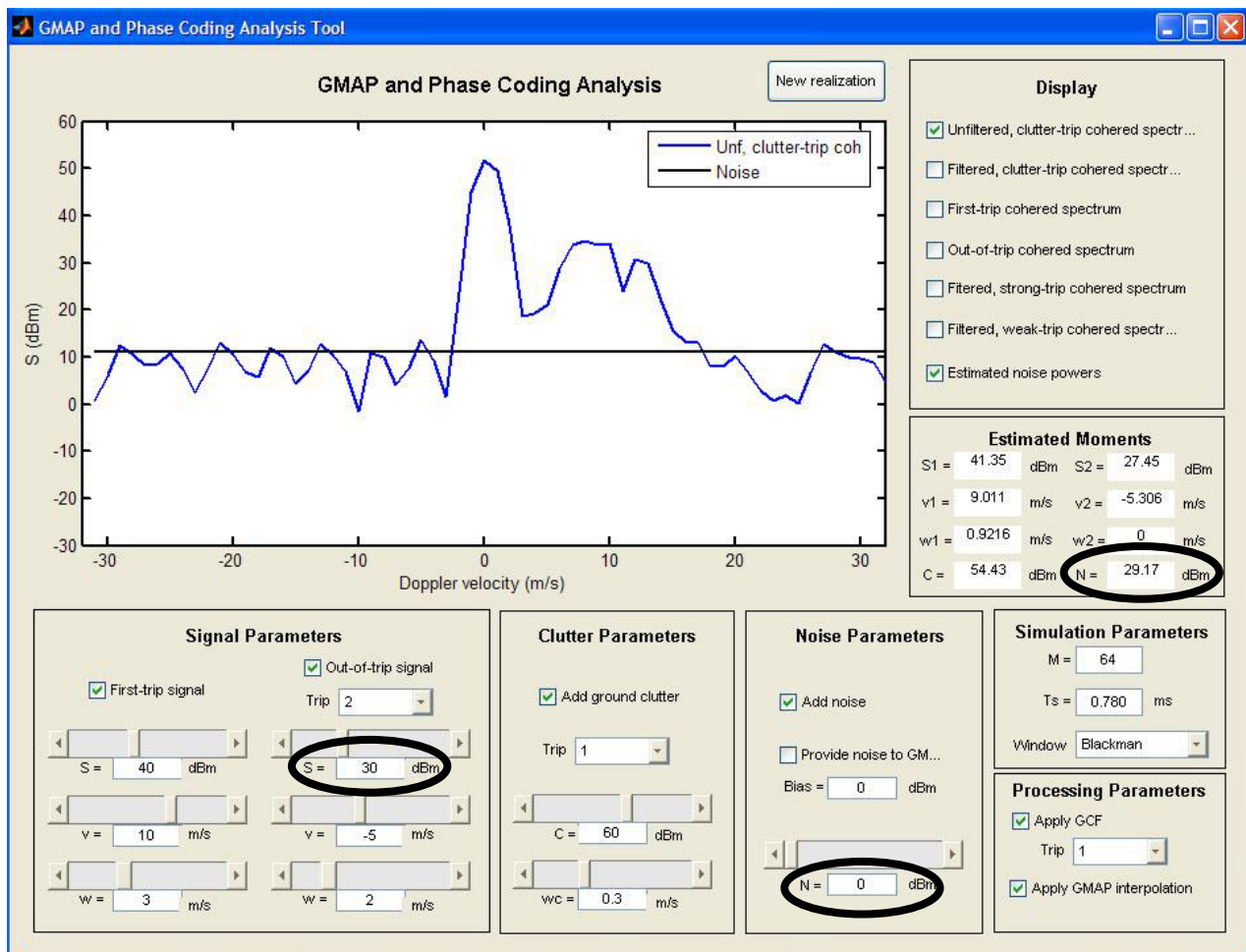


Fig. 2.2.7. An example of GMAP noise estimation algorithm in the context of phase coded signals. Although the simulated noise power is 0 dBm, GMAP overestimates the noise level as 29.17 dBm, which is approximately the power of the overlaid (out-of-trip) signal (30 dBm).

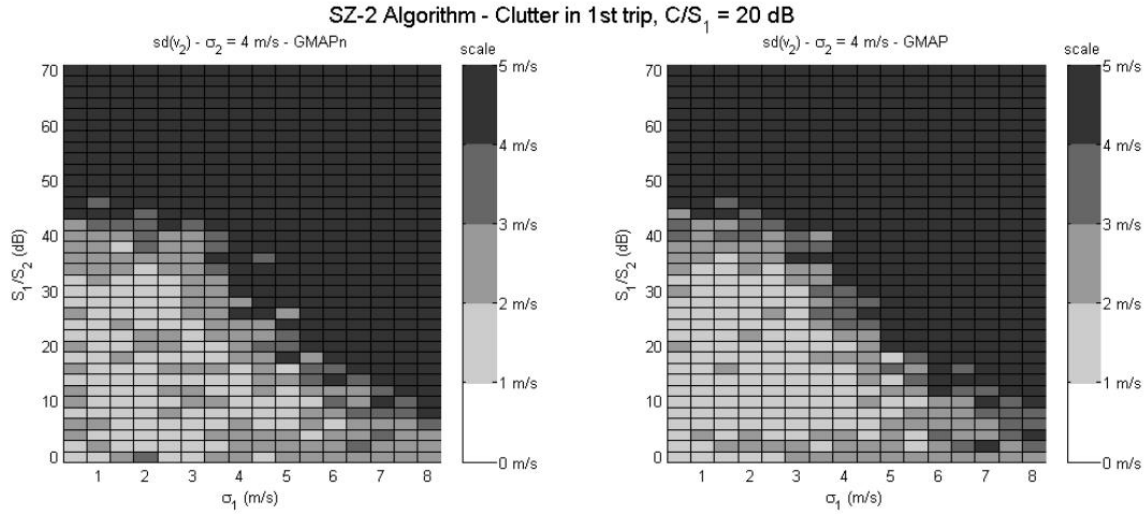


Fig. 2.2.8. Standard error of 2<sup>nd</sup>-trip velocity estimates for the SZ-2 algorithm with GMAP. (left) GMAP with noise estimation and (right) noise is provided to GMAP.

**c) Spectral reconstruction**

One of the most attractive features of GMAP is its ability to reconstruct the signal spectrum after the ground clutter is filtered. Under normal circumstances, this technique minimizes the estimation bias that is typically encountered with any time-domain ground clutter filter, especially for signals whose velocity is near zero. However, GMAP's interpolation scheme assumes that a coherent (Gaussian) weather signal is present after clutter filtering; this is not necessarily true for phase coded signals with overlaid echoes. To study this issue, we consider two cases for the location of ground clutter: (a) ground clutter is in the trip of the strong signal and (b) ground clutter is in the trip of the weak signal. These cases are conceptually depicted in Fig. 2.2.9.

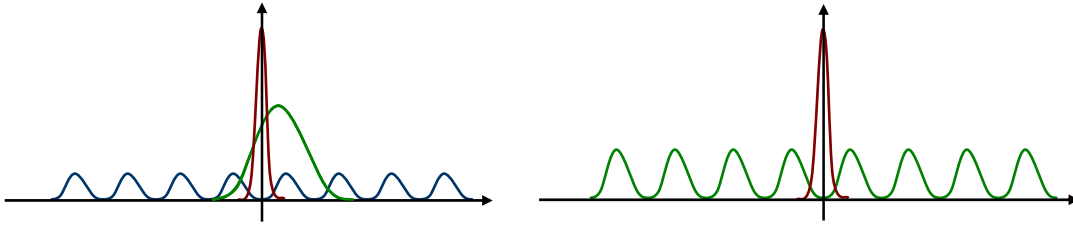


Fig. 2.2.9. Conceptual depiction of ground clutter in the same trip as the strong signal (left) and in the same trip as the weak signal (right).

Simulations were developed to assess GMAP's spectral reconstruction for these two cases. For the first case, simulated time series data consist of weather signals in the 1<sup>st</sup> and 2<sup>nd</sup> trips, and ground clutter in the 1<sup>st</sup> trip (in all the cases considered the SNR is very large). Simulated signal powers are such that the power ratio  $S_1/S_2$  varies from 0 to 70 dB and, in consecutive experiments, the clutter-to-1<sup>st</sup>-trip-signal-ratio  $C/S_1$  increases in steps of 10 dB. Velocities are random within the Nyquist interval. The spectrum width of the 1<sup>st</sup>-trip signal ( $\sigma_1$ ) varies from 0.5 to 8 m s<sup>-1</sup>; the 2<sup>nd</sup>-trip signal spectrum width ( $\sigma_2$ ) is fixed at 4 m s<sup>-1</sup>. Time series consist of 64 samples windowed with the Blackman window and processed via a simple version of the SZ-2 algorithm with GMAP. Estimates of 1<sup>st</sup>-trip velocities are recorded for 100 realizations of each set of parameters. Fig. 2.2.10 shows the statistics of 1<sup>st</sup> trip velocity ( $v_1$ ) for  $C/S_1 = 30$  dB (the results generalize for all CSR). Two cases are considered (a) GMAP with spectral interpolation and (b) GMAP without spectral interpolation (i.e., filtering consists of a simple notch filter). For larger values of the  $S_1/S_2$  ratio (weak overlay), estimates obtained with GMAP's spectral interpolation exhibit lower errors compared to those obtained if a simple notch is applied. This is because the conditions assumed for the spectral interpolation algorithm are more closely approximated for large  $S_1/S_2$  ratios. On the other hand, for small values of the  $S_1/S_2$  ratio (strong overlay) the interpolation fails, and estimates obtained with GMAP working as a simple notch filter are better.

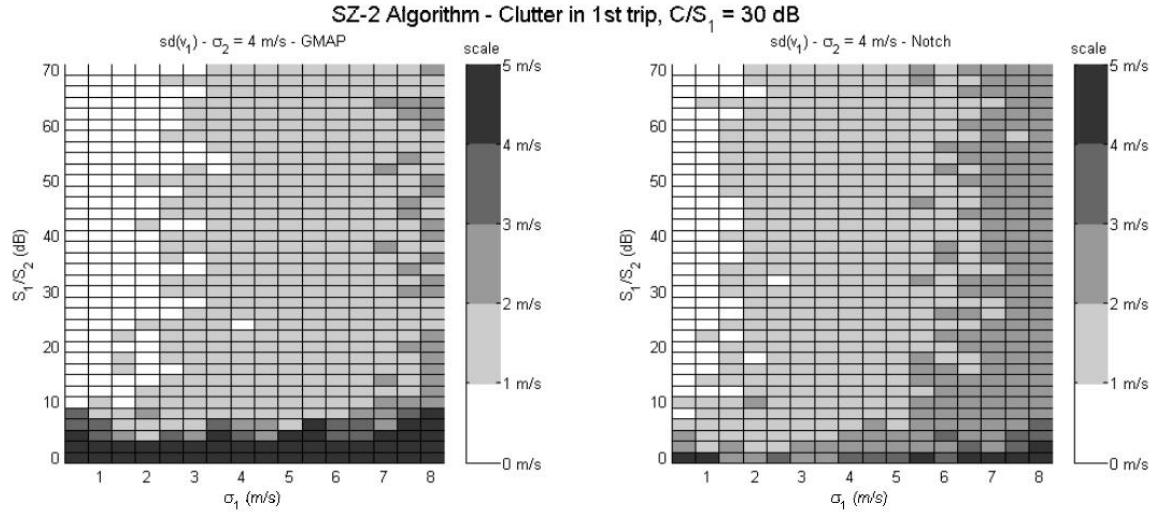


Fig. 2.2.10. Standard error of 1<sup>st</sup>-trip velocity estimates for the SZ-2 algorithm with GMAP when ground clutter is in the same trip as the strong signal. The left and right panels show the results for GMAP with spectral interpolation and GMAP without spectral interpolation (simple notch filter), respectively.

For the second case, simulated time series data consist of weather signals in the 1<sup>st</sup> and 2<sup>nd</sup> trips and ground clutter in the 2<sup>nd</sup> trip (in all the cases considered the SNR is very large). Simulated signal powers are such that the power ratio  $S_1/S_2$  varies from 0 to 70 dB and, in consecutive experiments, the clutter-to-1<sup>st</sup>-trip-signal-ratio  $C/S_1$  is stepped in 10 dB increments from -30 to 50 dB. Velocities are random within the Nyquist interval. The spectrum width of the 1<sup>st</sup>-trip signal ( $\sigma_1$ ) varies from 0.5 to 8 m s<sup>-1</sup>; the 2<sup>nd</sup>-trip signal spectrum width ( $\sigma_2$ ) is fixed at 4 m s<sup>-1</sup>. Time series consist of 64 samples windowed with the Blackman window and processed via a simple version of the SZ-2 algorithm with GMAP. Estimates of 1<sup>st</sup>-trip velocities are recorded for 100 realizations of each set of parameters. Fig. 2.2.11 shows the statistics of 1<sup>st</sup> trip velocity ( $v_1$ ) for  $C/S_1 = 30$  dB (the results generalize for all CSR). Again, two cases are considered (a) GMAP with spectral interpolation and (b) GMAP without spectral interpolation (i.e., filtering consists of a simple notch filter). Estimates obtained with GMAP's spectral interpolation exhibit larger

errors compared to those obtained if a simple notch is applied. It is evident in this case that the conditions assumed for the spectral interpolation algorithm are never satisfied.

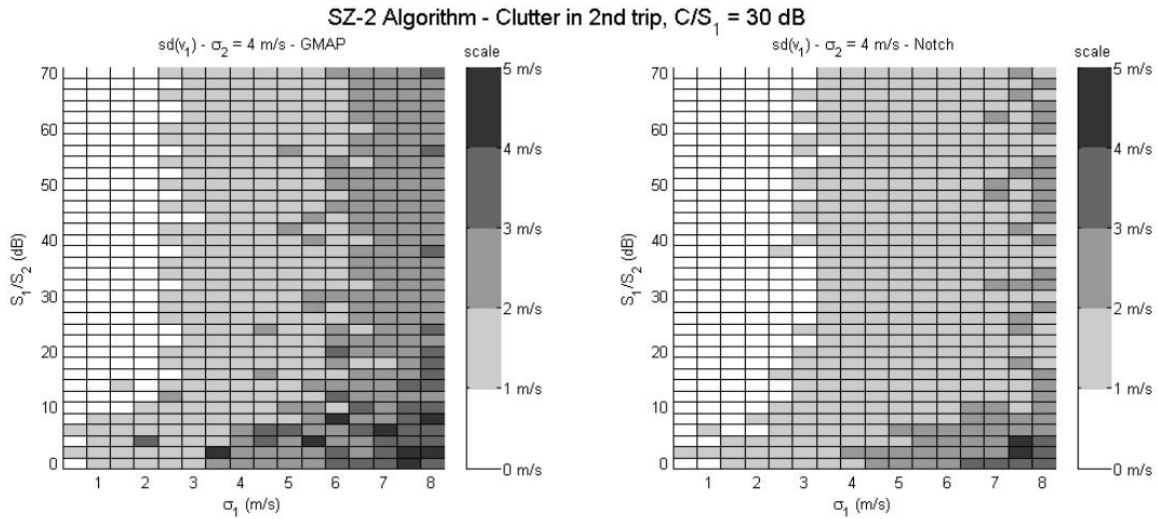


Fig. 2.2.11. Standard error of 1<sup>st</sup>-trip velocity estimates for the SZ-2 algorithm with GMAP when ground clutter is in the same trip as the weak signal. The left and right panels show the results for GMAP with spectral interpolation and GMAP without spectral interpolation (simple notch filter), respectively.

Summarizing, GMAP's spectral reconstruction algorithm assumes that a coherent signal spectrum remains after filtering. However, this condition is not always met if phase coded signals are overlaid. In such cases, a simple notch filter works better as demonstrated by the previous analyses.

**d) Filtered time series**

As described before, GMAP operates on frequency-domain spectral components and returns the filtered signal power spectrum. However, decoding (recohering) of phase coded signals must occur in the time domain. It is impossible to reconstruct the time series data merely from the power spectrum (i.e., the magnitude squared of the time-series Fourier transform) as all the phase

information is lost. The phase of the filtered signal spectrum is the same as the one of the original (unfiltered) signal spectrum except on those spectral components in which GMAP replaced the original spectrum with a reconstructed spectrum (or simply zeros in the case of a notch filter). Thus, in addition to having to save the original phase spectrum, we are faced with the question of how to determine which components were modified by GMAP and what to do with the phases of these spectral components. The first question could be easily handled by modifying GMAP so that it returns the number of spectral components in the “gap”. A simulation was designed to answer the second question, that is, which phases to use for the spectral components in the gap. Simulated time series data consist of a weather signal in the 2<sup>nd</sup> trip and ground clutter in the 1<sup>st</sup> trip (in all the cases considered the SNR is very large). Simulated powers are such that the power ratio  $C/S_1$  varies from 0 to 70 dB. Velocities are random within the Nyquist interval. The spectrum width of the signal varies from 0.5 to 8 m s<sup>-1</sup>. Time series consist of 64 samples windowed with the Blackman window and processed via a simple version of the SZ-2 algorithm with GMAP. Estimates of 2<sup>nd</sup>-trip velocities are recorded for 100 realizations of each set of parameters. Fig. 2.2.12 shows the statistics of 2<sup>nd</sup> trip velocity ( $v_2$ ). Three cases are considered: (a) reconstruction with original phases, (b) reconstruction with random phases, and (c) reconstruction with zero phases. Although the performance of these three approaches is almost equivalent, reconstruction with zero phases works the best for CSR less than about 35 dB. For larger CSR, the three approaches behave similarly, with a slight advantage to the approach that reconstructs the phase spectrum with random phases.

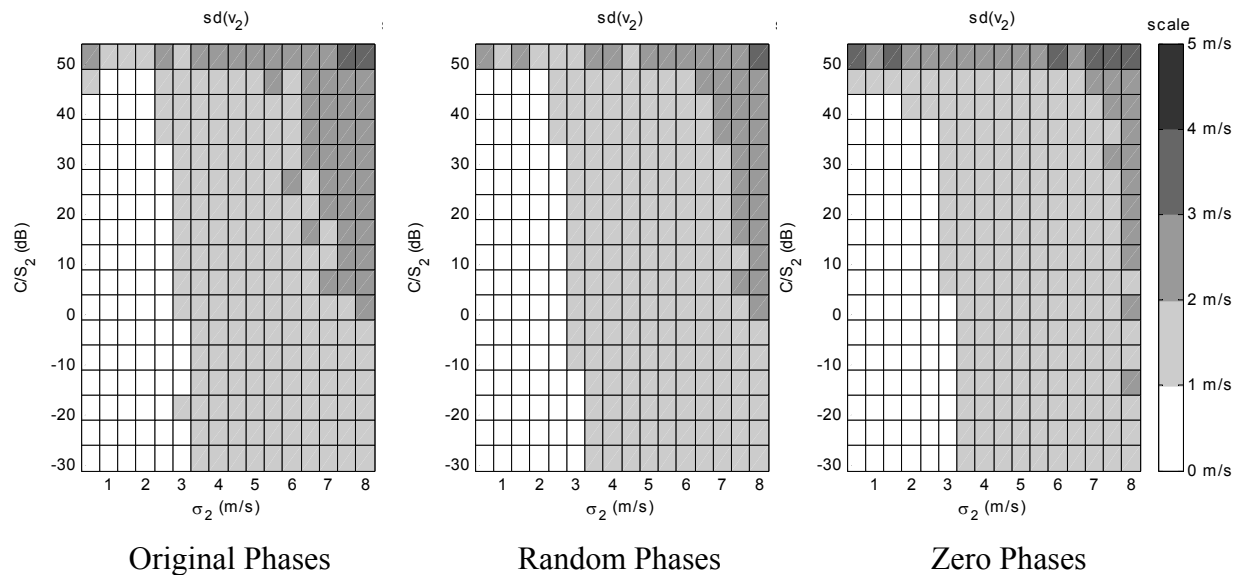


Fig. 2.2.12. Standard error of 2<sup>nd</sup>-trip velocity estimates for the SZ-2 algorithm with GMAP. The left, medium, and right panels show the results for a filtered phase spectrum reconstruction using original, random, and zero phases, respectively.

#### 2.3.4. Summary of recommendations

- Processing with the Blackman window is necessary to achieve the required clutter suppression by GMAP. However, this is done at the expense of loss of estimate accuracy. A hybrid approach in which the window is switched between Von Hann and Blackman depending on whether clutter is present or not should be investigated.
- Because out-of-trip echoes appear as white noise, the receiver noise power should be provided to GMAP instead of using GMAP's noise estimation algorithm. Because GMAP's performance depends on having an accurate estimate of the noise level, a reliable way to obtain this power (analogous to the current automatic calibration procedures) should be available in the operational system.

- Although GMAP's spectral reconstruction capabilities are a definite advantage with respect to standard time-domain filters, the reconstruction algorithm assumes that the remaining signal after clutter filtering is coherent. This assumption approximately holds if the clutter signal is in the same trip as the strong weather signal. However, if the clutter signal is not in the same trip as the strong weather signal, the interpolation fails and a simple notch filter is preferred.
- The original (unfiltered) phase spectrum must be saved in order to recover the filtered time series data after filtering with GMAP. In addition, GMAP must be modified to return the number of spectral coefficients identified as clutter. Finally, the filtered phase spectrum can be derived from the original one by zeroing out the phases of those spectral components modified by GMAP.

### 2.3.5. *Performance comparison*

The performance of GMAP is illustrated by comparing it with the 5<sup>th</sup>-order elliptic filter implemented in the legacy RDA. The first case (Fig. 2.2.13.a) corresponds to data collected with the KOUN radar on October 8, 2002 when a large region of stratiform precipitation slowly moved across Oklahoma. The second case (Fig. 2.2.13.b) corresponds to data collected on June 4, 2003 when a Mesoscale Convective System (MCS) developed early in the morning in North Texas and Southwestern Oklahoma, it propagated to the NE, and was over the KOUN radar in mid morning. By that time, the system developed a mesoscale convective vortex in its NW part which caused formation of three intense cells. Fig. 2.2.13 shows the results of processing these time series data with both ground clutter filters. Filtering is applied in the locations dictated by the bypass map for KOUN. Although performance of the two filters is similar, GMAP attains

slightly larger suppression; evidenced by the displayed lower reflectivity values. This is also confirmed by the Doppler velocity fields, where the elliptic filter shows a more prominent bias toward zero, which is usually indicative of stronger clutter residue.

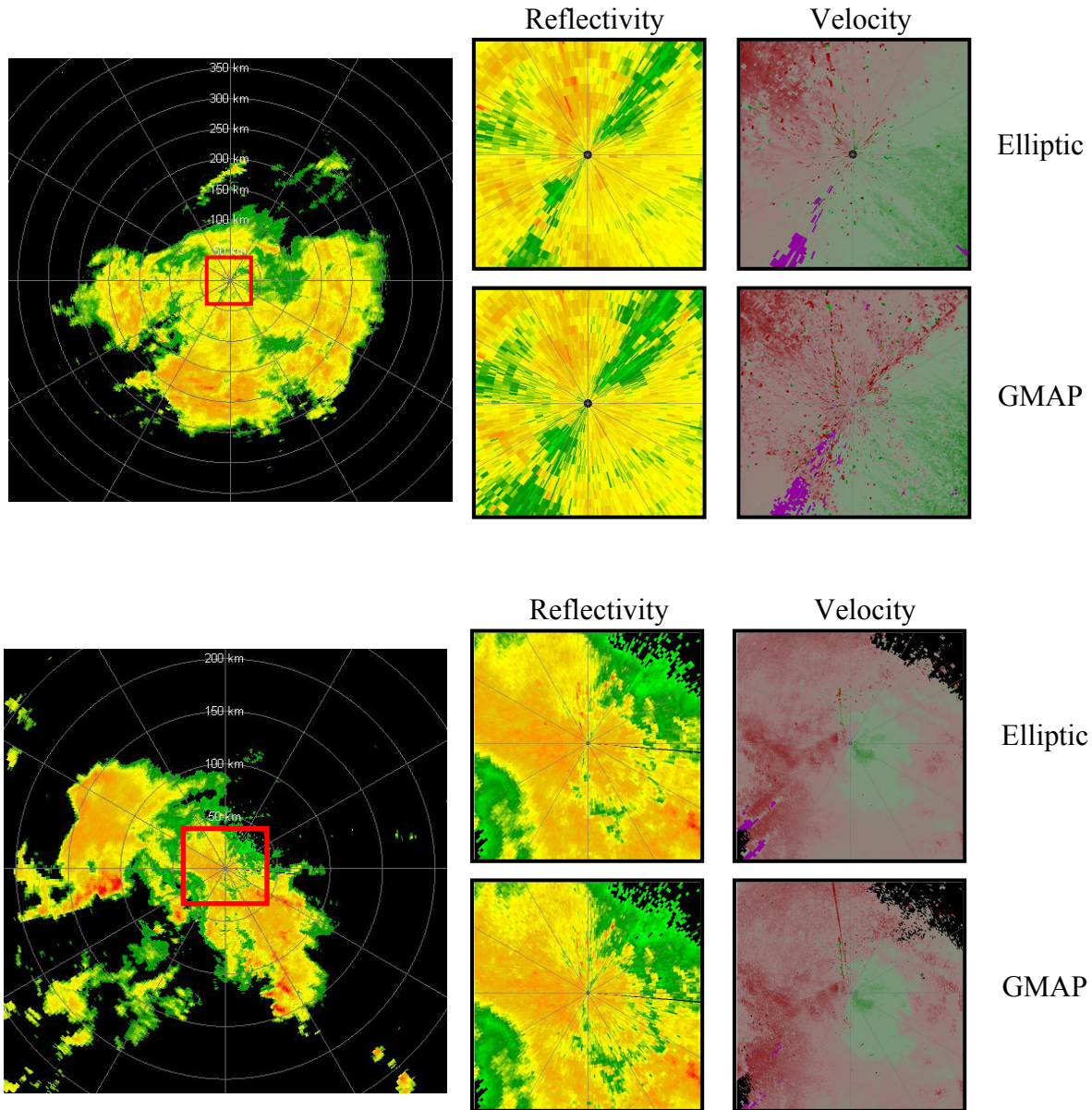


Fig. 2.2.13. Performance comparison between GMAP and the legacy 5-pole elliptic filter. Zoomed in plots on the right correspond to the red box on the left. (a) Data was collected on October 8, 2002 at approximately 15:11 GMT, (b) data was collected on June 4, 2003 at approximately 15:07 GMT. Range circles are spaced 50 km apart.

### **3. The SZ-2 Algorithm**

#### **3.1. Introduction**

The SZ-2 algorithm was first introduced by Sachidananda et al. (1998) in a study of range-velocity ambiguity mitigation using phase coding. Unlike the stand-alone SZ-1 algorithm, SZ-2 relies on power and spectrum width estimates obtained from a long pulse repetition time (PRT). The SZ-2 algorithm is computationally simpler than its stand-alone counterpart as it only tries to recover Doppler velocities associated with the strong and the weak trip signals and spectrum widths associated with the strong trip signal. Analogous to the legacy split cut, the volume coverage pattern (VCP) is designed such that a scan having non-phase-coded pulses at a long PRT is immediately followed by a scan with phase-coded signals using a short PRT at the same elevation angle. Hence, determination of the number and location of overlaid trips can be done by examining the overlay-free long-PRT powers.

The basic SZ-2 algorithm was documented in a joint report by NCAR and NSSL dated Aug 15, 2003. However, that algorithm did not consider the GMAP clutter filter, and only handled ground clutter within the 1<sup>st</sup> trip (i.e., within ~115 km of the radar site). Although most of the time ground clutter is in the 1<sup>st</sup> trip, there are radar sites where mountainous terrain, and therefore ground clutter, is beyond the 1<sup>st</sup> trip (i.e., more than 115 km away from the radar). Still, even for the sites that are not near mountains, the presence of anomalous propagation (AP) clutter in trips other than the 1<sup>st</sup> is definitely possible. It is evident that algorithms running in the ORDA should be able to handle any type of clutter in any of the possible trips. Addressing these issues in the

SZ-2 algorithm was a priority for this fiscal year, and the results of these efforts are described next.

### **3.2. Clutter Filtering in the SZ-2 Algorithm**

Clutter filtering in the RDA is controlled by two maps: the bypass map which is automatically generated, and the clutter censor zones which are defined in real time by the radar operator. Filtering occurs only at those range locations where either (or both) maps indicate the presence of clutter (in general, clutter can be ground clutter or anomalous propagation clutter). Because clutter filtering should occur before the moments are estimated, under typical conditions, the sequence of operations and conditions for clutter filtering are straightforward. However, this not so evident if dealing with overlaid echoes and phase coded signals.

Five issues were identified that required further investigation. These are: (1) sequence of operations, (2) conditions for filtering, (3) recovery of weak-trip signals in the presence of clutter, (4) handling ground clutter in any of the possible trips (including the possibility of overlaid clutter), and (5) handling AP clutter in any of the possible trips (also including the possibility of overlaid clutter).

After comparisons of estimates using numerous simulations it became possible to define the basic sequence of operations in the SZ-2 algorithm with clutter filtering. It is:

- 1) Cohere for trip with clutter
- 2) Apply clutter filter
- 3) Cohere for trip with strong signal
- 4) Recover strong-trip velocity

- 5) Apply processing notch filter (PNF)
- 6) Cohere for trip with weak signal
- 7) Recover weak-trip velocity

Conditions for filtering are established by the clutter maps: the bypass map determines the presence of ground clutter, and the clutter censor zones determine the presence of AP clutter. Nonetheless, even if the maps indicate the presence of clutter, clutter filters could be bypassed for very low clutter-to-signal ratios (CSR). That is, the strength of the clutter signal could be a useful additional factor in determining whether to filter or not. Unfortunately, the clutter maps solely indicate the presence of clutter, not its strength with respect to the weather signals<sup>1</sup>. Moreover, exploiting GMAP to estimate the clutter power during the long-PRT scan is not feasible since the removed power by GMAP ( $P_{REM}$ ) is a reliable estimator of clutter power only if this power is larger than the weather signal power. Additional conditions for filtering could involve the location of clutter returns with respect to overlaid weather returns. All these issues are evaluated next.

Simulations were designed to establish the performance of the SZ-2 algorithm in the presence of clutter. The results support our recommendations for the first release of the ORDA SZ-2 algorithm.

---

<sup>1</sup> This is true in the legacy RDA. Including the clutter strength in the maps was proposed as an enhancement for the ORDA; however, it is unclear at this time if the ORDA will have this feature.

### 3.2.1. *Simulation description:*

Time series data were simulated using standard algorithms (Zrnic 1975). The composite weather echo consists of 1<sup>st</sup> trip signal, 2<sup>nd</sup> trip signal, clutter, and white noise. Signal and clutter are characterized by power ( $S$ ), mean Doppler velocity ( $v$ ), and spectrum width ( $\sigma$ ).  $S_1$ ,  $v_1$ ,  $\sigma_1$ ,  $S_2$ ,  $v_2$ ,  $\sigma_2$ , and  $C$  are variable parameters. For clutter  $v_c = 0$  and  $\sigma_c = 0.3 \text{ m s}^{-1}$ . The effects of white noise are minimized by simulating a SNR larger than 30 dB for all cases.

Clutter filtering is accomplished via the GMAP filter, which was ported from the source code provided by Sigmet (Release 8.04.3, December 2003). The code was modified to output the number of coefficients notched by GMAP and to allow enabling and disabling the spectral reconstruction across the filter notch. Disabling the spectral reconstruction results in an ideal notch filter with an adaptive width (the width of the notch is still determined by GMAP).

Processing involves the following steps:

- 1) Cohere to the trip where clutter is present
- 2) Compute power spectrum and save phase information
- 3) Apply GMAP (filter can be bypassed)
- 4) Reconstruct phase spectrum
- 5) Go back to the time domain
- 6) Cohere to 1<sup>st</sup> trip
- 7) Compute lag-one autocorrelation
- 8) Cohere to 2<sup>nd</sup> trip
- 9) Compute lag-one autocorrelation
- 10) Determine strong and weak trips

- 11) Compute strong-trip velocity
- 12) Apply PNF
- 13) Cohere to weak trip
- 14) Compute weak-trip velocity
- 15) Return estimates of  $v_1$  and  $v_2$

Throughout these simulation we assumed  $\sigma_2 = 1, 2, 4, \text{ or } 8 \text{ m s}^{-1}$ ,  $M = 64$ , exact SZ(8/64) switching code, and used the Blackman window.

Biases and standard deviations were obtained for both  $v_1$  and  $v_2$  as a function of  $\sigma_1$  and  $S_1/S_2$  with  $\sigma_2$  as a parameter.  $\sigma_1$  spans the range  $[0.5, 8] \text{ m s}^{-1}$  in steps of  $0.5 \text{ m s}^{-1}$ . The strong-to-weak-trip power ratio spans the range  $[0, 70] \text{ dB}$  in steps of  $2 \text{ dB}$ . Each set of statistics is computed from 100 realizations. Simulated  $v_1$  and  $v_2$  velocities are independently and randomly chosen within the Nyquist interval.

### 3.2.2. *Analyzed cases*

Different situations were considered for the clutter location and strength. For each case, the clutter filtering function was (a) disabled, (b) standard GMAP, (c) GMAP without noise estimation (noise is provided to it), or (d) GMAP without spectral reconstruction. For brevity sake we summarize representative cases in the following table although a much more comprehensive set was analyzed (i.e., wider and finer range of parameters):

	<b>Clutter location</b>	$C/S_1$	<b>GCF</b>
<b>1</b>	No clutter	-	No GCF
<b>2</b>	1 <sup>st</sup> trip	30 dB	No GCF
<b>3</b>	1 <sup>st</sup> trip	30 dB	GMAP
<b>4</b>	1 <sup>st</sup> trip	30 dB	GMAP without noise estimation
<b>5</b>	1 <sup>st</sup> trip	30 dB	GMAP without spectral reconstruction
<b>6</b>	1 <sup>st</sup> trip	-20 dB	No GCF
<b>7</b>	1 <sup>st</sup> trip	-20 dB	GMAP
<b>8</b>	1 <sup>st</sup> trip	-20 dB	GMAP without noise estimation
<b>9</b>	1 <sup>st</sup> trip	-20 dB	GMAP without spectral reconstruction
<b>10</b>	2 <sup>nd</sup> trip	30 dB	No GCF
<b>11</b>	2 <sup>nd</sup> trip	30 dB	GMAP
<b>12</b>	2 <sup>nd</sup> trip	30 dB	GMAP without noise estimation
<b>13</b>	2 <sup>nd</sup> trip	30 dB	GMAP without spectral reconstruction
<b>14</b>	2 <sup>nd</sup> trip	-20 dB	No GCF
<b>15</b>	2 <sup>nd</sup> trip	-20 dB	GMAP
<b>16</b>	2 <sup>nd</sup> trip	-20 dB	GMAP without noise estimation
<b>17</b>	2 <sup>nd</sup> trip	-20 dB	GMAP without spectral reconstruction

### 3.2.3. Results

From case 1, plots agree with simulations in report 2 (Sachidananda et al. 1998). These results are the ones in Fig. 2.2.6, which is repeated here for convenience as Fig. 3.2.1. Comparison of cases 2, 3, 4, and 5 (Fig. 3.2.2) with case 1 reveals that the weak-trip velocity ( $v_2$ ) recovery region is significantly reduced by the presence of clutter in the trip of the strong signal. In addition, larger errors of  $v_1$  are observed for low values of  $S_1/S_2$ . This occurs because for some cases, step 10 of the algorithm regards the 2<sup>nd</sup> trip signal as the strong signal and the clutter is in the 1<sup>st</sup> trip (with the “weak” signal).

From cases 2 through 5 (Fig. 3.2.2) and 6 through 9 (Fig. 3.2.3), it is evident that the only case for which a clutter filter could be bypassed is for the estimation of  $v_1$  at very low CSR; otherwise, a clutter filter is necessary to obtain meaningful estimates of  $v_1$  and  $v_2$ . In general, GMAP without noise estimation seems to provide the best compromise in terms of recovery region;

GMAP without interpolation is superior only for the estimation of  $v_1$  at large CSR and low signal power ratios  $S_1/S_2$ .

If clutter is in the same trip as the weak weather signal (cases 10 through 17 in Figs. 3.2.4 and 3.2.5) it is true that clutter filtering is necessary even if the CSR is very low. Also, it is impossible to recover the velocity of the weak weather signal. This is because between the clutter filtering, recohering, the PNF, and recohering again, the weak signal spectrum is hopelessly distorted. In this case, weak trip velocity estimates must be censored. As discussed in section 2.2., the recovery of  $v_1$  is greatly improved when using GMAP without spectral reconstruction (simple notch).

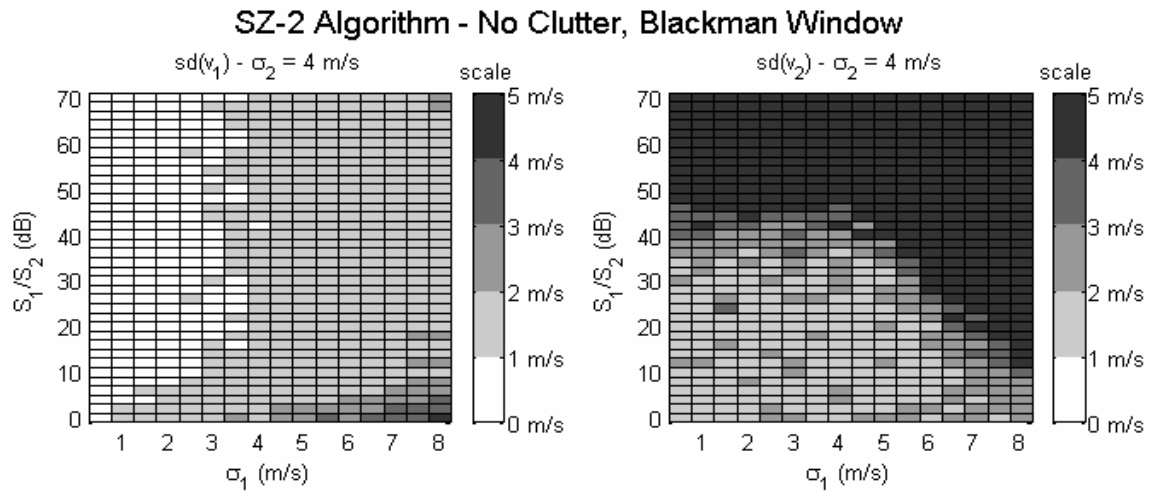


Fig. 3.2.1. Standard error of velocity estimates for the 1<sup>st</sup> trip (left) and 2<sup>nd</sup> trip (right) signals. Clutter is not present and  $\sigma_2 = 4 \text{ m s}^{-1}$ .

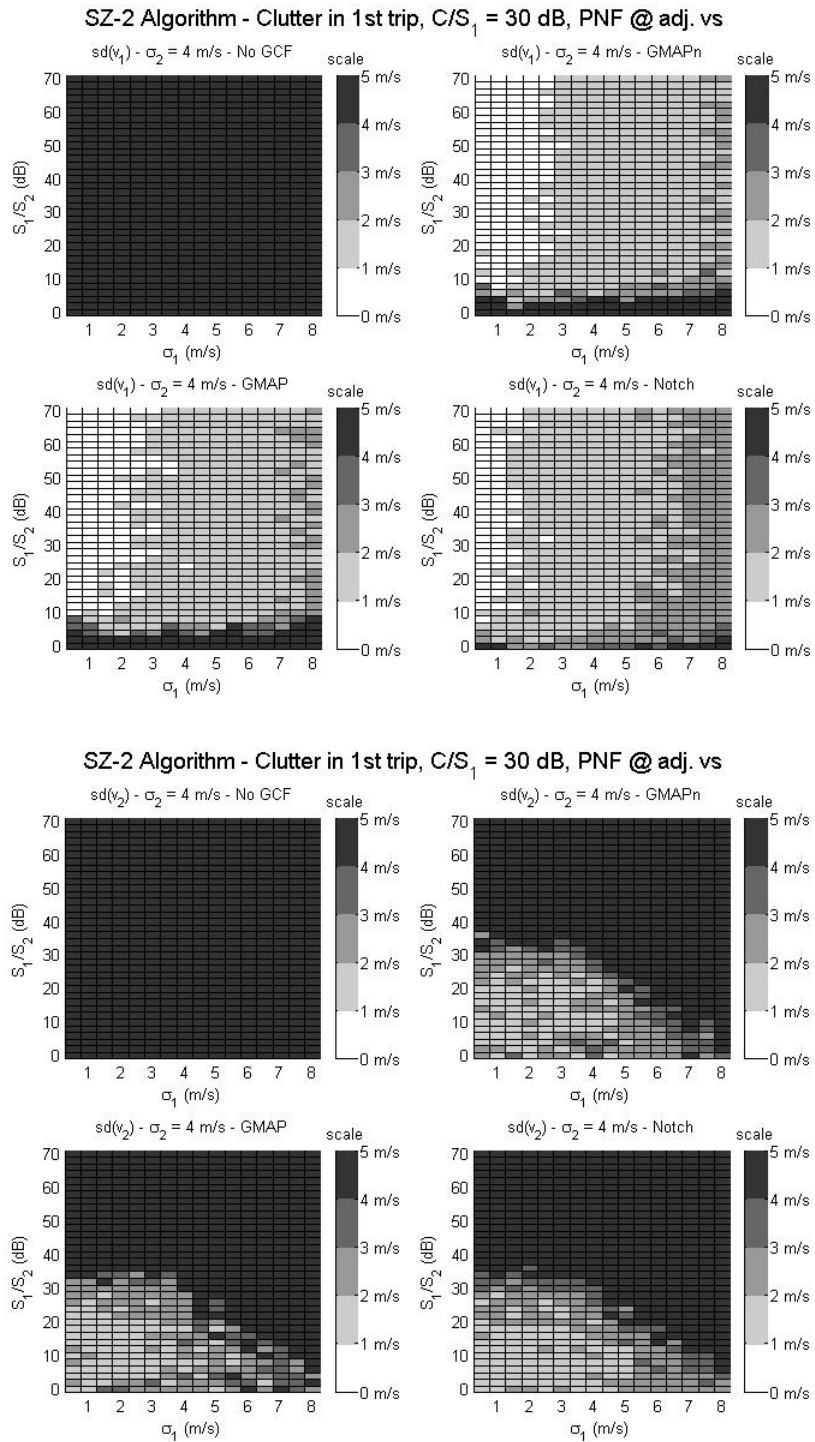


Fig. 3.2.2. Standard error of velocity estimates for the 1<sup>st</sup> trip (top) and 2<sup>nd</sup> trip (bottom) signals. Clutter is in the 1<sup>st</sup> trip. The CSR is 30 dB and  $\sigma_2 = 4$  m s<sup>-1</sup>. The four panels in each figure correspond to (clockwise starting from the top left): (a) clutter filter disabled, (b) standard GMAP with noise estimation, (c) GMAP without noise estimation, and (d) GMAP without spectral interpolation.

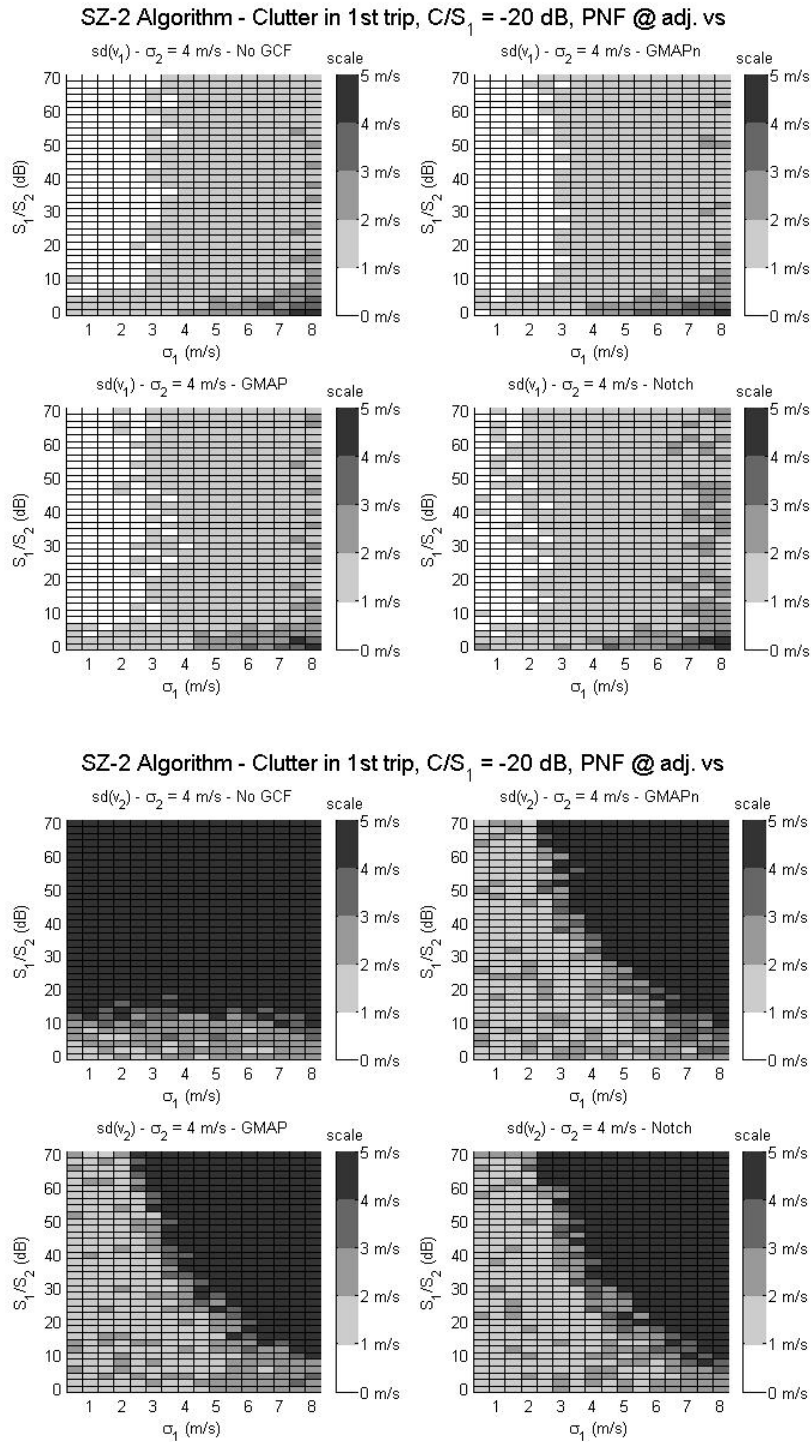


Fig. 3.2.3. Standard error of velocity estimates for the 1<sup>st</sup> trip (top) and 2<sup>nd</sup> trip (bottom) signals. Clutter is in the 1<sup>st</sup> trip. The CSR is  $-20$  dB and  $\sigma_2 = 4$  m s<sup>-1</sup>. The four panels in each figure correspond to (clockwise starting from the top left): (a) clutter filter disabled, (b) GMAP with noise estimation, (c) GMAP with provided noise, and (d) GMAP without spectral interpolation.

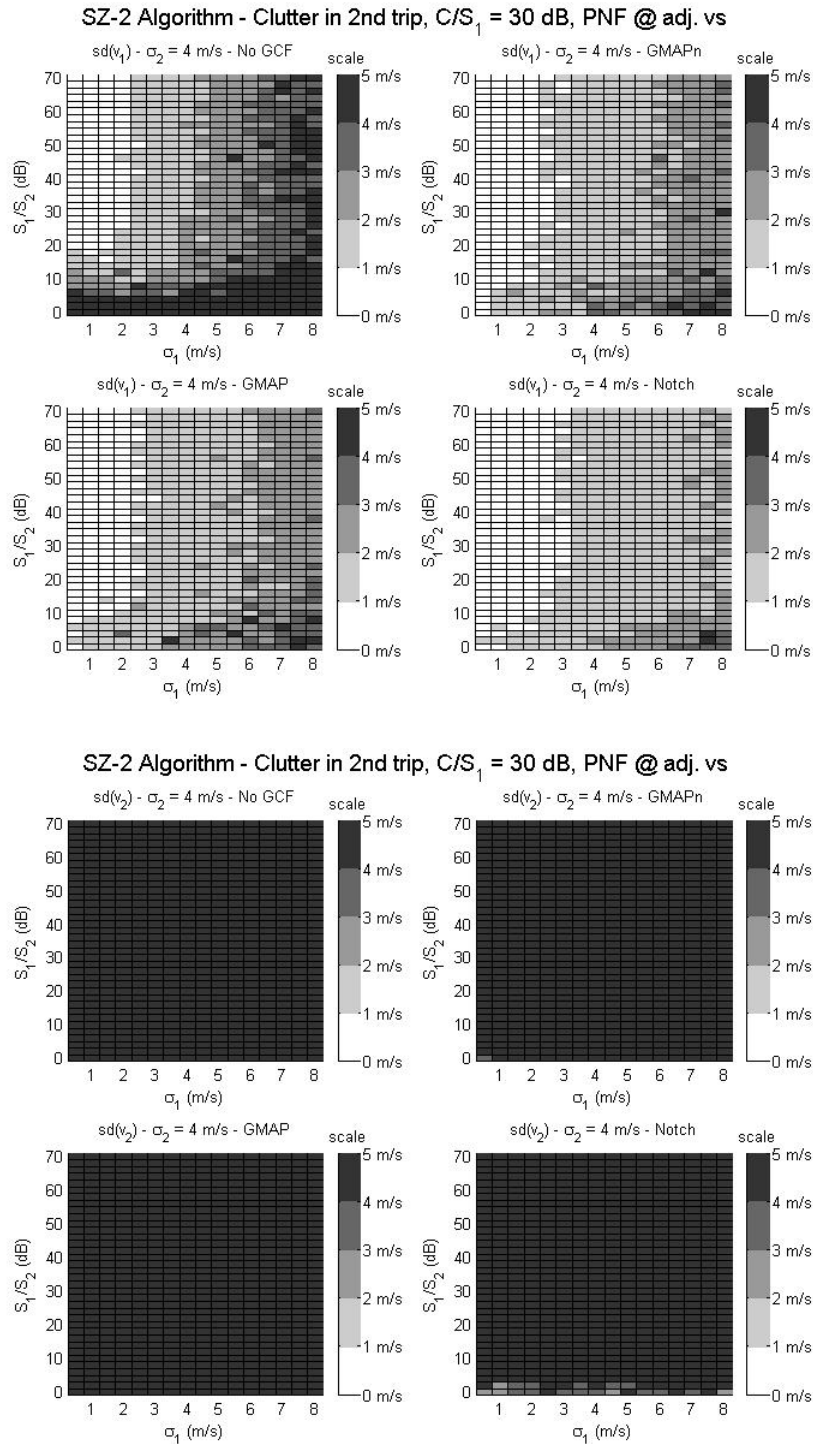


Fig. 3.2.4. Standard error of velocity estimates for the 1<sup>st</sup> trip (top) and 2<sup>nd</sup> trip (bottom) signals.

Clutter is in the 2<sup>nd</sup> trip. The CSR is 30 dB and  $\sigma_2 = 4$  m s<sup>-1</sup>. The four panels in each figure correspond to (clockwise starting from the top left): (a) clutter filter disabled, (b) GMAP with noise estimation, (c) GMAP with provided noise, and (d) GMAP without spectral interpolation.

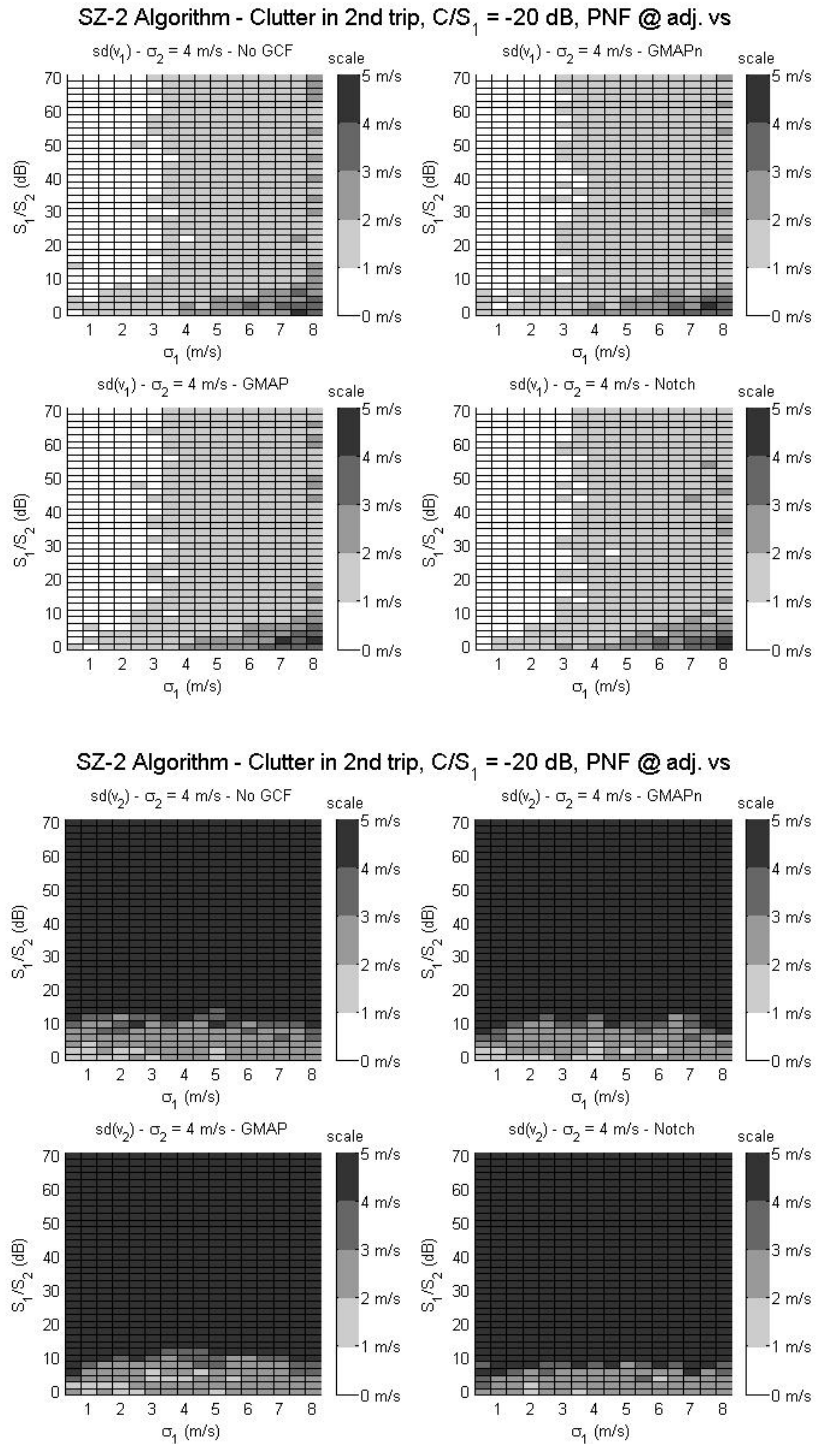


Fig. 3.2.5. Standard error of velocity estimates for the 1<sup>st</sup> trip (top) and 2<sup>nd</sup> trip (bottom) signals. Clutter is in the 2<sup>nd</sup> trip. The CSR is -20 dB and  $\sigma_2 = 4$  m s<sup>-1</sup>. The four panels in each figure correspond to (clockwise starting from the top left): (a) clutter filter disabled, (b) GMAP with noise estimation, (c) GMAP with provided noise, and (d) GMAP without spectral interpolation.

To summarize, from this experiment we derived the following rules:

- Clutter (ground clutter or AP clutter) must be filtered before any moment estimate is attempted. One of the first steps in the SZ-2 algorithm should involve cohering to the trip with clutter and applying the clutter filter.
- If clutter is not with the strong signal, the weak signal cannot be recovered and weak trip velocities must be censored.
- If clutter is not with the strong signal, GMAP without spectral interpolation (simple notch) offers an advantage over the GMAP provided by Sigmet. This requires minor changes to the GMAP algorithm.

### **3.3. Proposed changes to the SZ-2 algorithm**

After extensive investigation, the following changes to the basic algorithm reported by NCAR and NSSL (Aug 15, 2003) are proposed for the first release of the SZ-2 algorithm:

- Incorporation of GMAP for clutter filtering
- Handling of clutter in any of the possible trips
- Optimization of the processing notch filter (PNF)
- Addition of short-PRT spectrum width computation
- Refinement of censoring rules and thresholds

#### *3.3.1. Incorporation of GMAP for clutter filtering*

Two types of clutter filter in the algorithm reported on August 2003 were proposed. One was the legacy 5<sup>th</sup>-order elliptic filter and the other a spectral filter. The 5<sup>th</sup>-order elliptic filter introduces

phase distortions that considerably impair recovery of velocities from overlaid echoes. Although compensating for these distortions is possible, the required additional computations tilted the choice toward the spectral filter. Then, NWS decided that the only clutter filter in the ORDA will be GMAP, which is a sophisticated spectral filter. Changes in the SZ-2 algorithm to incorporate the GMAP have been discussed in section 2 and are summarized below:

- Use the Blackman window instead of the von Hann window to achieve required clutter suppression with GMAP
- The unfiltered power spectrum must be computed (this involves a discrete Fourier transform of the time series data).
- The original phase spectrum must be saved and reconstructed after clutter filtering in order to produce the filtered time series for the re-cohering process.

Because of this last change, GMAP should be modified to return the number of spectral components with clutter (this requires minor functional changes).

### 3.3.2. *Handling of clutter in any of the possible trips*

The August 2003 algorithm considered clutter only in the 1<sup>st</sup> trip. To handle clutter in any of the possible trips, three cases are examined: (1) no clutter in any trips, (2) clutter in one of the trips, and (3) clutter in multiple trips. Obviously, if clutter is not present, clutter filtering is not invoked. If clutter is present in just one trip, the algorithm is modified to cohere to the trip with clutter (not necessarily the 1<sup>st</sup> trip), GMAP is applied followed by the usual processing. Finally, if clutter is present in more than one trip (overlaid clutter), velocity estimates are censored as they are deemed unrecoverable.

### 3.3.3. Optimization of the processing notch filter

The processing notch filter tries to remove most of the strong-trip weather signal while preserving (at least) two “clean” replicas of the out-of-trip (weak) weather signal. The August 2003 algorithm controls the PNF notch width using the difference between the strong and weak signal trips. A trip difference of one corresponds to a notch width of 75% of the spectral components; a trip difference of two to 50% of the spectral components. PNF placement was determined using the CSR as an indicator of the presence of clutter. If clutter is not present, the PNF was centered on the strong-trip Doppler velocity ( $v_s$ ); otherwise, the PNF was centered half-way between clutter and the strong-trip weather spectrum (i.e., at  $v_s/2$  since the velocity of clutter is zero).

A better PNF placement scheme consists on centering the PNF on an “adjusted” velocity (adjusted  $v_s$ ). This adjusted  $v_s$  is the closest velocity to  $v_s$  such that the clutter filter “gap” is within the PNF’s stop band. The computation of the PNF center is then based on  $v_s$ , the PNF’s notch width, and the number of spectral coefficients with clutter  $k_{GMAP}$  (GMAP can be easily modified to return this number).

A simulation was developed to test this technique. Simulated time series data consist of weather signals in the 1<sup>st</sup> and 2<sup>nd</sup> trips with 64 samples; clutter in the 1<sup>st</sup> trip, and the SNR is very large. Simulated signal powers are such that the power ratio  $S_1/S_2$  varies from 0 to 70 dB and velocities are random within the Nyquist interval. The spectrum width of the 1<sup>st</sup>-trip signal ( $\sigma_1$ ) varies from 0.5 to 8 m s<sup>-1</sup>; the 2<sup>nd</sup>-trip signal spectrum width ( $\sigma_2$ ) is fixed in succeeding experiments at 1, 2, 4, and 8 m s<sup>-1</sup>. Estimates of 2<sup>nd</sup>-trip velocities obtained via a simple version of the SZ-2 algorithm are recorded for 100 realizations of each set of parameters. Fig. 3.3.1 shows the

statistics of 2<sup>nd</sup> trip velocities ( $v_2$ ) for  $\sigma_2 = 4 \text{ m s}^{-1}$  using (a) a PNF centered at  $v_s$ , (b) a PNF centered at  $v_s/2$ , and (c) a PNF centered at the “adjusted”  $v_s$ . It is evident from this figure that centering the PNF on the adjusted  $v_s$  yields the best performance (i.e., larger recovery region for  $v_2$ ), except for narrow spectrum widths ( $\sigma_1$ ) and large  $S_1/S_2$  ratios.

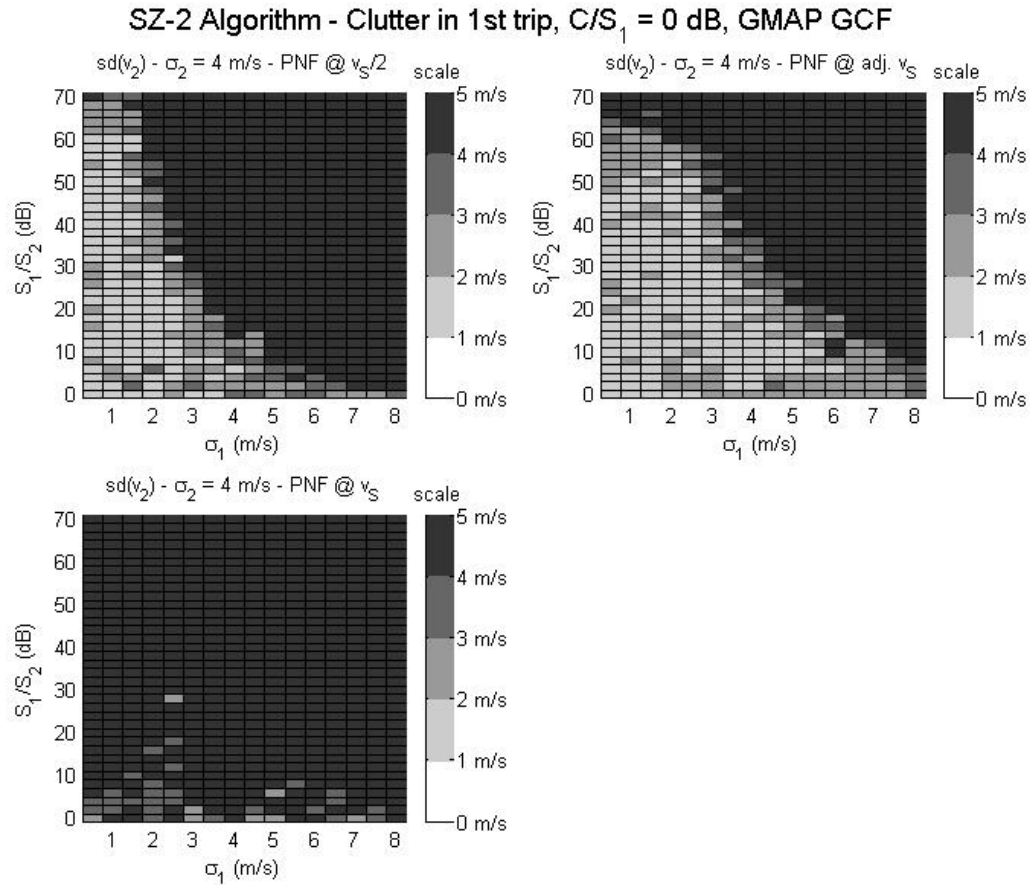


Fig. 3.3.1. Standard error of velocity estimates for the 2<sup>nd</sup> trip signal. Clutter is in the 1<sup>st</sup> trip. The CSR is 0 dB and  $\sigma_2 = 4 \text{ m s}^{-1}$ . The three panels correspond to (clockwise starting from the top left): (a) PNF centered at  $v_s/2$ , (b) PNF centered at the adjusted  $v_s$ , and (c) PNF centered at  $v_s$ .

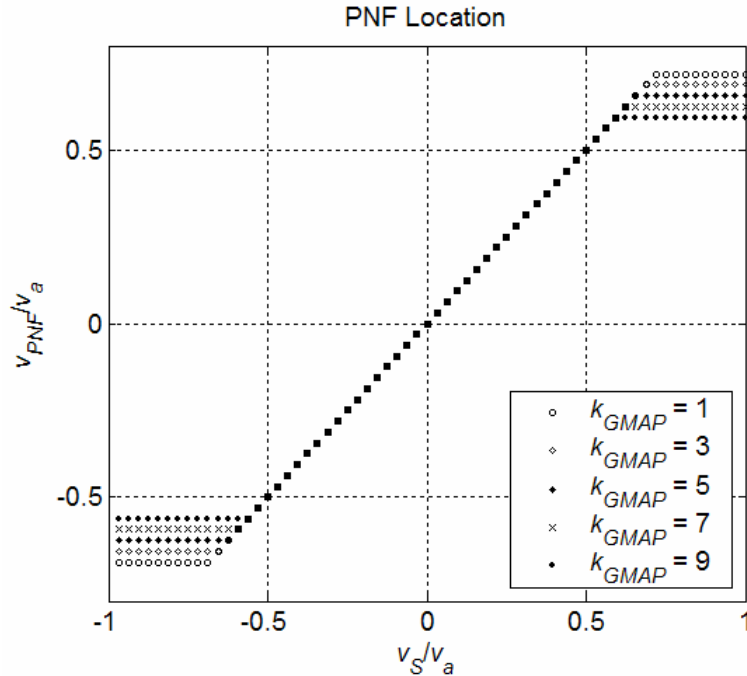


Fig. 3.3.2. Optimum PNF location as a function of the normalized strong-trip signal velocity for different values of  $k_{GMAP}$  (the number of spectral components that GMAP identifies as having clutter). The PNF location is also given in normalized units.

### 3.3.4. Addition of short-PRT spectrum width computation

In the August 2003 SZ-2 algorithm spectrum widths were computed from the long-PRT scan. These estimates were saved and then used during the short-PRT scan. Traditionally, spectrum widths are not computed from long-PRT data; still, estimates of velocities and spectrum widths from surveillance scans will be available in the forthcoming ORDA. Whereas it is well known that the mean velocity will be aliased three to four times more often than in the Doppler scans, the effects of long PRT on the Doppler spectrum width estimates are more subtle. These are described in appendix B, where it is demonstrated that estimators of spectrum width of sampled signals saturate at large values. The maximum value of spectrum width that can be measured

with the lag-one autocovariance estimator (Doviak and Zrnic 1993, eq. 6.27) is derived in appendix B; it is given by

$$\sigma_{v,\max} = \frac{v_a}{\pi} \left[ \ln \left( \frac{M^2 - 1}{M} \right) \right]^{1/2}. \quad (3.1)$$

For the parameters of the KOUN radar, formula (3.1) is plotted in Fig. 3.3.3; pertinent is the saturation or maximum measurable width which depends on the PRT and the number of samples.

Note that the wavelength is 11.09 cm and the unambiguous velocity is  $8.92 \text{ m s}^{-1}$ .

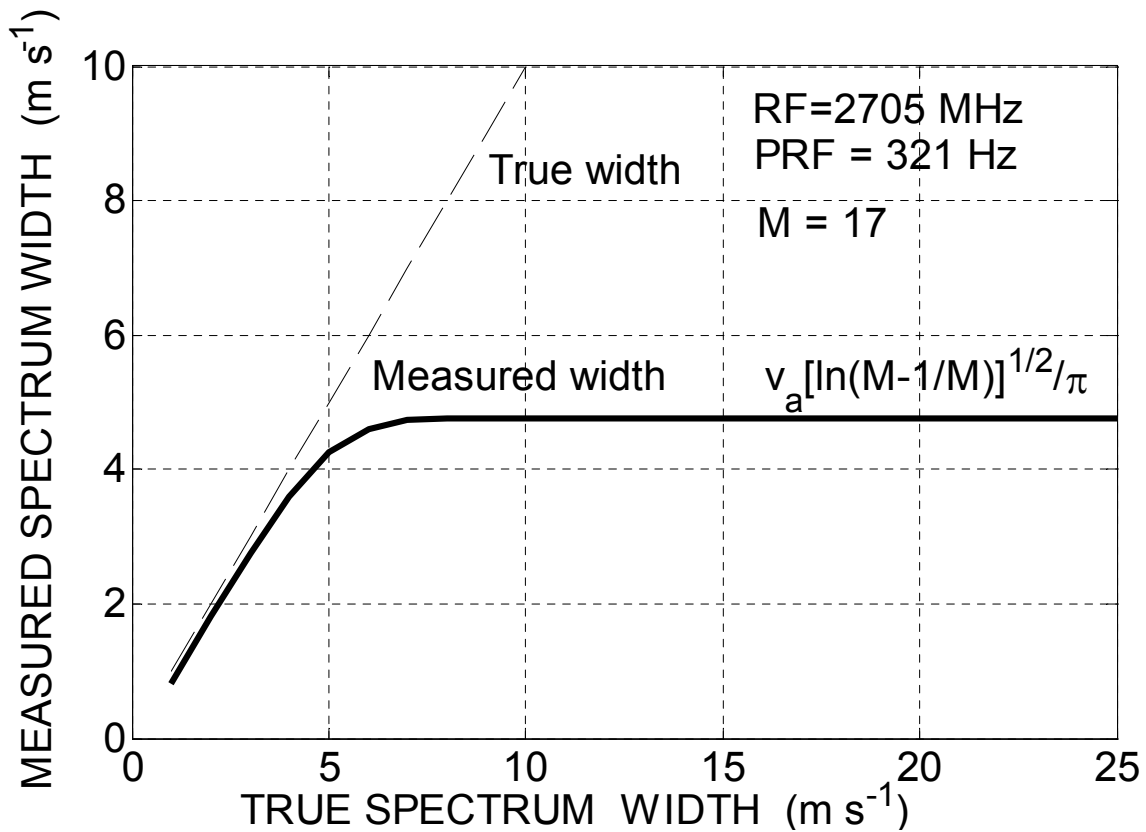


Fig. 3.3.3. Estimated vs. true spectrum width obtained from (3.1). The wavelength is for the KOUN radar and other parameters (surveillance PRF and number of samples  $M$ ) are standard on the WSR-88 network.

In Fig. 3.3.4 are estimates of spectrum widths along a radial obtained in the surveillance scan with 17 and 64 samples. No noise correction is applied; hence, the values beyond gate 1300 are caused by noise. Note the offset between the two curves; the one for  $M=17$  is consistently smaller (in noise and otherwise) than the one for  $M=64$  as predicted by (3.1). Furthermore, there is good agreement with theoretical prediction (3.1) indicated by the black horizontal lines in the region where noise alone is present.

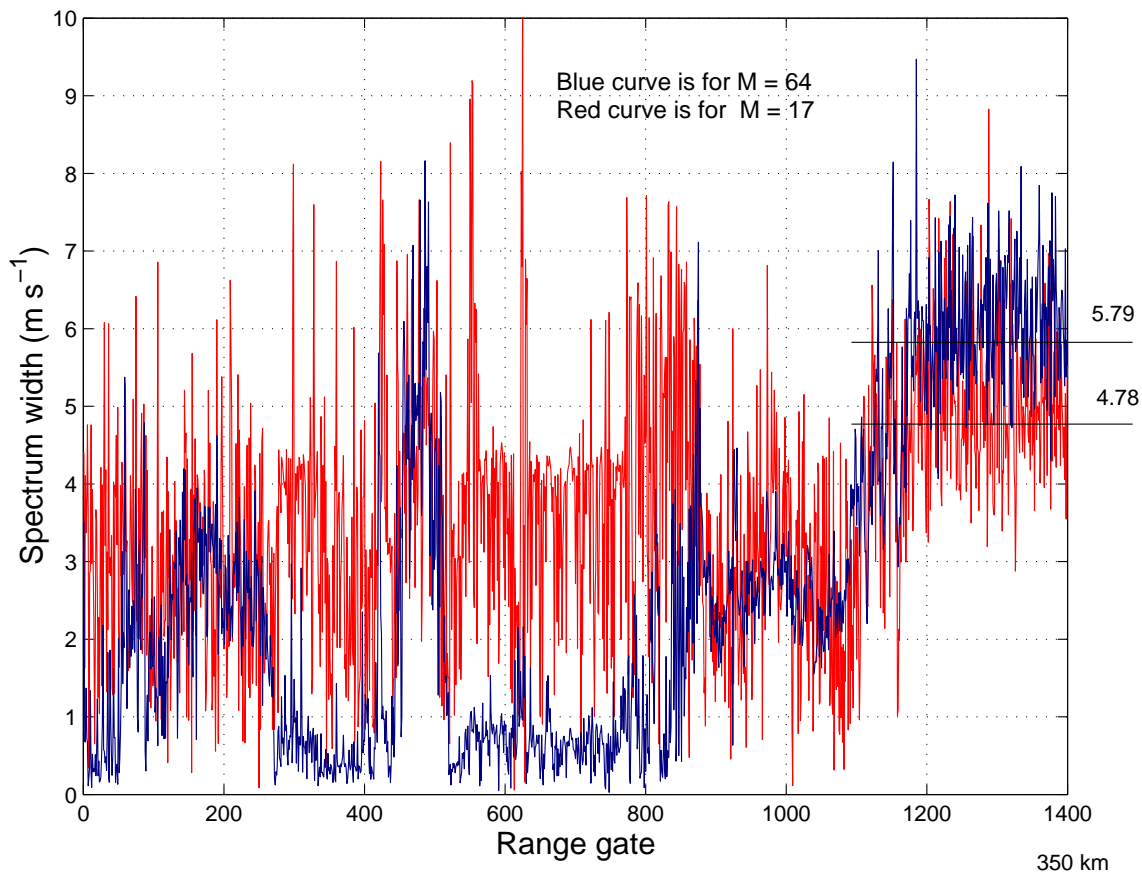


Fig. 3.3.4. Spectrum width estimates from autocovariance at lags 0 and 1; noise was not removed from the power estimates (lag 0 autocovariances). The radar operated with the PRT No. 1 (PRF = 321 Hz,  $r_a = 466$  km surveillance scan) when this data was acquired. Elevation is 0.5 deg, azimuth is 149 deg, date is Aug 25, 2002, and data to 350 km are displayed.

The estimator of spectrum width for the standard surveillance scan ( $M = 17$ ) saturates at  $4.78 \text{ m s}^{-1}$ . At a true width of  $5 \text{ m s}^{-1}$  the negative bias is already  $0.7 \text{ m s}^{-1}$  or 14 % (Fig. 3.3.3). For the majority of storm situations this might not be a problem as Fang et al. (2004) indicate that the median values in most weather events are about  $2 \text{ m s}^{-1}$ . But in strong squall lines the spectrum width can exceed  $4 \text{ m s}^{-1}$  (Fang et al. 2004); this means that in such events about one half of spectrum widths will not be measured in the long-PRT mode and therefore should be censored.

According to the previous discussion, it would be beneficial if the spectrum widths were estimated from the short-PRT data. In the current version of the SZ-2 algorithm we propose to use the short PRT for estimating the spectrum width of the strong trip echo and the long PRT for the spectrum width of the weak trip (overlaid) echo. From the preceding discussion it follows that the censored areas in the spectrum width field can be larger than censored areas in the velocity field. Even then, the long PRT will provide spectrum widths in significantly bigger area than possible without it. Spectrum width estimates using the deconvolution in the SZ-2 algorithm should be evaluated and compared (on data) with those obtained from long PRT scans. Thereafter, it may be possible to devise an optimum combination of the two which could be included in the algorithm.

### 3.3.5. *Refinement of censoring rules and thresholds*

The SZ-2 algorithm reported in August 2003 included the basic SNR censoring whereby only significant returns are processed, and censoring based on the recovery region for weak trip velocity (i.e., the plots of standard error of  $v_2$  on the  $S_1/S_2$  vs.  $\sigma_1$  plane). Additional censoring rules are required if dealing with clutter in any trip or if considering the possibility of overlaid

clutter (the full set of censoring rules is discussed in the next section). Moreover, old censoring thresholds should be refined to include the effects of the Blackman window and GMAP on the accuracy of estimates. The plots in section 2.2 are a good starting point for the definitions of these thresholds.

### **3.4. The recommended SZ-2 algorithm**

Based on the studies documented above and similar investigations by NCAR, a joint algorithm recommendation was completed earlier this year (FY2004 NSSL-NCAR interim report dated June 1, 2004). The recommended SZ-2 implementation is by-in-large an extension of the August 2003 algorithm with the following important changes: (1) ground clutter is no longer assumed to be only in the first trip, (2) GMAP is used as the clutter filter, and (3) censoring logic and thresholds were updated. The algorithm is briefly described next; the reader is referred to the aforementioned report for a detailed description of the proposed SZ-2 algorithm. A short list of errata for this report was released soon after the report was completed and delivered. This was timely distributed to key ROC personnel and is included in appendix C.

#### *3.4.1. The algorithm fundamentals*

The proposed algorithm involves two scans at the same elevation angle. The first one uses a long PRT and no phase coding. This scan is used to obtain power (reflectivity) and spectrum width estimates from non-overlaid echoes. In addition to these variables, the power removed by GMAP ( $P_{REM}$ ) is saved. The second scan uses a short PRT with SZ(8/64) phase coding and returns Doppler velocities and spectrum widths from likely overlaid signals. This is the essence of the SZ-2 algorithm; the basic steps are summarized as follows:

- 1) Determination of overlaid trips: Long-PRT signal powers are used to determine the (potentially) recoverable trips
- 2) Determination of ground clutter location: Location of ground clutter is determined according to the bypass map. Three cases are considered: (1) no clutter in any trips, (2) clutter in one trip, and (3) clutter in multiple trips
- 3) Data windowing
- 4) Cohering to trip with ground clutter
- 5) Filtering ground clutter using GMAP
- 6) Cohering to trips with recoverable signals
- 7) Computation of total power
- 8) Computation of lag-one correlations for cohered signals
- 9) Determination of strong and weak trips: lag-one correlations from the previous step are used in this determination
- 10) Computation of strong trip velocity
- 11) Processing notch filtering: This frequency-domain ideal notch filter removes most of the strong-trip signal spectrum, leaving two replicas of the modulated weak-trip signal spectrum
- 12) Computation of total weak trip power: This includes all the powers except for what the processing notch filter removed

13) Cohering to weak trip

14) Computation of weak trip lag-one correlation

15) Computation of weak trip velocity

16) Computation of strong and weak trip powers: These are the “actual” powers of the strong and weak trip signals

17) Computation of strong trip spectrum width

18) Censoring: This is explained next in more detail

### 3.4.2. *Censoring rules*

Censoring in the SZ-2 algorithm is used to maintain data quality under situations that preclude the recovery of one or more overlaid echoes. Censored range cells may be encoded as noise-like or overlaid-like returns. Noise-like gates correspond to those locations in which the received powers are not significant; these are usually encoded in black on displays. Gates with overlaid-like returns indicate that “something” is in those locations, but its characteristics (i.e., reflectivity, Doppler velocity, and/or spectrum width) cannot be reliably determined. A purple color (usually referred to as the “purple haze”) is used for these cells on displays.

In the SZ-2 algorithm, censoring can occur only on the Doppler velocity or spectrum width fields, since the reflectivity is determined from a long-PRT, non-phase-coded scan. Velocities and spectrum widths are censored under the following conditions:

- 1) Low signal-to-noise ratio in the long-PRT scan: Long-PRT powers that fall below  $K_{SNR}$  times the noise power are considered non significant. Range gates with non-significant powers are tagged as having noise-like returns (encoded in black).  $K_{SNR}$  is the SNR threshold in the VCP definition.
- 2) Low signal-to-noise ratio in the short-PRT scan: Short-PRT powers that fall below  $K_{SNR}$  times the noise power are considered non significant. This rule is necessary in case of significant advection of the weather phenomena. That is, especially at the edges of storm cells, range gates that exhibit significant powers during the long-PRT scan could have non-significant power during the short-PRT scan due to advection.
- 3) Low coherent-to-incoherent-signal ratio (SNR\*): The SZ(8/64) code is such that if the phase-coded time series is cohered for a given trip, all out-of-trip echoes appear roughly as white noise. Hence, the standard error of estimates for the velocity and spectrum width of the cohered trip will be affected by an equivalent SNR (the SNR\*) computed as the ratio of the coherent power to the sum of incoherent powers plus noise. Range gates with SNR\* below  $K_s$  or  $K_w$  for the strong or weak trip, respectively, are tagged as overlaid-like returns.
- 4) Outside the recovery region for weak trip velocity: The recovery of weak trip velocity is limited by the strong-to-weak power ratio ( $S_1/S_2$ ) and the spectrum widths of both strong and weak trip signals ( $\sigma_{v1}$  and  $\sigma_{v2}$ ). Sachidananda et al. (1998) performed simulation studies and plotted the standard error of weak trip velocities on the  $S_1/S_2$  vs.  $\sigma_{v1}$  plane with  $\sigma_{v2}$  as a parameter. Based on these plots, we can define a recovery region for weak trip velocities in which estimate errors are predicted to be within required levels. Two

regions are defined via a parameter  $K_r$ , one for narrow and one for wide weak trip spectrum widths ( $\sigma_{v2}$ ).  $K_r$  is the maximum  $S_1/S_2$  ratio for recovery of the weaker trip and is a function of the normalized strong and weak trip spectrum widths ( $\sigma_{vn1}$  and  $\sigma_{vn2}$ ) as

$$K_r(\sigma_{vn1}, \sigma_{vn2}) = \begin{cases} 10^{C_T(\sigma_{vn2})/10}, & \sigma_{vn1} < C_I(\sigma_{vn2}) \\ 10^{\{C_S(\sigma_{vn2})[\sigma_{vn1} - C_I(\sigma_{vn2})] + C_T(\sigma_{vn2})\}/10}, & \sigma_{vn1} \geq C_I(\sigma_{vn2}) \end{cases},$$

where  $C_T$  is the threshold,  $C_S$  is the slope and  $C_I$  is the intercept all of which depend on  $\sigma_{vn2}$ . Weak-trip range cells with parameters lying outside the recovery region for weak-trip velocity are tagged as overlaid-like returns.

- 5) High clutter-to-signal ratio: The clutter filtering process is imperfect in that it removes most of the clutter power but always leaves a clutter residue in the skirts of the clutter spectrum. This effect is detrimental especially if the clutter power is much stronger than the strongest weather signal. In such cases, recovery of overlaid weather signal parameters is significantly impaired by clutter residue and data from these locations must be censored. Clutter power is obtained from the long-PRT scan using GMAP's removed power ( $P_{REM}$ ), which makes sense here because we are interested in large clutter powers (see Section 2.2). This censoring rule comes into play if the clutter power is  $K_{CSR}$  (or more) times larger than the signal power. Two thresholds are available, one for the recovery of the strong trip ( $K_{CSR1}$ ) and one for the recovery of the weak trip ( $K_{CSR2}$ ).
- 6) Clutter location: As discussed in section 2.2, weak trip recovery is feasible if clutter is located in only one trip and that trip is the one with the strongest signal. If these conditions are not met, weak trip recovery is not possible and the corresponding range locations are censored (tagged as overlaid-like returns).

- 7) Large spectrum widths from the long-PRT scan: As explained in 3.3.4, saturation of spectrum width estimates is worse for estimates derived from long-PRT data, and these estimates are used for the weak-trip spectrum widths. Therefore, if the measured weak-trip spectrum width is close to the saturation level, it is impossible to tell whether saturation occurred or not. Locations corresponding to weak trips with spectrum widths larger than  $\sigma_{vmax}$  must be censored to indicate their unreliable nature.  $\sigma_{vmax}$  is chosen below the saturation level but close to it.
- 8) Triple or quadruple overlay: the SZ-2 algorithm can recover at most two overlaid trips out of a possible maximum of four. Hence, the weaker trips cannot be recovered in the case of a triple or quadruple overlay. Those range locations with 3<sup>rd</sup> or 4<sup>th</sup> strongest powers in a multiple overlay situation are censored and contribute to the purple haze in the SZ-2 algorithm.

### 3.4.3. *Examples on real weather data*

SZ phase coded data was collected using NSSL's KOUN radar in Norman, OK. An experimental VCP (No. 43 described in report 7) was designed to compare the performance of the SZ-2 algorithm with the legacy split cut processing. The VCP covers the lower elevation angles and consists of groups of five scans at each elevation angle. Each group contains a non-phase-coded long-PRT scan, phase-coded and non-phase-coded medium-PRT scans, and phase-coded and non-phase-coded short-PRT scans.

The case in figures 3.4.1 through 3.4.4 was obtained on October 8, 2002 at 15:11 GMT. KOUN operated with the experimental VCP described above. The long, medium, and short PRTs are  $T_{long} = 3.107$  ms ( $r_a = 466$  km),  $T_{medium} = 1.17$  ms ( $r_a = 175$  km), and  $T_{short} = 0.78$  ms

( $r_a = 117$  km). The number of pulses in the dwell time is  $M = 15$  for the long PRT and  $M = 64$  for the medium and short PRTs. The corresponding maximum unambiguous velocities are  $v_a = 23.75$  m s<sup>-1</sup> and  $v_a = 35.52$  m s<sup>-1</sup> for the medium and short PRTs, respectively.

Figure 3.4.1 shows the reflectivity PPI display from the first scan that uses a long PRT at an elevation angle of 0.5 deg. Figures 3.4.2 and 3.4.3 contain the Doppler velocity PPI displays obtained using legacy and SZ-2 processing for the medium and short PRTs at the same elevation angle. As expected, Doppler velocity displays obtained with legacy-type processing are significantly obscured by the purple haze which indicates the presence of unresolvable overlaid echoes. On the other hand, the SZ-2 algorithm successfully recovers velocities of the two strongest overlaid echoes.

An additional limitation observed in these figures is that all NEXRAD radars currently display velocities only up to 230 km; with the SZ-2 algorithm velocities can be displayed up to about 460 km. Whereas velocity estimates agree quite well in places where both legacy and SZ-2 processing show valid data, estimates obtained with the SZ-2 algorithm can exhibit larger errors under the conditions described before and therefore are censored. Figure 3.4.4 shows the reasons for censoring in a PPI display. Plots of this kind are very useful for tuning the censoring thresholds.

In general, range and velocity ambiguity mitigation schemes work better with longer PRTs because overlaid echoes are more likely to occur at shorter PRTs. This is evident when comparing Figures 3.4.2.b and 3.4.3.b. Using the short PRT provides the largest maximum unambiguous velocity but also leads to cases with triple overlay from which only two trips can

be resolved. Using the medium PRT leads to a smaller  $v_a$  but at most two trips are overlaid at any given range location.

Additional cases with varied weather situations can be found on our web site at [http://cimms.ou.edu/rvamb/SZ/SZ-2\\_Algorithm.htm](http://cimms.ou.edu/rvamb/SZ/SZ-2_Algorithm.htm).

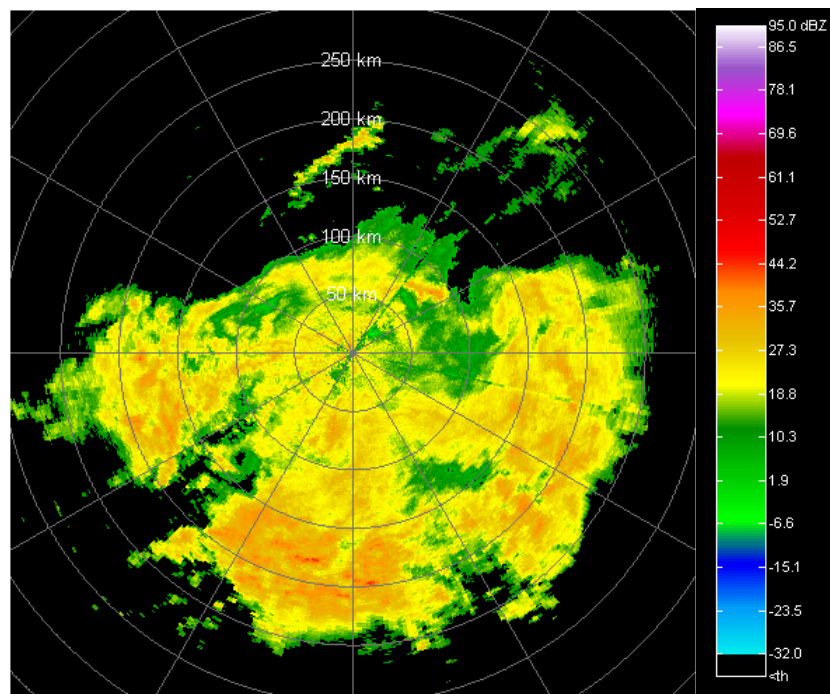


Fig. 3.4.1. Reflectivity PPI display. Range rings are 50 km apart.

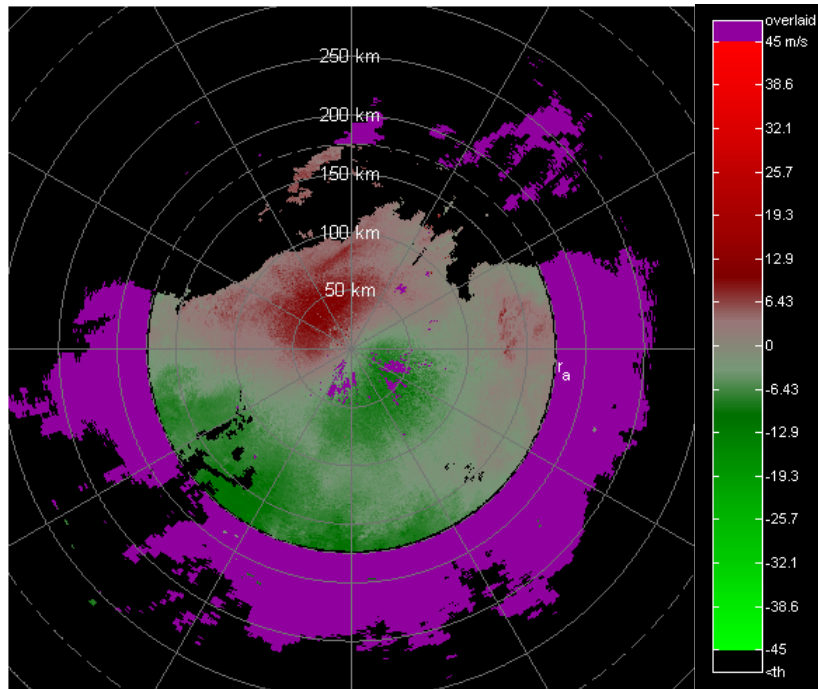


Fig. 3.4.2 (a) Doppler velocity PPI display obtained from the medium PRT using standard legacy processing.

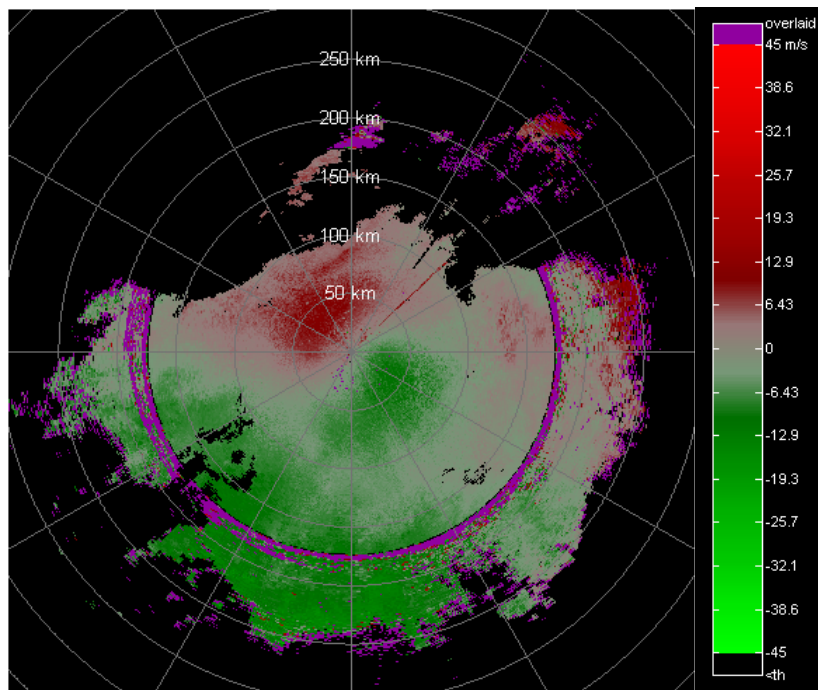


Fig. 3.4.2 (b) Doppler velocity PPI display obtained from the medium PRT using the SZ-2 algorithm.

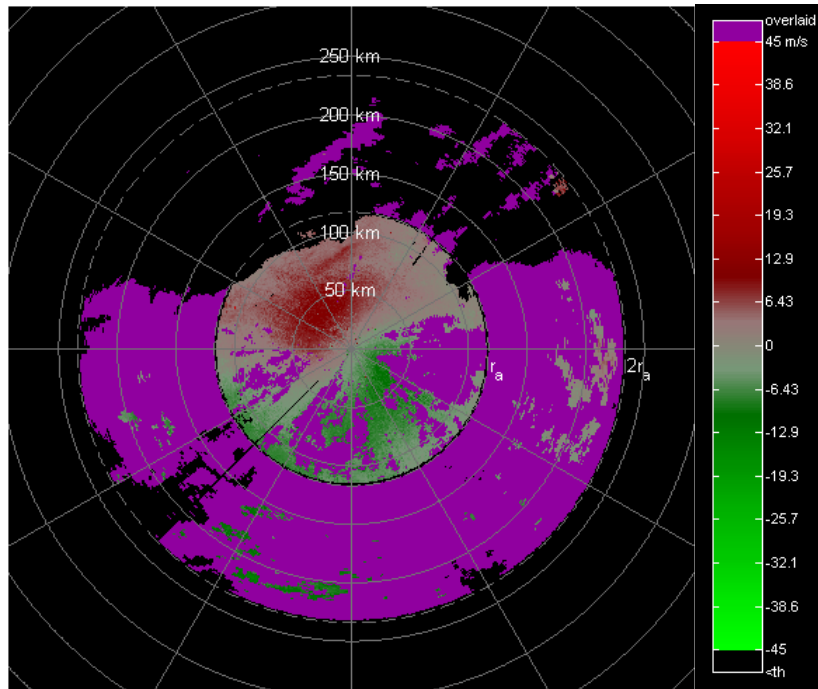


Fig. 3.4.3 (a) Doppler velocity PPI display obtained from the short PRT using standard legacy processing.

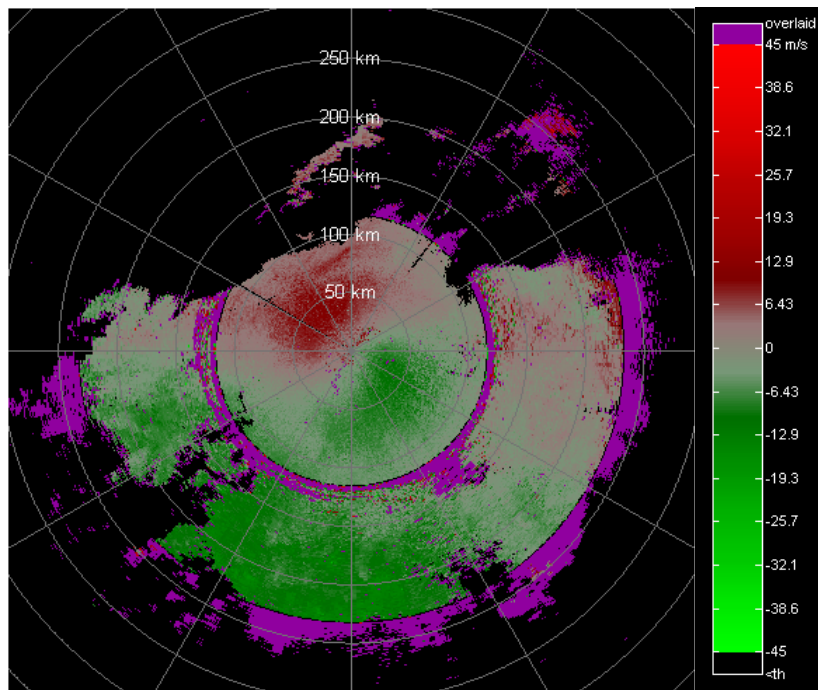


Fig. 3.4.3 (b) Doppler velocity PPI display obtained from the short PRT using the SZ-2 algorithm.

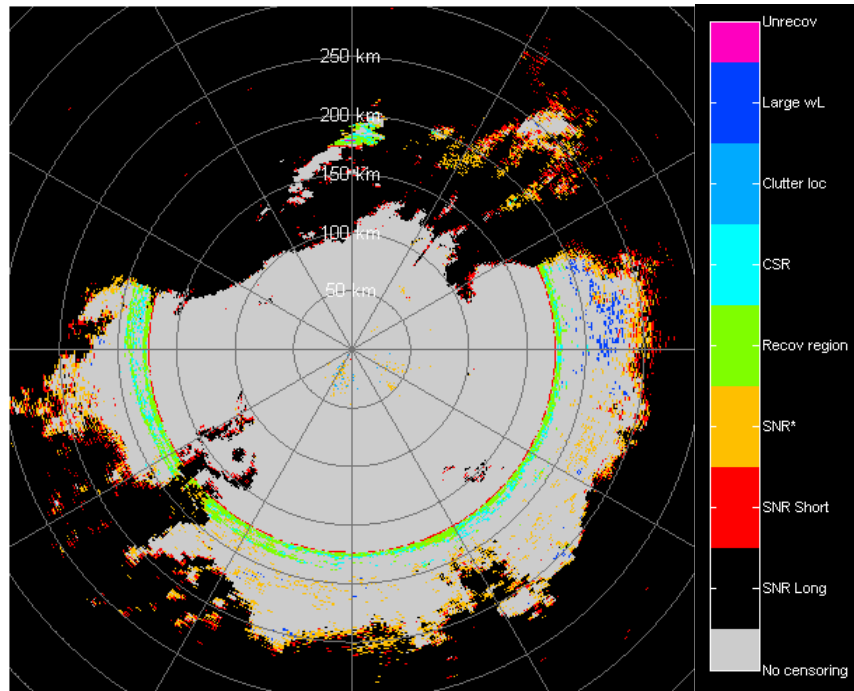


Fig. 3.4.4 (a) Censoring cases in a PPI display obtained from the medium PRT using the SZ-2 algorithm.

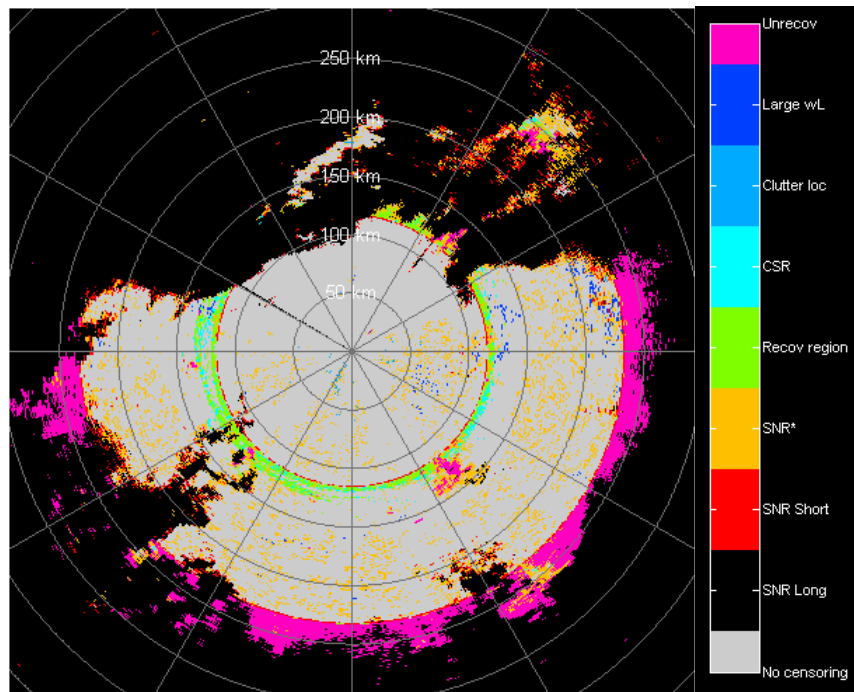


Fig. 3.4.4 (b) Censoring cases in a PPI display obtained from the short PRT using the SZ-2 algorithm.

### 3.5. Future enhancements to the SZ-2 algorithm

As demonstrated, the proposed SZ-2 algorithm works well. Indeed, compared to the techniques currently implemented in the legacy WSR-88D, the SZ-2 algorithm provides a significant improvement in range and velocity ambiguity mitigation. Nonetheless, we have already identified a few areas where there is room for improvement. These improvements are not proposed for the first implementation of the SZ-2 algorithm for several reasons. To begin with, most of these enhancements come at a large computational cost compared to the potential advantages that can be realized. Moreover, some of these techniques are still under investigation and being tested using real data, and their benefits have only been quantified from theoretical analyses. In conclusion, these improvements are proposed for later releases of the SZ-2 algorithm after detailed studies are completed and the involved agencies concur that the cost of adding these enhancements is commensurate with the improvements to the performance of the radar. Below is a summary of issues for future refinements of the SZ-2 algorithm.

#### 3.5.1. *Anomalous propagation clutter*

Clutter filter application is currently controlled with two maps: the bypass map and the clutter censor zones map. The former has information about the location of ground clutter within the radar's domain. The latter is defined by the operator upon observing evidence of anomalous propagation clutter. The filter is applied in those range locations where either map indicates the presence of clutter, therefore relying on the radar operator for the removal of AP clutter. This process can be automated (complementarily to the current capability or as a substitute) by using the removed power from GMAP during the long-PRT scan to identify range gates with significant clutter power. This information can be used to generate an AP clutter map that can be

combined with the legacy bypass map to generate a composite clutter map to be used in the ORDA.

### 3.5.2. *Strongly overlaid echoes*

In situations where the ratio of strong-to-weak-trip powers is small (less than about 5 dB), the distinction between strong and weak trips is arbitrary in the sense that either of the two strongest trips can be considered “the strong trip”. In the absence of a typical “weak trip”, recovery of overlaid echoes can proceed in a different way by treating both trips as the strong trip, or performing what was termed as to “double processing”. That is, the processing sequence becomes:

- 1) Cohering (clutter filtered time series) to the strong trip
- 2) Applying the PNF
- 3) Cohering to the weak trip
- 4) Computing weak trip velocity
- 5) Cohering (clutter filtered time series) to the weak trip
- 6) Applying the PNF
- 7) Cohering to the strong trip
- 8) Computing strong trip velocity

The performance of this algorithm must be evaluated and quantified using both simulated and real weather data.

### 3.5.3. *Spectrum width computation*

Weak trip spectrum widths computed during the long-PRT scan get saturated at values well below the usual scale. Therefore, it would be advantageous to estimate all spectrum widths from the short-PRT scan. Similarly to the standalone SZ-1 algorithm, a deconvolution technique can

be used to recover weak trip spectrum widths. However, this computationally expensive technique does not guarantee reliable estimates. The extent to which deconvolution will be effective for the estimation of spectrum widths has to be quantified using real weather data.

#### 4. Staggered PRT further results

This section deals with staggered PRT. The following is a list of ambitious tasks extracted from the FY04 statement of work dealing with staggered PRT.

1. Implement the spectral ground clutter filter (NSSL report 1999) on the Matlab SimSPS (Simulation of Signal Processing Subsystem). **(NSSL)**
2. Test the spectral ground clutter filter on time series data. Evaluate and quantify its performance. **(NSSL)**
3. Compare the results with those obtained on uniform time series data as well as with other schemes (e.g., the removal of DC power from the autocovariance). **(NSSL)**
4. Explore other alternatives for filtering ground clutter from staggered PRT sequences. **(NSSL)**
5. Determine errors in the spectral moments and compare to theoretical predictions and simulation results. **(NSSL)**
6. Extend the unambiguous range for reflectivity measurements from  $3/2$  of the short unambiguous range to twice the short unambiguous range both in the real time and off line algorithm. **(NSSL)**
7. Investigate the interplay between extended unambiguous velocity, dealiasing error, and stagger ratio so that optimum parameters can evolve. **(NSSL)**
8. Investigate limitation on spectrum width estimates from either uniform or staggered PRTs both with large separations. **(NSSL)**
9. Compare staggered PRT and phase coding techniques on time series data from the same events. Such metrics as % of obscured area (purple haze) and errors will be used. **(NCAR/NSSL)**

Next, we present a brief summary of the work done on the listed items. Due to intense occupation with phase coding we have not been able to quantify the performance of spectral ground clutter filter on time series data (part of item 2) but have examples to show its effectiveness. Neither have we attempted to quantify item 3 although we do have comparative images. Nonetheless, we are comparing qualitatively and on data the performance of various clutter filters with the one suggested for the staggered PRT (item 3). Concerning item 4, we have

looked at some other possibilities in the literature (e.g., Bagchi and Mitra 1999); so far we have not found a promising alternative and will continue to explore the topic. Further due to change of priorities we were not able to fulfill item 6.

The issue of large spectrum width estimation from lag one autocovariance is the same in staggered PRT as in uniform PRT (appendix A). The pulse separations in staggered PRT are generally longer than uniform PRTs for Doppler measurements, but are shorter than long PRTs in surveillance scans. Spectrum width estimates from the shorter of the two PRTs in the staggered scheme exhibit saturation at value of about  $10 \text{ m s}^{-1}$ . This is sufficiently large to exceed detection thresholds for hazardous turbulence by a good margin.

The spectral ground clutter filter (item 1) has been implemented on the Simulation of the Signal Processing Subsystem (SimSPS) in Matlab; detailed functional description will be provided in the subsequent report after we have sufficiently tested its performance on time series data. This will give us time to finalize the algorithm. Initial tests of the ground clutter filter are described in section 4.1.

Items 7, 8, and 9 from the list are exposed in sections 4.2, 4.3, and 4.4, respectively.

#### **4.1. Evaluation using time series data**

Clutter filtering in staggered PRT sequences is described in Sachidananda et al. (1999, 2001). Choice of window functions and clutter filter width are in Section 2 of this report, and we use the same notation herein.

In this section we apply the staggered PRT clutter filtering algorithm to actual radar time series data to demonstrate its ability to filter the clutter. The data was collected in the staggered PRT

mode and in the lowest elevation scan (0.5°) using the NSSL research radar on April 6, 2003. Strong ground clutter with clutter-to-noise ratio (CNR) as large as 90 dB is measured in some locations. The scan rate was somewhat slower ( $10^\circ \text{ s}^{-1}$ ) than the scan rate used in the VCP-11 (about  $20^\circ \text{ s}^{-1}$ ), hence the clutter spectrum width is narrower than what is encountered normally in an operational environment. Nevertheless, the performance of the clutter filter would be marginally different if the ground clutter spectrum width is twice the width in this scan and the number of samples is the same. This is because the main lobe of the window function is much wider than the clutter spectrum width, and hence, the clutter filter width is mainly determined by the window function. Note that if the number of available samples (dwell time) is reduced, then the performance of the filter would deteriorate. Quantitative determination of the effects of dwell time on ground clutter removal at the KOUN site will be made in the subsequent report.

In section 2, we have discussed ground clutter filtering at length; specifically, the optimum combination of the clutter filter width and the window function based on the CNR. This requires at least some approximate estimate of the CNR. One possible method of estimating the approximate CNR is

$$CNR_{\text{approx}} = [(S_1 + S_2 + S_N) (5/2)(5/2)] / (N \cdot p_{\text{noise}}),$$

where  $S_1$  is the spectral power of at zero Doppler,  $S_2$  is the spectral power at the adjacent positive Doppler,  $S_N$  is the spectral power at the adjacent negative Doppler (or Doppler line at the last  $N$ th coefficient), and  $p_{\text{noise}}$  is the spectral power (per coefficient) of the noise. The two  $5/2$  factors are to account for: (a) the inserted zeros (3 in the five places), and (b) the spread of the clutter spectral power (into five replicas). The staggered PRT spectrum has 5 unequal replicas, with the main one having  $2/5$  of the power.

The other option to estimate CNR is to use the clutter map of the radar. This second option is better and faster. It also avoids filtering the signal near zero velocity when the clutter is not present. If approximate clutter strength is known, we can also include the type of window and the clutter filter width to be used for each range location in the clutter map. In the present analysis of the data, we have used the first approach because the clutter map was not readily available. A simulation study indicates that the first approach gives a reasonably good estimate of the CNR and is adequate for selecting an optimum combination of the window and the clutter filter width. For a sequence length of 64 in this data set ( $N = 160$ ), the maximum  $q$  value is not more than 6 for the strongest of the ground clutter signals. In general, the  $q$  value increases by one for every 20 dB (approximately) increase in the CNR. Hence, an approximate CNR as outlined herein is adequate.

We chose one full 360 degree scan of the staggered PRT data from April 6 (Torres et al. 2003). The PRTs are  $T_1 = 1.2267$  ms and  $T_2 = 1.840$  ms. This provides an unambiguous range  $r_a = cT_1/2 = 184$  km, and an unambiguous velocity of  $45.2$  m s<sup>-1</sup>. The PPI display indicated no overlay in the 190° to 320° sector. The rest of the regions had some overlay. Hence we have selected data from this particular sector to try our algorithm on.

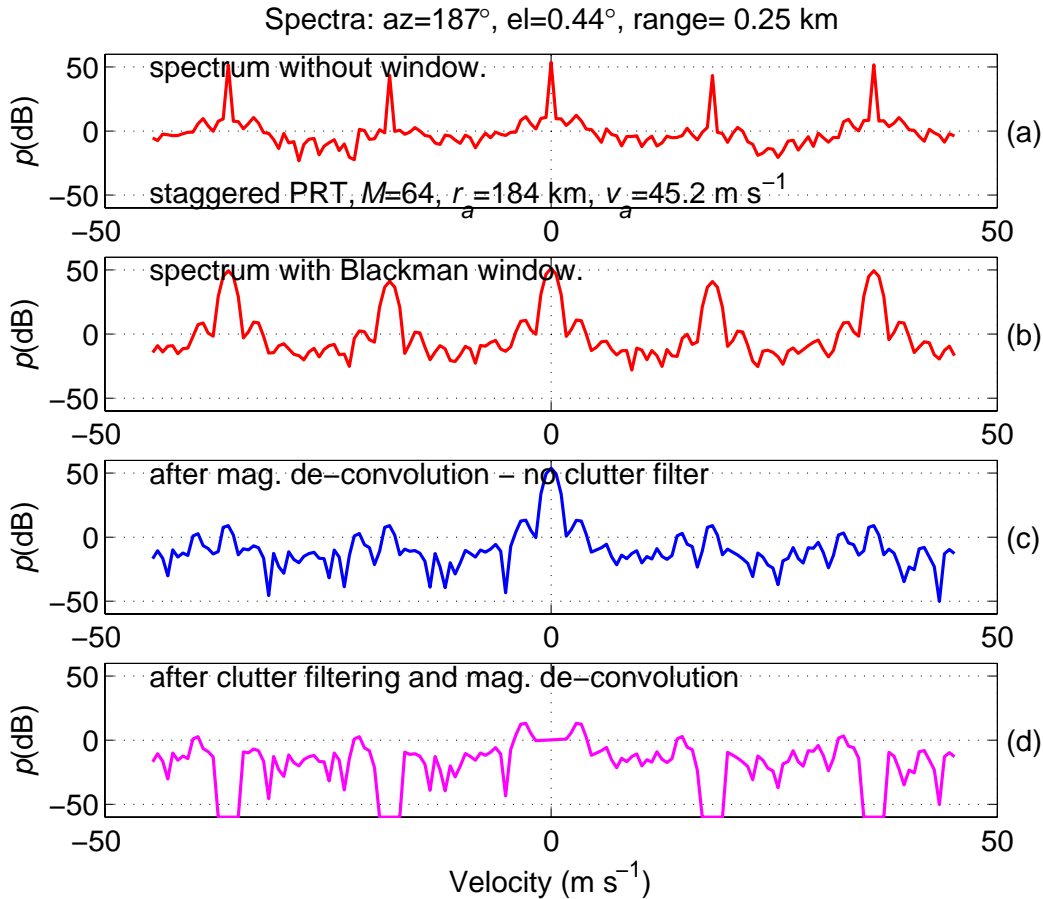


Fig. 4.1. Spectra from a staggered PRT sequence at one range location with large ground clutter, a sixty-cycle sidebands, and perhaps weather signal. Date is April 6, 2003 and the VCP was 46.

First, we examine some spectra which have strong and some which have weak ground clutter. Fig. 4.1 shows four spectra; the first one is the spectrum of the derived time series without applying any window; the second one is with the Blackman window. This range cell is the closest to the radar (250 m) and therefore has extremely strong ground clutter (estimated CNR = 94 dB). The two sidebands next to the clutter peak correspond to 60 Hz but we do not know its origin; suffice to say that it occurs at extremely large clutter powers (there was no indication of saturation as the sinusoidal modulation at 60 Hz can be clearly seen in the in-phase and quadrature phase components.) The rest of the spectral components (excluding the clutter and 60

Hz replicas) could be due to harmonics of 60 Hz or to imbedded weather signal (mean power,  $p = -0.78$  dB, noise at  $-55$  dB, relative values). Examination of the fields of Doppler velocities indicates that there is a weather signal with velocities close to zero in the vicinity of the radar. It is seen that the clutter spectrum has 5 weighted replicas corresponding to the staggered PRT code spectrum. After applying the Blackman window the main lobes are much wider, but the side lobe level has come down. The “other signal (60 Hz?)” can be seen overlapping the ground clutter peak (the mean velocity is  $0.2 \text{ m s}^{-1}$ ). The third spectrum is the spectrum after magnitude deconvolution but without filtering the clutter. It is clearly seen that all the five replicas are reduced to a single peak at zero Doppler. The “other signal” is also de-convolved and can be seen on either side of the main ground clutter lobe. It is also seen that there are four replicas of lower amplitude, apart from the one at zero Doppler. These are because the “other signal” spectrum does not satisfy the "narrow" criterion (i.e., it spreads over more than  $N/5$  coefficients). Whenever the spectral replicas *overlap one time*, the overlapped parts do not deconvolve fully into a single spectrum and then the four residuals have the same amplitude. This can be easily recognized in the Fig. 4.1.c. The last spectrum is obtained after clutter filtering and deconvolution. With  $n_c = 5$  ( $q = 3$ ), the main lobe of the clutter is deleted at zero Doppler. Since, the “other signal” is also located around zero velocity; the deleted coefficients are reconstructed approximately by the linear interpolation. The rest of the four places where the clutter peaks existed are set to zero.

We select another example where the spectra of the ground clutter and the weather signal do not overlap significantly, and the weather spectrum satisfies the "narrow" criterion fairly well. In Fig. 4.2 we again show similar four spectra from another range cell. The ground clutter is weaker than in the previous example ( $\text{CNR} = 43$  dB), and the signal and clutter spectra do not overlap

significantly. With a clutter filter width,  $n_c = 5$ , the clutter is completely eliminated (see Fig. 4.2.d), and the signal is more or less fully deconvolved; the residuals are nearly at the noise floor of the receiver (noise floor = -55 dB). This indicates that the signal spectrum satisfies the "narrow" criterion reasonably well in this case.

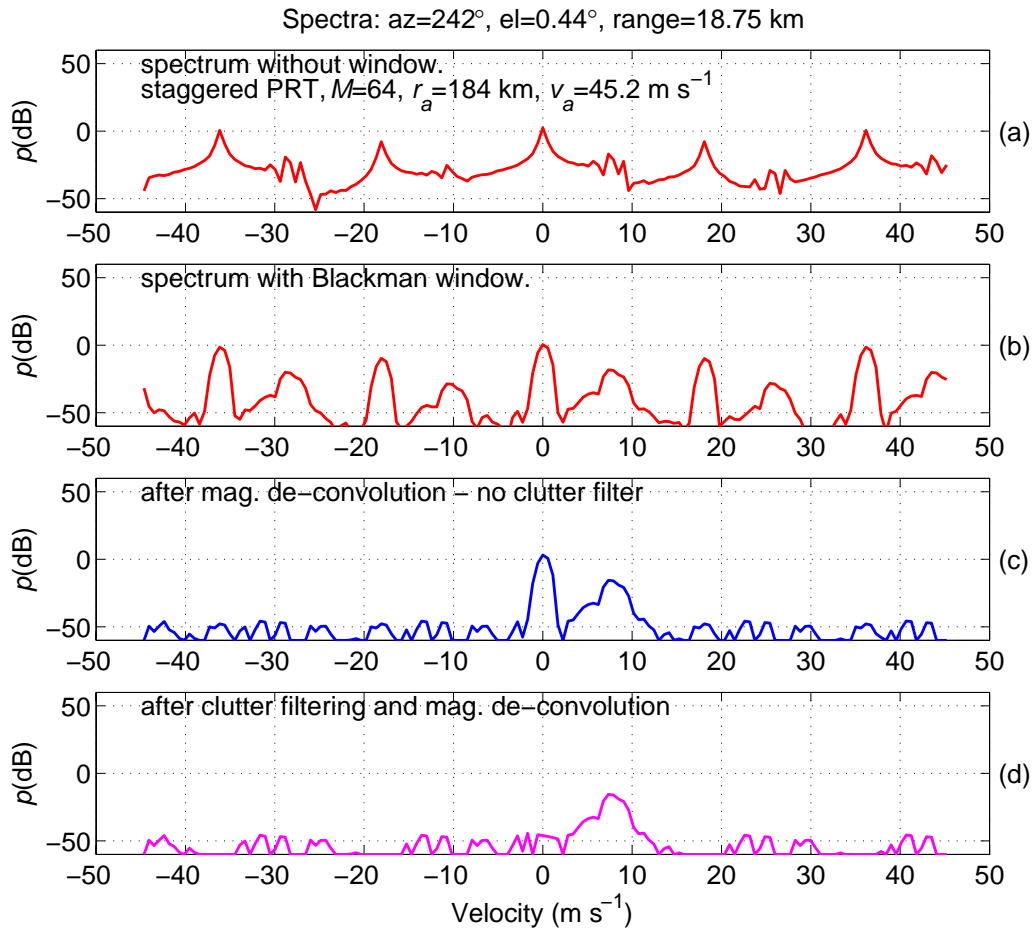


Fig. 4.2. Spectra from a staggered PRT sequence at one range location. The spectra of ground clutter and weather signal do not overlap. Date is April 6, 2003 (VCP-46).

In a third example (Fig. 4.3), we choose a case with a strong signal and a weak clutter (CSR=-8.3 dB). With the application of the window the clutter signal is clearly seen. With  $n_c = 5$ , the clutter is filtered and the lost signal is reconstructed by interpolation near zero velocity.

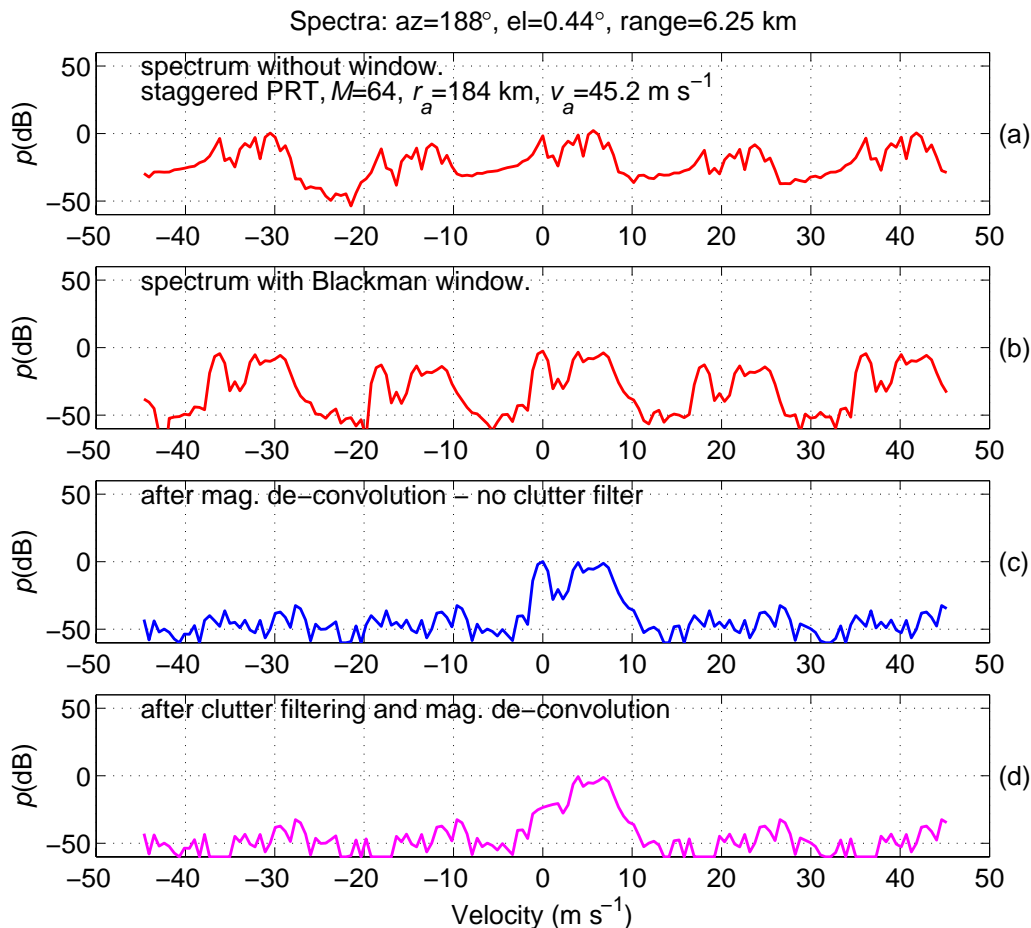


Fig. 4.3. Spectra from a staggered PRT sequence at one range location with weak ground clutter and strong weather signal. Date is April 6, 2003 (VCP-46).

In the next couple of figures we show spectral parameters along a radial with and without the clutter filter. The clutter filter is applied only if there is significant ground clutter power present in the spectra. The criterion used is: if the clutter power estimated from only three spectral

coefficients centered on zero velocity is more than a tenth of the total power in the spectrum, we apply the clutter filter. This criterion was used because the clutter map was not readily available. Because of this criterion, the clutter filter comes on at a few places where there is no clutter but a strong weather signal is present at zero velocity. This situation can easily be eliminated using a clutter map. In Fig. 4.4 and 4.5 the three spectral moment estimates are shown along the radial with and without the clutter filter. The dotted lines are without the clutter filter, and the continuous lines are with the clutter filter applied as per the criterion indicated above. The bar at the bottom (in the reflectivity plot) indicates the ranges at which the clutter filter is applied. The range gates are spaced 0.25 km apart. It can be seen that wherever strong ground clutter is present, the velocity is nearly zero and spectrum width is also below  $2 \text{ m s}^{-1}$ . After the clutter is filtered, the velocity and width are recovered along with the weather signal power.

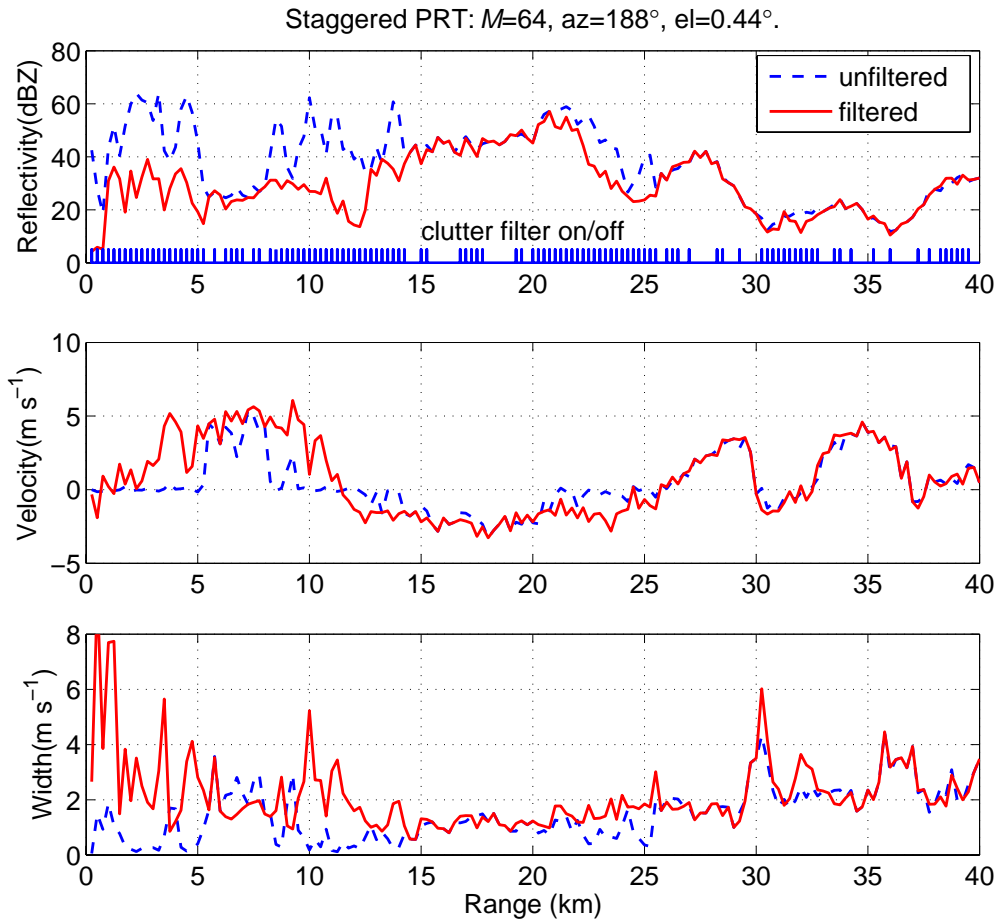


Fig. 4.4. Reflectivity, velocity, and spectrum width estimates along the radial at  $188^\circ$  with and without clutter filtering. Date is April 6, 2003 (VCP-46).

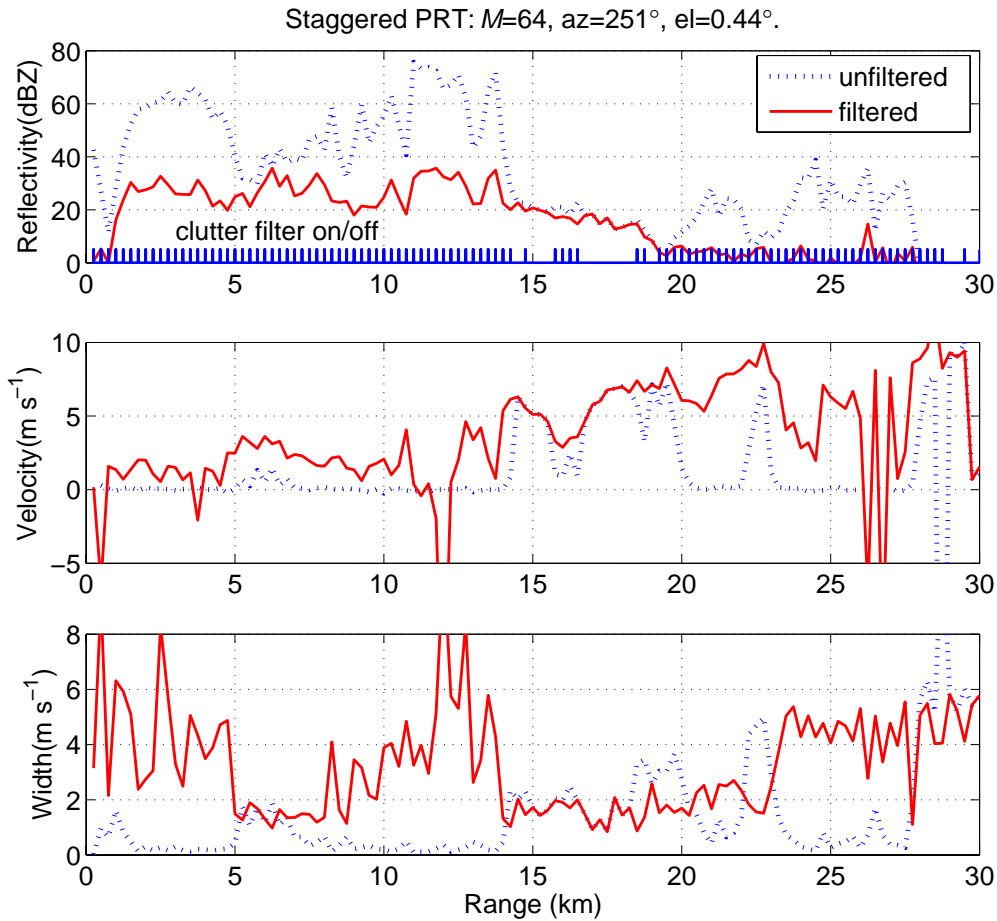


Fig. 4.5. Reflectivity, velocity, and spectrum width estimates along the radial at  $251^\circ$  with and without clutter filtering. Date is April 6, 2003 (VCP-46).

Next, we present fields of reflectivity factor and Doppler velocity for the same data as presented in Fig. 4.1 to 4.5. Because our aim is to demonstrate clutter filtering capabilities and because clutter is strongest close to the radar, we show these fields up to the range of 30 km (Fig. 4.6). There were several large and strong storms in the radar coverage area (see Fig. 3.23 to 3.30 in Torres et al. 2004), but within 30 km of the radar cells (to the south, south east, and east) were small and weak.

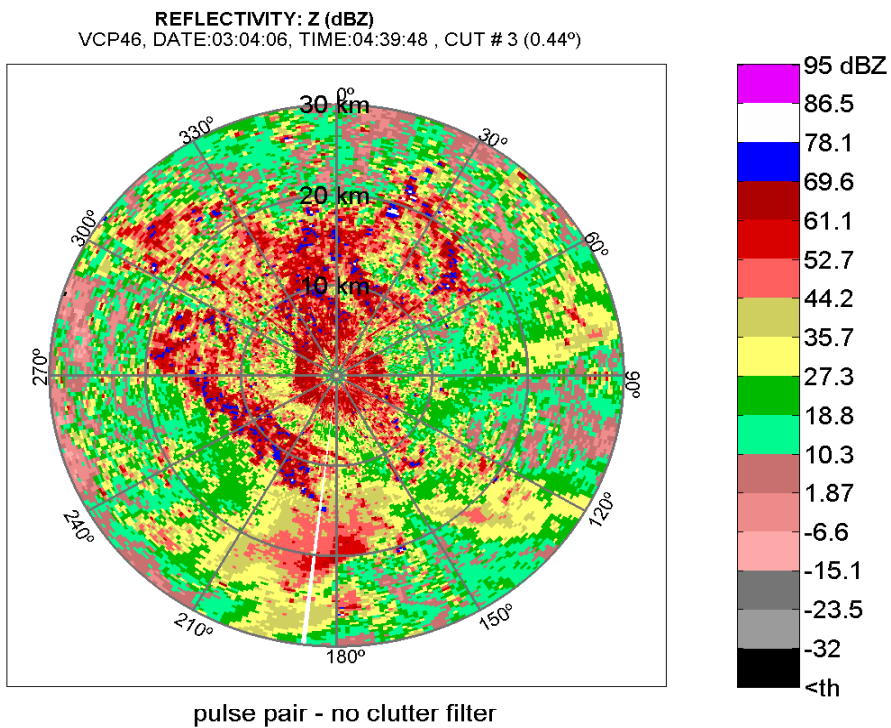


Fig. 4.6. Reflectivity field (April 6, 2003) up to the range of 30 km, without filter.

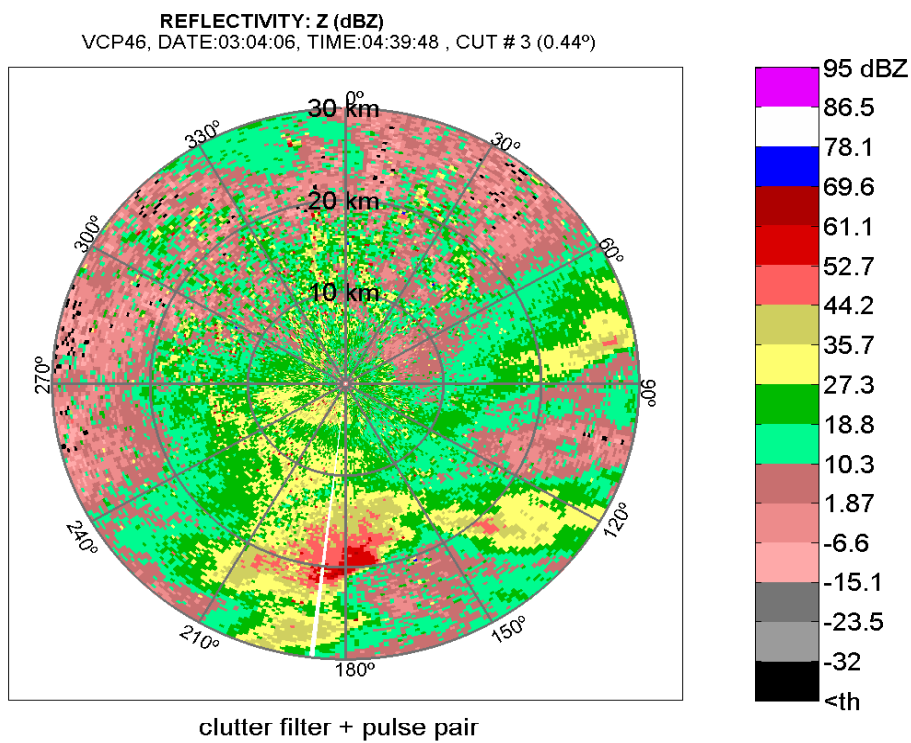


Fig. 4.7. Same as in 4.6 but clutter filter was applied.

Note the significant reduction in clutter powers after application of the clutter filter (Fig. 4.7). Very strong ground clutter (as large as 80 dBZ could be seen in Fig. 4.6) is nearly eliminated in the next plot with the clutter filter. Here again, we have used the approximate CNR estimated from just three spectral coefficients around zero velocity to determine the window and the clutter filter width. The clutter filter is applied whenever the estimated ground clutter power exceeded a tenth of the total power in the spectrum.

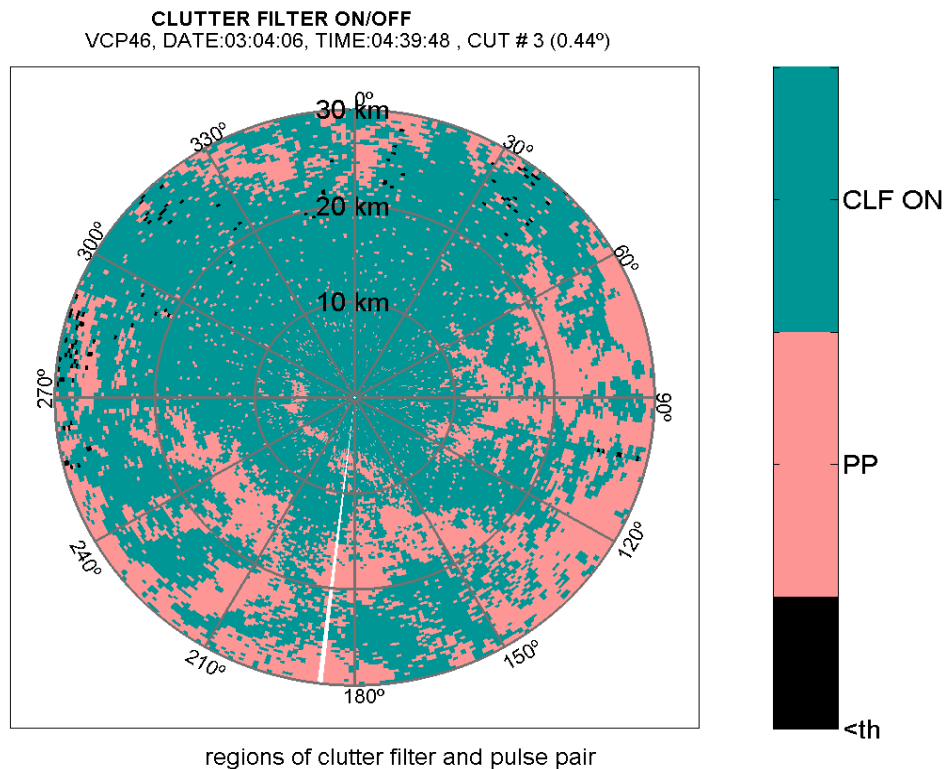


Fig. 4.8. Locations where clutter filter has been applied are in aquamarine color.

The three cells to the south, southeast, and east are now clearly discernible (Fig. 4.7). Some clutter residue is apparent to the southwest at 10 km which is from an elevated ridge. Clutter

residue to the north (between 10 and 20 km range) is from the urban Oklahoma City area. The locations where clutter filter was applied are indicated in Fig. 4.8.

The velocity fields for the same scan and without clutter filtering and with the filter applied (as indicated in Fig. 4.8) are in Fig. 4.9 and 4.10. Continuity and structure of the velocity field in Fig. 4.10 indicates that much of the winds are correctly depicted in the region of storm cells (from 45° to 270° in azimuth). The speckles to the north are caused by the mix of clutter residue and very weak signal in clear air. No attempt has been made to identify such unreliable data; nonetheless, this can be done relatively easily from the measured CNR and signal to clutter ratios.

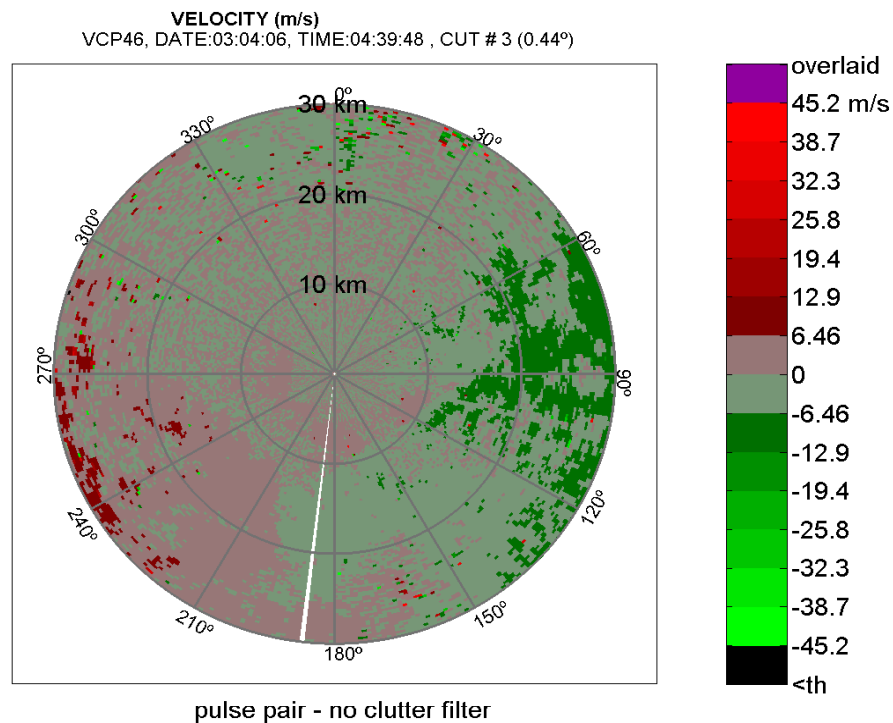


Fig. 4.9. Velocity field, clutter filter is off (April 6, 2003).

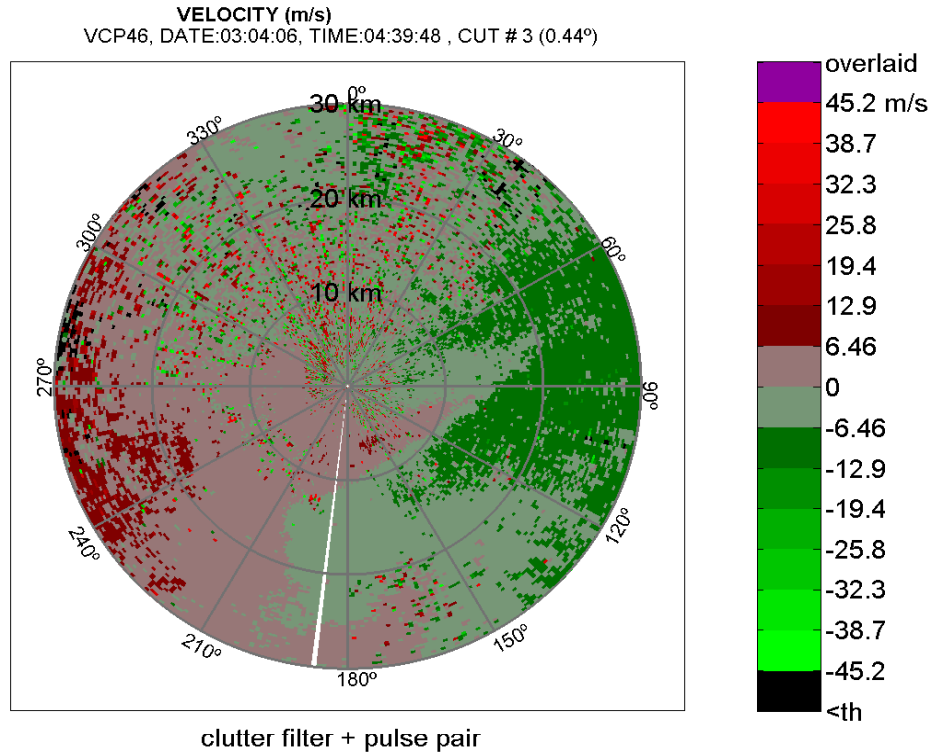


Fig. 4.10. Same as in Fig. 4.9 but clutter filter has been applied.

#### 4.2. Errors in spectral moments, experimental verification

Real-time implementation of the staggered PRT technique was completed on NSSL's KOUN research RDA in 2003 and functional description of that implementation has been provided by Torres et al. (2003). Neither now nor then was there a formal requirement to produce the Algorithm Enunciation Language (AEL) description of this algorithm; evidently this is an inadvertent omission. We are including this AEL in appendix F because it will be needed sooner or later. Over the last two years, we have collected staggered PRT time-series data for quite a number of weather events (a list and description of events can be found in appendix A and last year's reports). For a few of these cases, we deviated from the usual constant elevation scanning

and collected data with a stationary antenna. The statistical performance of the velocity dealiasing algorithm can be obtained using this type of data. Fig. 4.2.1 shows the results on a set of 200 radials of weather data recorded on May 16, 2003. The antenna was in a stationary position at an elevation of 1.5 deg. The staggered PRTs are  $T_1 = 1.6$  ms and  $T_2 = 2.4$  ms (stagger ratio  $\kappa = 2/3$ ), and the number of samples  $M = 32$ . The number of dealiasing rules was chosen as 5 (these are discussed in the next section), providing a maximum unambiguous velocity of  $45.17 \text{ m s}^{-1}$ . Fig. 4.2.1.a shows the mean SNR (over 200 radials) for each range location. Only returns between 160 and 230 km are considered, and just the locations with significant powers are processed; i.e., we examine locations where the power is above the SNR threshold  $T_{SNR}$  ( $T_{SNR} = 8$  dB). Fig. 4.2.1.b shows the mean spectrum width for each range location with significant returns; spectrum widths of up to  $10 \text{ m s}^{-1}$  can be observed.

The dealiased Doppler velocity is computed for each radial as described in Torres et al. (2004) and its mean is plotted in Fig. 4.2.1.c. At some locations, significant differences may be observed among the 200 velocity estimates. This is because all the estimates are not dealiased to the same Nyquist interval (from radial to radial, the estimates of  $v_1$  and  $v_2$  may not be the same due to the time delay between radials and the errors in the autocorrelation estimates, which may lead to catastrophic errors). To avoid unrealistic statistics, the outliers are removed from the data. That is, a histogram of Nyquist interval numbers is computed for the 200 radials, and only the radials in which the dealiased velocity belongs to the predominant Nyquist interval are considered in subsequent analyses. Still, if the determination of the proper Nyquist interval becomes ambiguous because two or more intervals have almost the same propensity of occurrence, a continuity rule is applied, and the predominant Nyquist interval is obtained from the previous range location. Smooth variations in the velocity profile of Fig. 4.2.1.c. confirm that velocity

estimates are dealiased to the correct Nyquist interval (after discarding the outliers). Still, a few catastrophic errors occurred between 180 and 185 km, where the spectrum width is in excess of  $8 \text{ m s}^{-1}$ . Fig. 4.2.1.d depicts the normalized standard deviations of the velocity obtained both from the data and theoretical predictions [c.f. (6.21) of Doviak and Zrnić 1993] using the estimated spectrum width (note that unlike the pulse-pair algorithm which uses contiguous pairs, velocity estimates in the staggered PRT technique are obtained from spaced pairs).

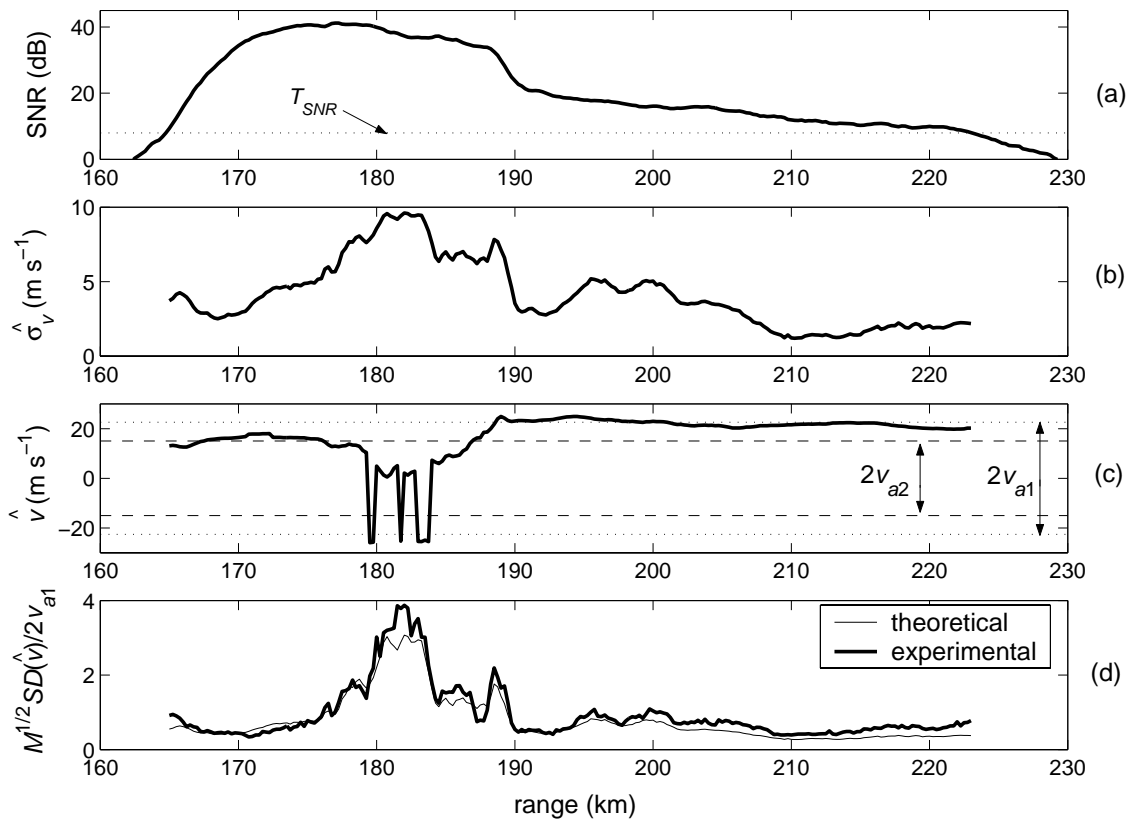


Fig. 4.2.1. Statistical performance of the velocity dealiasing algorithm on 200 radials of staggered PRT data collected with a stationary antenna.  $T_1 = 1.6 \text{ ms}$ ,  $T_2 = 2.4 \text{ ms}$  ( $\kappa = 2/3$ ),  $M = 32$ , and  $T_{SNR} = 8 \text{ dB}$ . (a) Mean signal-to-noise ratio (SNR), (b) mean spectrum width, (c) mean Doppler velocity dealiased with the velocity dealiasing algorithm (dotted and dashed lines indicate the Nyquist intervals corresponding to  $T_1$  and  $T_2$ , respectively), and (d) experimental and theoretical normalized standard deviations of velocity estimates.

The plot shows remarkable agreement between the two curves although the theoretical values are slightly smaller within regions of weaker SNRs; this is likely due to excess noise unaccounted for in the calibration. As expected, large errors of velocity estimates correspond to areas where the spectrum width is large.

### **4.3. The generalized staggered PRT velocity dealiasing algorithm**

In a recent paper (Torres et al. 2004) we described the design, real-time implementation, and demonstration of the staggered PRT sampling and processing on the KOUN radar. Unlike many of the algorithms described in the literature (Sirmans et al. 1976, Doviak et al. 1976, Doviak et al. 1978, Zrnić and Mahapatra 1985, Doviak and Zrnić 1993, Loew and Walther 1995), our velocity dealiasing algorithm extends  $v_a$  to its theoretical maximum and is valid for any PRT ratio  $\kappa$ . This has more than academic interest because the currently available PRTs on the WSR-88D network form none of the specific ratios for which the algorithms had been previously derived. At the core of the staggered PRT technique is the Doppler velocity dealiasing algorithm, which efficiently uses the fact that Doppler velocities obtained from the short and long PRTs alias in different Nyquist intervals. The design of this algorithm stems from a precise study of the velocity difference transfer function that avoids misconceptions found in previous works. Details of this analysis can be found in appendices D and E. For any staggered PRT ratio of the form  $\kappa = m/n$  with  $m$  and  $n$  relatively prime integers, the properties of this function lead to a general velocity dealiasing algorithm that extends the maximum unambiguous velocity to its theoretical maximum ( $v_a = mv_{a1} = nv_{a2}$ ). As a result, the maximum unambiguous range and velocity product  $r_a v_a$  is  $m$  times larger than what is possible with uniform PRT, improving the ability of weather surveillance radars to observe widespread severe phenomena.

#### 4.4. Effectiveness of phase coding and staggered PRT

Application of phase coding or staggered PRT increases the area wherein velocities can be recovered compared to clear area offered by uniform PRT. Here we compute the percent of area where censoring is applied for the two mitigating techniques. These computations are done on the data collected in 2003 and 2004 (see Table).

The percent of area where velocities can not be recovered is found from the ratio of censored area to the total area (Fig. 4.4.1):

$$\text{Percent of Obscuration} = A_c / (A_c + A_v),$$

where  $A_c$  is the area where censoring is applied (purple in Fig. 4.4.1.a and Fig. 4.4.1.b), and  $A_v$  is the area of valid echoes (shades of green and red in Fig. 4.4.1.a same as area in Fig. 4.4.1.c).

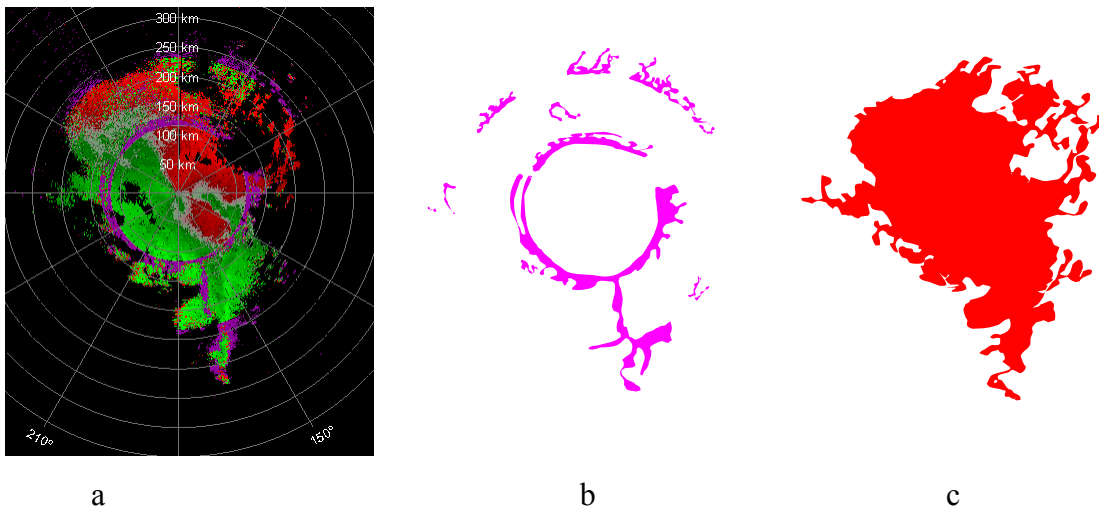


Fig. 4.4.1. (a) Velocity field, March 4, 2004, short PRT ( $r_a = 117$  km); (b) area where censoring is applied,  $A_c$ ; (c) total area (sum of censored and valid portions),  $A_c + A_v$ .

Table 4.4.1: Days of data collection

Scan No	Date
1	October 8 2002
2	October. 29 2002
3	February 14 2003
4	February 14 2003
5	February 14 2003
6	March 17 2003
7	March 17 2003
8	March 17 2003
9	April. 5 2003
10	May 16 2003
11	June 4 2003
12	June 11 2003
13	June 11 2003
14	June 13 2003
15	June 25 2003
16	March 4 2004
17	March 4 2004

The events for which this analysis was performed are listed in the Table 4.4.1 and corresponding images can be viewed on [http://cimms.ou.edu/rvamb/SZ/SZ-2\\_Algorithm.htm](http://cimms.ou.edu/rvamb/SZ/SZ-2_Algorithm.htm).

In Fig. 4.4.2, are the percentages of obscuration for the case of standard processing (exactly the same as on the WSR-88D) and for the case of phased coding. The scan in Fig. 4.4.2 refers to the scan numbers in the Table 4.1, and the comparisons are at the two lowest elevations where the phase coding is currently suggested. Immediately obvious is the decrease in obscuration by about a factor of 2 to 4 for the phase coded cases. The relative position of graphs within the same case (i.e., phase coded) depends on the particularity of the echoes. For instance in case number 10, the medium PRT produces a larger obscured area (in the non-phase-coded case as well as in the phase-coded case) than the short-PRT case which is counterintuitive. This is entirely due to the position of storms (Fig. 4.4.3). Note how the ground clutter from first trip overlays the storms in the second trip at the medium PRT, whereas the overlay is less significant at the short PRT.

Moreover, although the total area at the medium PRT is larger (to the north of the radar) than the total area at the short PRT, the increased patch is mainly obscured. Therefore, the percent of area at the medium PRT is smaller. This amply illustrates the importance to have variable PRT for mitigating range and velocity ambiguities.

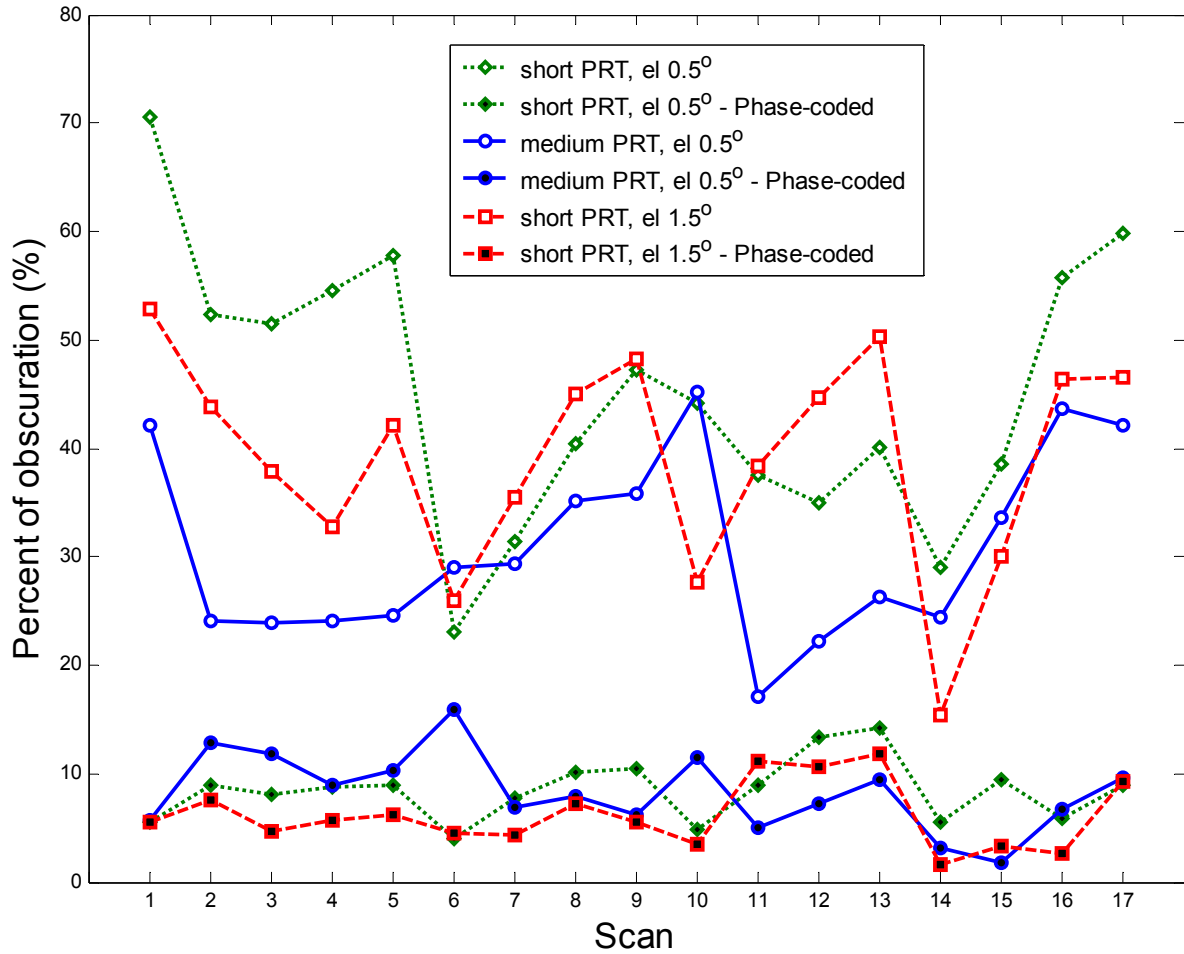


Fig. 4.4.2. Percent of obscuration for the events listed in the Table 4.4.1 whereby both legacy WSR-88D processing and the SZ-2 phase coding algorithm were applied.

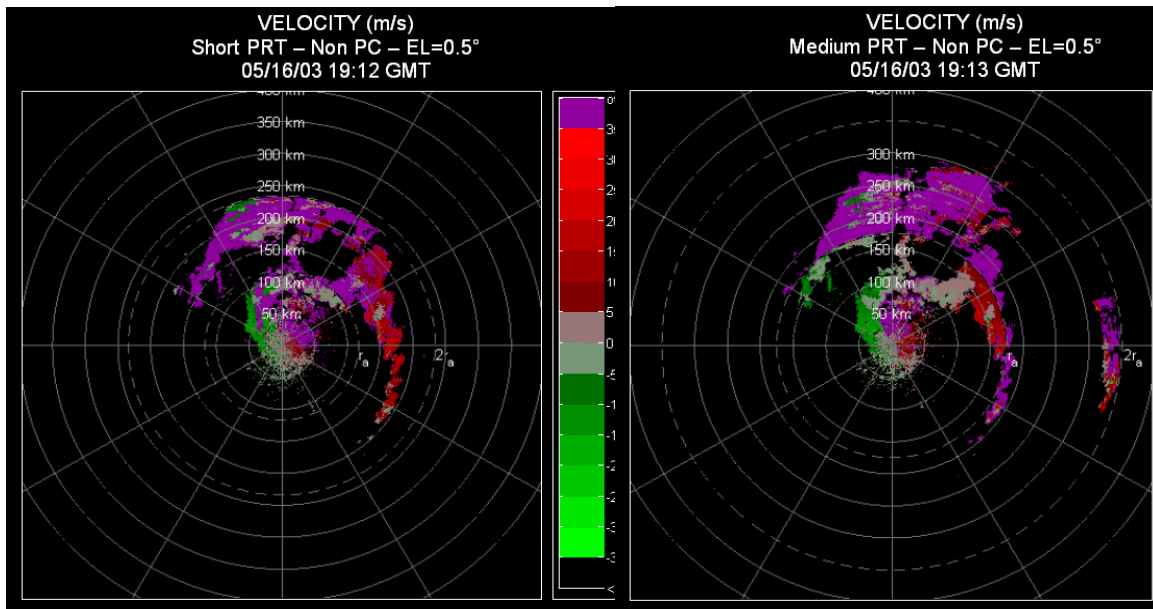


Fig. 4.4.3. Velocity fields obtained with a short ( $r_a = 117$  km) and medium PRT ( $r_a = 175$  km). Time between scans is one minute.

The percent of obscuration in phase coded cases varies from few percentage points to over 10%. Most of the obscuration is due to the strong ground clutter overlaying the second trip weak echo. The fraction of the total area (up to 234 km in range) in which ground clutter of the KOUN radar would preclude velocity measurement with SZ-2 phase coding of short PRTs is about 6 %.

Effectiveness of staggered PRT and comparison with uniform PRT has been analyzed in a similar manner. We collected data with two types of VCPs. One (VCP-46a, see Torres et al. 2003) consisted of a surveillance scan, Doppler scan ( $r_a = 117$  km), and a short staggered PRT scan. The other (VCP-46b) had a surveillance scan, a Doppler scan ( $r_a = 148$  km), a long staggered PRT, a short staggered PRT, and a medium staggered PRT.

First, we analyze data from the VCP-46a. The percentages of obscured areas were computed up to a range of 234 km which is twice the unambiguous range of the Doppler scan. Note that the

range for Doppler measurement in the staggered scheme is 184 km and the range for reflectivity is 276 km. Thus, in principle, the range for Doppler measurement in this staggered scheme could be increased beyond 184 km by appropriate processing of second trip echoes; this we have not done. Nonetheless, we have elected to consider storms up to 234 km in range for computations of the obscuration because that is how far the velocities are provided in the uniform PRT (Doppler) scan. Results are presented in Fig. 4.4.4 where the event number refers to the date (month and day); images of reflectivity and velocity fields for these days are available on the website [http://cimms.ou.edu/rvamb/Staggered/Stag\\_Algorithm.htm](http://cimms.ou.edu/rvamb/Staggered/Stag_Algorithm.htm). Obvious is the improvement with the staggered PRT at the elevation angles 1.5 and 2.5 deg. In fact, at elevations of 2.5 deg apart from the 5/16 case there are hardly any obscured areas.

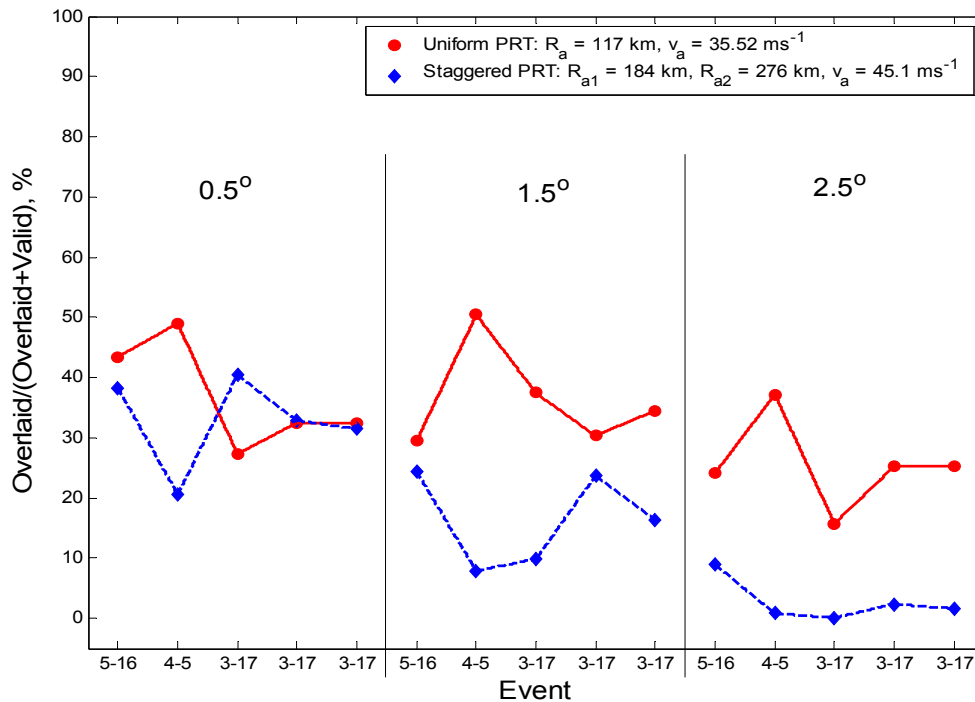


Fig. 4.4.4. Percent of obscuration for some of the events listed in the Table 4.1; the events are listed by date and results for three elevation angles are plotted. Uniform PRT (parameters are listed) data are processed exactly as on the WSR-88D. Short staggered PRT is used with the listed parameters.

In one case on 3/17 (Fig. 4.4.4 middle of the graph at 0.5 deg) the uniform PRT exhibits smaller obscuration than the staggered PRT. This is because most cell are situated in the second trip of the Doppler scan; hence, there is little overlay in the first trip (Fig. 4.4.5, also see images on the website). Nonetheless, the storms extend beyond the range to which we have processed the data ( $r_{a1} = 184$  km) at this staggered PRT; processing to longer range would increase area with valid velocities so that it could exceed the clear area obtained with the short uniform PRT. This we had no time to verify. Also, staggered PRT with larger  $R_{a1}$  could reduce the obscuration, for that reason we collected data with three different sets ( $r_{a1}$ ) of staggered PRT later in the season. Finally, observe that the short staggered PRT is applied at the lowest elevation; we submit that a study is required to determine effectiveness of any staggered PRT at the lowest elevations.

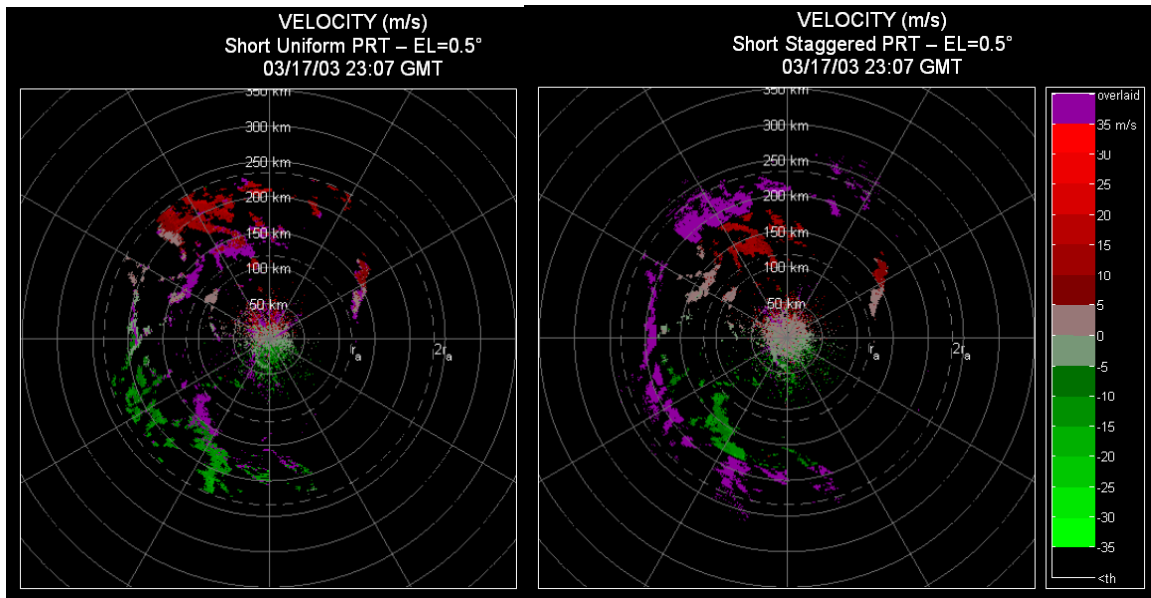


Fig. 4.4.5. Velocity fields obtains with a uniform PRT ( $r_a = 117$  km, on the left) and short staggered PRT ( $r_{a1} = 184$  km,  $r_{a2} = 276$  km, on the right)

Next we analyze the results from VCP-46b which are displayed in Fig. 4.4.6. For the Doppler scan (red dots) and the short staggered PRT (pink triangles) scan the range to which the computations of obscuration are made is 276 km (this is the range for reflectivity measurement in the short staggered PRT); hence comparison of these two graphs is “fair”. Clearly the staggered PRT recovers significantly larger area, and at 2.5 deg is free of overlaid echoes on all four days (images are on the website).

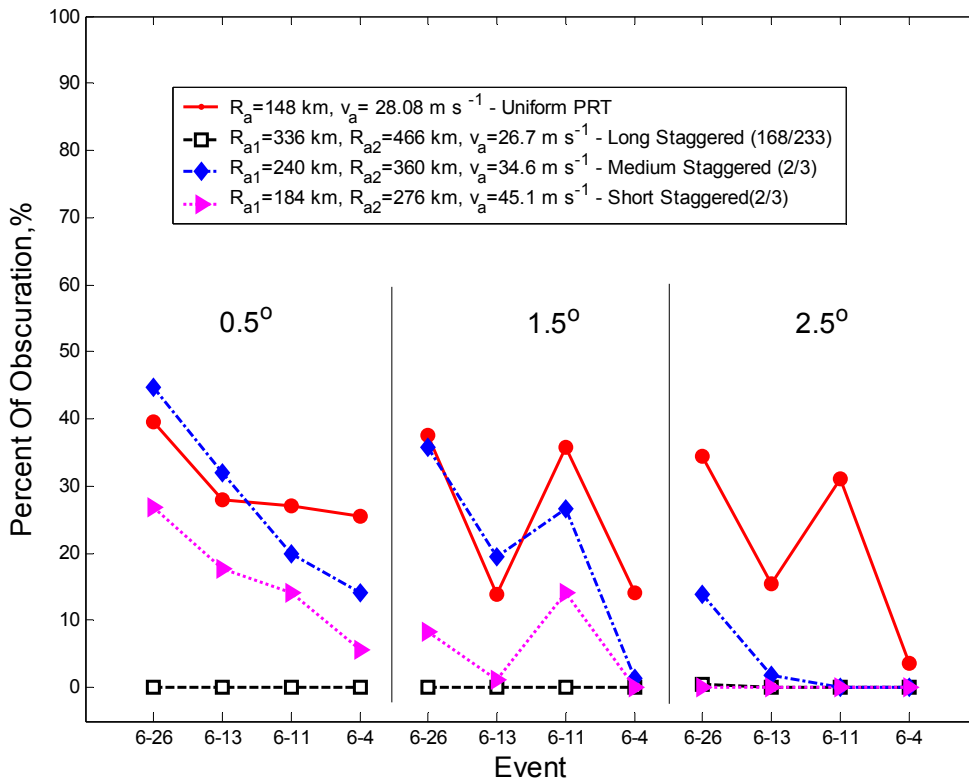


Fig. 4.4.6. Percent of obscuration for some of the events listed in the Table 4.4.1; the events are listed by date and results for three elevation angles are plotted.

Computations of the obscuration at the medium staggered PRT and the long staggered PRT were made to 296 km. This range is beyond  $r_{a1}$  of the medium staggered PRT but within the  $r_{a1}$  range of the long staggered PRT; it is exactly equal to  $2r_a$  of the uniform PRT (but was not used in the graphs for the uniform PRT!). Clearly there are no overlaid echoes in the long PRT staggered case. In the medium PRT staggered case and at 2.5 deg the overlay (up to range of 296 km) is relatively minor. Note that the obscured percent in the case of short PRT appears smaller, but that is because the computations are done only to 276 km.

Our data (on the website) and analysis indicate that staggered PRT will produce fields of velocities free of range overlaid echoes at 2.5 deg in elevation. At lower elevations the staggered PRT significantly reduces the obscured area, and often eliminates it altogether. Quantitative comparison of ground clutter filters on time series data from staggered sequences and uniform sequences should be made to establish the relative merits of these two schemes.

## 5. References

- Siggia, A. D., and R. E. Passarelli, Jr., 2004: Gaussian model adaptive processing (GMAP) for improved ground clutter cancelation and moment calculation. Preprints, 3<sup>rd</sup> *European Conf. on Radar Meteorology and Hydrology*, Visby, Sweden, MS-NR: ERAD3-P-00117.
- Bagchi, S., and S. Mitra, 1999: *The nonuniform discrete Fourier transform and its applications in signal processing*. Kluwer Academic Publishers, 208 pp.
- Ice, R. L., D. A. Warde, D. Sirmans, and D. Rachel, 2004: Open RDA – RVP8 Signal Processing. Part 1: Simulation Study, WSR-88D Radar Operations Center Report, 87 pp.
- Zrnic, D., S. Torres, Y. Dubel, J. Keeler, J. Hubbert, M. Dixon, G. Meymaris, and S. Ellis, 2003: NEXRAD range-velocity ambiguity mitigation. SZ(8/64) phase coding algorithm recommendations. NCAR-NSSL Interim Report.
- Fang, M., R.J. Doviak, and V. Melnikov, 2004: Spectrum width measured by WSR-88D: Error sources and statistics of various weather phenomena. *J. Atmos. Oceanic Technol.*, **21**, 888-904.
- Sachidananda, M., D. Zrnic, R. Doviak, and S. Torres, 1998: Signal design and processing techniques for WSR-88D ambiguity resolution, Part 2, NOAA/NSSL Report, 105 pp.
- Zrnic, D, S. Torres, Y. Dubel, J. Keeler, J. Hubbert, M. Dixon, G. Meymaris, and S. Ellis, 2003: FY2003 NCAR-NSSL interim report: NEXRAD range-velocity ambiguity mitigation – SZ(8/64) phase coding algorithm recommendations.
- Doviak, R. J. and D. S. Zrnic, 1993: *Doppler radar and weather observations*. Academic Press, New York, 562p.
- Sachidananda, M., D. Zrnic, and R. Doviak, 1999: Signal design and processing techniques for WSR-88D ambiguity resolution, Part 3, NOAA/NSSL Report, 81 pp.
- Sachidananda, M., D. Zrnic, and R. Doviak, 2000: Signal design and processing techniques for WSR-88D ambiguity resolution, Part 4, NOAA/NSSL Report, 99 pp.
- Sachidananda, M., D. Zrnic, and R. Doviak, 2001: Signal design and processing techniques for WSR-88D ambiguity resolution, Part 5, NOAA/NSSL Report, 75 pp.
- Sachidananda, M., D. Zrnic, and R. Doviak, 2002: Signal design and processing techniques for WSR-88D ambiguity resolution, Part 6, NOAA/NSSL Report, 57 pp.
- Torres, S., D. Zrnic, and Y. Dubel, 2003: Signal design and processing techniques for WSR-88D ambiguity resolution, Part 7, NOAA/NSSL Report, 103 pp.

- Doviak, R. J., D. Sirmans, and D. Zrnić, 1976: Resolution of pulse-Doppler radar range and velocity ambiguities in severe storms. Preprints *17th Conf. on Radar Meteorology*, Seattle, WA, Amer. Meteor. Soc., 15-22.
- Doviak, R. J., D. Sirmans, D. Zrnić, and G. B. Walker, 1978: Considerations for pulse-Doppler radar observations of severe thunderstorms. *J. Appl. Meteor.*, **17**, 189–205.
- Loew, E., and C. A. Walther, 1995: Engineering analysis of dual pulse interval radar data obtained by the ELDORA radar. Preprints *27th Conf. on Radar Meteorology*, Vail, CO, Amer. Meteor. Soc., 710-712.
- Sirmans, D., D. Zrnić, and B. Bumgarner, 1976: Extension of maximum unambiguous Doppler velocity by use of two sampling rates. Preprints *17th Conf. on Radar Meteorology*, Seattle, WA, Amer. Meteor. Soc., 23-28.
- Torres, S. M., Y. Dubel, and D. S. Zrnić, 2004: Design, implementation, and demonstration of a staggered PRT algorithm for the WSR-88D. *J. Atmos. Oceanic Technol.*, **21**, 1389-1399.
- Zrnić, D., and P. Mahapatra, 1985: Two methods of ambiguity resolution in pulse Doppler weather radars. *IEEE Trans. Aerosp. Electron. Syst.*, **21**, 470-483.

**LIST OF NSSL REPORTS FOCUSED ON POSSIBLE UPGRADES  
TO THE WSR-88D RADARS**

Melnikov, V. M, and D.S. Zrnice, 2004: Simultaneous transmission mode for the polarimetric WSR-88D – statistical biases and standard deviations of polarimetric variables. NOAA/NSSL Report, 84 pp.

Bachman, S., 2004: Analysis of Doppler spectra obtained with WSR-88D radar from non-stormy environment. NOAA/NSSL Report, 86 pp.

Torres S., D. Zrnice, and Y. Dubel, 2003: Signal Design and Processing Techniques for WSR-88D Ambiguity Resolution: Phase coding and staggered PRT, implementation, data collection, and processing. NOAA/NSSL Report, Part 7, 128 pp.

Schuur, T., P. Heinselman, and K. Scharfenberg, 2003: Overview of the Joint Polarization Experiment (JPOLE), NOAA/NSSL Report, 38 pp.

Ryzhkov, A, 2003: Rainfall Measurements with the Polarimetric WSR-88D Radar, NOAA/NSSL Report, 99 pp.

Schuur, T., A. Ryzhkov, and P. Heinselman, 2003: Observations and Classification of echoes with the Polarimetric WSR-88D radar, NOAA/NSSL Report, 45 pp.

Melnikov, V. M, D. S. Zrnice, R. J. Doviak, and J. K. Carter, 2003: Calibration and Performance Analysis of NSSL's Polarimetric WSR-88D, NOAA/NSSL Report, 77 pp.

NCAR-NSSL Interim Report, 2003: NEXRAD Range-Velocity Ambiguity Mitigation SZ(8/64) Phase Coding Algorithm Recommendations.

Sachidananda, M., 2002: Signal Design and Processing Techniques for WSR-88D Ambiguity Resolution, NOAA/NSSL Report, Part 6, 57 pp.

Doviak, R. J., J. Carter, V. Melnikov, and D.S. Zrnice, 2002: Modifications to the Research WSR-88D to obtain Polarimetric Data, NOAA/NSSL Report, 49 pp.

Fang, M., and R. J. Doviak, 2001: Spectrum width statistics of various weather phenomena, NOAA/NSSL Report, 62 pp.

Sachidananda, M., 2001: Signal Design and Processing Techniques for WSR-88D Ambiguity Resolution, NOAA/NSSL Report, Part 5, 75 pp.

Sachidananda, M., 2000: Signal Design and Processing Techniques for WSR-88D Ambiguity Resolution, NOAA/NSSL Report, Part 4, 99 pp.

Sachidananda, M., 1999: Signal Design and Processing Techniques for WSR-88D Ambiguity Resolution, NOAA/NSSL Report, Part 3, 81 pp.

Sachidananda, M., 1998: Signal Design and Processing Techniques for WSR-88D Ambiguity Resolution, NOAA/NSSL Report, Part 2, 105 pp.

Torres, S., 1998: Ground Clutter Canceling with a Regression Filter, NOAA/NSSL Report, 37 pp.

Doviak, R. J. and D. S. Zrnic, 1998: WSR-88D Radar for Research and Enhancement of Operations: Polarimetric Upgrades to Improve Rainfall Measurements, NOAA/NSSL Report, 110 pp.

Sachidananda, M., 1997: Signal Design and Processing Techniques for WSR-88D Ambiguity Resolution, NOAA/NSSL Report, Part 1, 100 pp.

Sirmans, D., D. S. Zrnic, and M. Sachidananda, 1986: Doppler radar dual polarization considerations for NEXRAD, NOAA/NSSL Report, Part I, 109 pp.

Sirmans, D., D. S. Zrnic, and N. Balakrishnan, 1986: Doppler radar dual polarization considerations for NEXRAD, NOAA/NSSL Report, Part II, 70 pp.

## Appendix A. Engineering Development and Data Collection for FY04

Configuration of the radar as existed during 2004 and up to this writing is depicted in Fig. A.1. The system contains three main components, the Legacy, the Research Radar Data Acquisition (RRDA), and Sigmet's RVP8.

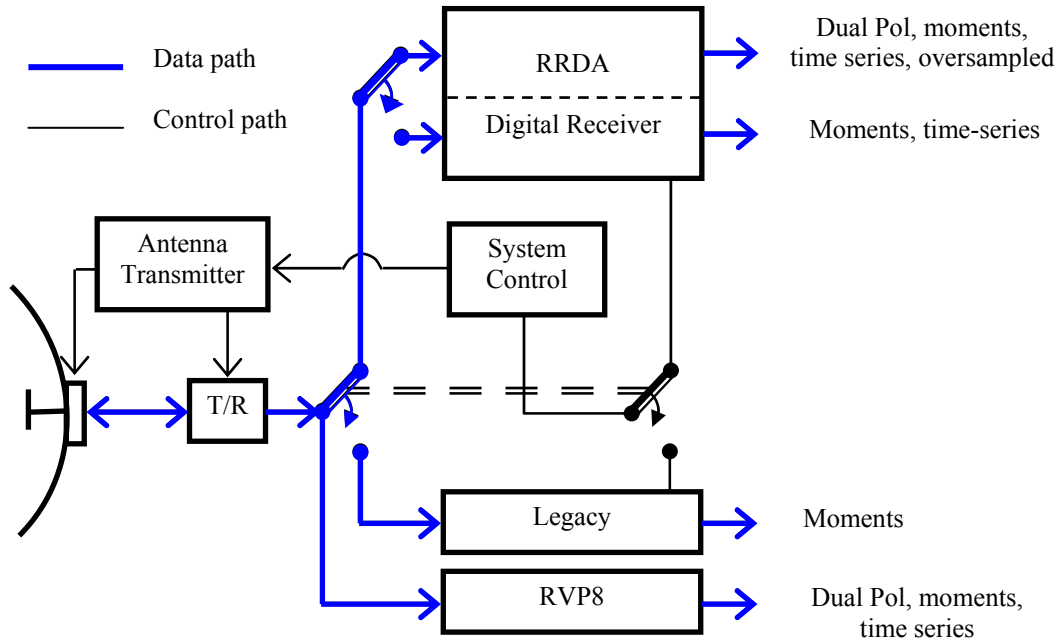


Fig. A.1. Control and data paths on the research and development KOUN radar.

The Sigmet's RVP8 is connected in a passive mode and accepts the data while either the RRDA or the Legacy control the radar. Therefore, only uniform PRT data can be processed by the RVP8. Generation of dual polarization variables and recording of these variables as well as time series data is possible through the RVP8.

The Legacy system is as on the network of the WSR-88D radars, and it is continuously updated by the National Weather Service. It provides spectral moments which, as on all WSR-88Ds, can be recorded. It serves mainly for diagnostic purposes and for comparisons with the RRDA.

The RRDA enabled us to generate staggered and phase coded sequences. The RRDA accommodates two different receivers. One is the analogue (Legacy) receiver through which only horizontally polarized signals pass. The other is the digital receiver on which significant engineering developments were made; it was configured to provide oversampled I, Q components. The oversampling factor can be set to 1 (no oversampling), 5 (in regular and dual-polarization mode), and 10 (in non-dual-polarization mode). Thus, oversampled or regularly sampled time series data in either dual polarization or single polarization can be collected. At the moment, there is no processing of dual polarization data in real time on the RRDA but spectral moments in the H channel are computed.

During the spring of 2004 it was not possible to oversample and record staggered PRT data. At various times we realized that not all PRTs were functional in the oversampled mode. Thus, some of the oversampled data that we list herein might be faulty. For R/V purposes, the non oversampled data suffice. In summer of 2004 we have purchased a dual raceway interlink which enabled collection of oversampled times series in all PRTs as well as in staggered PRT and dual polarization. The first data collection in 2004 was made on Feb 23.

Herein we briefly describe the storm type and distribution for each pertinent day and tabulate the VCP and type of data collected. The two digit VCP designation i.e., XX refers to the description in our report from 2003 (Torres et al. 2003). Since then, some new VCPs have been programmed

and the designation has changed so that the new VCPs are numbered with four digits, XXXX. The pertinent new VCPs are 2048, 2049, and 2011; these are listed in tables.

### **A.1. Tables of VCPs**

Tables of the new VCPs which were used extensively during the Spring of 2004 follow. The 2048 (Table A.1) contains legacy continuous and Doppler scans followed by a phase coded scan and a staggered PRT scan at the lowest elevation of  $0.48^\circ$ ; the same repeats at  $1.45^\circ$ . These low elevations are most prone to overlaid echoes and we wanted to have closely spaced scans each employing a different technique for comparisons. At  $2.45^\circ$  the first scan has batch mode, then follows a scan with phase coded signals and the last scan uses staggered PRT. The phase coded signals have the SZ(8/64) code.

The 2049 VCP (Table A.2) has no staggered PRT, and has four Doppler scans at each elevation, a pair with PRT No. 8, one scan without the other with phase coding, and a pair at PRT No. 5 also without and with phase coding. Omission of staggered PRT was made so that we could collect oversampled data which at the time could not be done in the staggered PRT mode.

The 2011 VCP (Table A.3) follows the recommendation by Sachidananda et al. (2001). Note that in the staggered PRT the unambiguous ranges (for both reflectivity and velocity) first decrease with elevation (at angles  $2.3^\circ$  to  $4.3^\circ$ ), then there is an abrupt change (i.e., increase) and again gradual decrease until constant values at  $8.7^\circ$  are reached. The reason for this is that at the lowest elevations the recommendation was to resolve once overlaid echoes; this resolution is at best tenuous and the PRTs were chosen so that the errors of estimates could be controlled. At higher elevations there would be no overlaid echoes. It might be worthwhile not to attempt a once overlay resolution, but censor the overlaid data, in which case a gradual monotonous decrease of

unambiguous ranges with elevation could be a good choice. This will be explored in subsequent studies.

A short description of various acronyms in Table A.1 follows. CS – is continuous scan (uniform PRT). CD – is continuous Doppler (uniform PRT). PC - is phase coded [uniform PRT, SZ(8/64)]. ST - is staggered PRT, and the stagger ratio is within parenthesis. B – signifies batch mode. The numbers next to these designations refer to the PRTs; these are internal to our housekeeping. In the case of staggered PRT,  $M$  is the number of staggered pairs, and  $T_1$  and  $T_2$  refer to the short and long PRT. For the batch mode  $T_1$  is the PRT for reflectivity estimation and  $T_2$  is the one for velocity estimation. The maximum ranges to which measurements can be made are to be interpreted as follows.  $r_{ar}$  is the range for reflectivity measurement, and  $r_{av}$  is the range to which Doppler measurements are made, in the case of phase coded signals this range is twice the one of the non coded signals. (Note that sometime velocities can be recovered to larger range, i.e., third or even forth trip in the case of phase coding.). In the case of staggered PRT,  $r_{ar}$  corresponds to the long PRT,  $T_2$ , and  $r_{av}$  corresponds to  $T_1$ , further the  $v_a$  corresponds to the extended unambiguous velocity.

Elev. (deg)	AZ rate (deg/s)	Period (s)	Dwell time (ms)	WF type	PRT #	Short PRT #	Long PRT #	M	$T_u$ (ms)	$T_1$ (ms)	$T_2$ (ms)	$r_{ar}$ (km)	$r_{av}$ (km)	$v_a$ (m/s)
0.48	18.66	19.29	52.87	CS,1	1	-	-	17	3.11	-	-	466	-	-
0.48	19.23	18.72	51.3	CD,5	5	-	-	52	0.98	-	-	-	148	28.8
0.48	20.03	17.97	49.92	PC,8	8	-	-	64	0.78	-	-	-	234	35.52
0.48	17.86	20.15	56	ST(2/3)	-	23	24	14	-	1.6	2.4	360	240	34.64
1.45	19.84	18.14	49.76	CS,1	1	-	-	16	3.11	-	-	466	-	-
1.45	19.23	18.72	51.3	CD,5	5	-	-	52	0.98	-	-	-	148	28.8
1.45	20.03	17.97	49.92	PC,8	8	-	-	64	0.78	-	-	-	234	35.52
1.45	17.86	20.15	56	ST(2/3)	-	23	24	14	-	1.6	2.4	360	240	34.64
2.45	16.12	22.34	29.44	B,1,5	-	5	1	6,41	-	3.11	0.98	466	148	28.8
2.45	20.03	17.97	49.92	PC,8	8	-	-	64	0.78	-	-	-	234	35.52
2.45	16.30	22.08	61.4	ST(2/3)	-	9	10	20	-	1.23	1.84	276	184	45.1

Table A.1. VCP 2048

Elev. (deg)	AZ rate (deg/s)	Period (s)	Dwell time (ms)	WF type	PRT #	Short PRT #	Long PRT #	M	$T_u$ (ms)	$T_1$ (ms)	$T_2$ (ms)	$r_{ar}$ (km)	$r_{av}$ (km)	$v_a$ (m/s)
0.48	18.93	19.03	52.87	CS,1	1	-	-	17	3.11	-	-	466	-	-
0.48	15.84	22.73	62.72	CD,5	5	-	-	64	0.98	-	-	-	148	28.8
0.48	15.84	22.73	62.72	PC,5	5	-	-	64	0.98	-	-	-	296	28.8
0.48	20.03	17.97	49.92	CD,8	8	-	-	64	0.78	-	-	-	117	35.52
0.48	20.03	17.97	49.92	PC,8	8	-	-	64	0.78	-	-	-	234	35.52
1.49	20.11	17.9	49.76	CS,1	1	-	-	16	3.11	-	-	466	-	-
1.49	15.84	22.73	62.72	CD,5	5	-	-	64	0.98	-	-	-	148	28.8
1.49	15.84	22.73	62.72	PC,5	5	-	-	64	0.98	-	-	-	296	28.8
1.49	20.03	17.97	49.92	CD,8	8	-	-	64	0.78	-	-	-	117	35.52
1.49	20.03	17.97	49.92	PC,8	8	-	-	64	0.78	-	-	-	234	35.52

Table A.2. VCP 2049

Elev. (deg)	AZ rate (deg/s)	Period (s)	Dwell time (ms)	WF type	PRT #	Short PRT #	Long PRT #	M	T <sub>it</sub> (ms)	T <sub>1</sub> (ms)	T <sub>2</sub> (ms)	r <sub>ar</sub> (km)	r <sub>av</sub> (km)	v <sub>a</sub> (m/s)
0.48	18.89	19.06	52.87	CS,1	1	-	-	17	3.11	-	-	466	-	-
0.48	20.00	18.00	49.92	PC,8	8	-	-	64	0.78	-	-	-	234	35.52
1.45	20.10	17.91	49.76	CS,1	1	-	-	16	3.11	-	-	466	-	-
1.45	20.00	18.00	49.92	PC,8	8	-	-	64	0.78	-	-	-	234	35.52
2.42	17.20	20.93	58.33	ST(2/3)	-	9	10	19	-	1.23	1.84	276	184	45.1
3.34	19.00	18.95	52.57	ST(2/3)	-	11	12	19	-	1.11	1.66	249	166	50.07
4.3	19.80	18.18	50.6	ST(2/3)	-	13	14	22	-	0.92	1.38	207	138	60.4
5.2	18.70	19.25	53.4	ST(2/3)	-	15	16	18	-	1.19	1.78	267	178	46.7
6.2	18.6	19.35	53.9	ST(2/3)	-	17	18	21	-	1.03	1.54	231	154	53.98
7.5	26.70	13.48	37.4	ST(2/3)	-	19	20	17	-	0.88	1.32	198	132	62.98
8.7	27.7	13.00	36.1	ST(2/3)	-	21	22	19	-	0.76	1.14	114	171	72.92
10	27.7	13.00	36.1	ST(2/3)	-	21	22	19	-	0.76	1.14	114	171	72.92
12	27.7	13.00	36.1	ST(2/3)	-	21	22	19	-	0.76	1.14	114	171	72.92
14	27.7	13.00	36.1	ST(2/3)	-	21	22	19	-	0.76	1.14	114	171	72.92
16.7	27.7	13.00	36.1	ST(2/3)	-	21	22	19	-	0.76	1.14	114	171	72.92
19.5	27.7	13.00	36.1	ST(2/3)	-	21	22	19	-	0.76	1.14	114	171	72.92

Table A.3. VCP 2011

## A.2. Summary of collected data

The summary by day of collected data is listed next.

### Feb 23

On this day, a large stratiform precipitation was located south east from the radar, and few small cells were to the northwest. The H and V channels on this day were interchanged because the collar tube in the pedestal was inadvertently rotated by 180° in the Fall of 2003. The collar was mounded correctly on March 15, 2004. In the dual polarization mode there may be a shift of up to one range gate between H and V samples. This was fixed on March 17.

VCP	Time (UTC)	Polarization	Oversampled	Receiver
2048		H	Yes	Digital
43		dual H,V	Yes	Digital
43		dual H,V	No	Digital

### March 3

Widespread, low-intensity cells were located in the radar coverage area. The following table summarizes pertinent data collection parameters.

VCP	Time (UTC)	Polarization	Oversampled	Receiver
2049		dual	yes	Digital
RV-111		no	no	Analogue
11		no	no	Analogue
2048		no	no	Analogue
2049		no	no	Analogue
2048		dual	no	Digital
2049		dual	no	Digital
2048		no	yes	Digital
2049		no	yes	Digital

## March 4

Data collection started at about 1:30 pm. A squall line and large MCS were moving from the south. There was a warning for high winds and we were advised to vacate the premises. Nevertheless, on the radar screen we noticed that the line had broken and Doppler winds were weakening, so we continued to collect the data.

VCP	Time (UTC)	Polarization	Oversampled	Receiver	Comments
ROC-11		H	no	Analogue	for ROC
2011		H	no	Analogue	
11		H	no	Analogue	
2048		H	no	Analogue	
2049		H	no	Analogue	
2049		dual	yes	Digital	
2048		dual	no	Digital	
2049		dual	no	Digital	
2048		dual	no	Digital	
2048		H	yes	Digital	
2049		H	yes	Digital	
2048		H	no	Analogue	
2049		H	no	Analogue	
2049		dual	no?	Digital	
11		H	no	Analogue	3 hours

## April 21

Several individual intense storms were in Central Oklahoma. We have collected mostly uniformly-spaced time series data at the lowest few elevations. These uniform-PRT data were collected with the VCP designation HR (46, 47, 51). We do not list these herein to save space and because they are not pertinent to the R/V, but some of these were in oversampling mode. The radar was in dual polarization mode all the time and the digital receiver was used. We tabulate only the data for R/V mitigation studies.

VCP	Time (UTC)	Oversampled	Comments
2049		yes	
2048		yes	
2011		no	
2049		yes	3 consecutive VCPs
2048		yes	
2011		no	
2048		yes	
2049		yes	

### April 22

On this day there were birds, some very small storm cells close to the radar, and large storm far away. Patchy cells to the northeast and east looked like AP but we think these are cells. Radar was in dual polarization mode all the time with no oversampling.

VCP	Time (UTC)	Comments
2048		
2049		
44		No of samples 128, data at r<40 km mostly OK

### April 23

Much precipitation and a long squall line occurred on this day. Only a couple of R/V scans were made both in dual polarization and without oversampling. These are listed.

VCP	Time (UTC)	Comments
2011	21:58	Hail storm near Duncan (Phase coded + staggered top)
2048	> 23:15	400 km+, squall line south west and over radar

## April 29

We have collected some data in clear air (from insects, birds). The only two scans for R/V mitigation are listed.

VCP	Time (UTC)	Comments
2048	~ 2	Birds to the NE, storm SW and some overlay
2011		Squall line (curved) within 20 km, MCS

## June 4

Two scans for R/V mitigation studies were collected. It seems that the air to the east cooled and therefore extended AP developed. This is the only case we have in which AP extends to the second trip. It might be the only AP in phased coded and staggered PRT.

VCP	Time (UTC)	Comments
Temp-64091	2:53	Uniform PRT (for birds), good AP
2048	~ 3:10	AP east, range overlaid at 0.4°
2049	3:25	

## June 30

One VCP (2048) was collected on this day starting at 18:25 UCT. There was a large region of stratiform precipitation east of the radar and numerous small cells everywhere else.

## Aug 12

Two VCP (2048) in dual polarization mode and oversampled by 5. Some storm cells may have overlaid echoes.

## **September 9**

VCP (2048) dual polarization, non oversampled. This was a morning with significant amount of AP over large areas. A cold front moved and cooled the lowest levels, which where then further cooled by radiation.

## **Appendix B. Estimates of Large Spectrum Width from Autocovariances**

The following is a reprint of a paper published in the June 2004 issue of the Journal of Oceanic and Atmospheric Technology by V. Melnikov and D. Zrnić.



## Appendix C. Errata for the June 1, 2004 SZ-2 Algorithm

NEXRAD Range-Velocity Ambiguity Mitigation - SZ-2 Algorithm Recommendation

### ERRATA

June 22, 2004

Page 5. Recommended values of  $C_S$  should be  $-429$  dB in both cases.

Page 7, step 2.  $r$  is an input to this step,  $n_C$  is not an output to this step.

Page 10, step 5.iv. Phase reconstruction should be performed as

$$\varphi_{CF}(k) = \begin{cases} 0, & k_{GMAP} > 0 \text{ and} \\ & [k \leq (k_{GMAP} - 1)/2 \text{ or } k \geq M - (k_{GMAP} - 1)/2] \\ \text{Arg}[F_{CW}(k)], & \text{otherwise} \end{cases}$$

Page 10, step 6. The “Else” corresponding to “If  $t_C = -1$ ” can be optimized as

*(Signal was clutter filtered; therefore, cohere from trip  $t_C$  if needed)*

If  $t_C \neq t_A$

*(Cohering is needed)*

$$V_A(m) = V_{CF}(m) \exp[-j\phi_{t_A, t_C}(m)], \text{ for } 0 \leq m < M$$

Else

*(Cohering is not needed)*

$$V_A(m) = V_{CF}(m), \text{ for } 0 \leq m < M$$

End

Page 11, step 6. The “Else” corresponding to “If  $t_C = -1$ ” can be optimized as

*(Signal was clutter filtered; therefore, cohere from trip  $t_C$  if needed)*

If  $t_C \neq t_B$

*(Cohering is needed)*

$$V_B(m) = V_{CF}(m) \exp[-j\phi_{t_B, t_C}(m)], \text{ for } 0 \leq m < M$$

Else

*(Cohering is not needed)*

$$V_B(m) = V_{CF}(m), \text{ for } 0 \leq m < M$$

End

Page 14, step 14. In the note,  $\tilde{P}_w$  should be written as  $\tilde{P}_w \approx P[r(t_w)] + P(2) + P(3) + NOISE$

Page 17, step 21.

a)  $P_L$  and  $t_C$  are inputs to this step,  $n_C$  is not an input to this step.

b) If #1 should be modified as

If  $n + IN < N_L$  and  $P_L(n + IN) > NOISE.K_{SNR}$

c) SNR\* censoring should be modified as

If  $t_W \neq -1$

If  $P[r(t_S)] < \{P[r(t_W)] + P(2) + P(3) + NOISE\}K_s$

*(Strong-trip long-PRT power is not above  $K_s$ -times the sum of the powers of the out-of-trip signals plus noise; therefore, censor)*

$CENSOR = TRUE$

End

Else

If  $P[r(t_S)] < [P(1) + P(2) + P(3) + NOISE]K_s$

*(Strong-trip long-PRT power is not above  $K_s$ -times the sum of the powers of the out-of-trip signals plus noise; therefore, censor)*

$CENSOR = TRUE$

End

End

## **Appendix D. Design, Implementation, and Demonstration of the Staggered PRT Algorithm for the WSR-88D**

The following is a reprint of a paper published in the September 2004 issue of the Journal of Oceanic and Atmospheric Technology by S. Torres, Y. Dubel, and D. Zrnić.



## Appendix E. Staggered PRT velocity dealiasing algorithm: Analysis of the velocity difference transfer function

### E.1. The Staggered PRT Technique

The staggered PRT technique is based on a transmitted pulse sequence consisting of two alternating pulse spacings,  $T_1$  and  $T_2$ , as shown on Fig. E.1. Autocorrelation estimates are computed using alternate pairs of samples for every range bin in the radial. For a given range bin,  $\hat{R}_1$  is obtained for lag  $T_1$  and  $\hat{R}_2$  for lag  $T_2$ . Then, two Doppler velocities,  $\hat{v}_1$  and  $\hat{v}_2$ , are estimated from the principal arguments (Arg) of  $\hat{R}_1$  and  $\hat{R}_2$  as

$$\hat{v}_1 = -\frac{\lambda}{4\pi T_1} \text{Arg}\{\hat{R}_1\}, \text{ and} \quad (\text{E.1})$$

$$\hat{v}_2 = -\frac{\lambda}{4\pi T_2} \text{Arg}\{\hat{R}_2\}, \quad (\text{E.2})$$

where  $\lambda$  is the radar wavelength. Thus,  $\hat{v}_1$  ( $\hat{v}_2$ ) is estimated unambiguously only if the true velocity lies within the unambiguous limits  $\pm v_{a1}$  ( $\pm v_{a2}$ ), where  $v_{a1} = \frac{\lambda}{4T_1}$  ( $v_{a2} = \frac{\lambda}{4T_2}$ ) is the Nyquist velocity for lag  $T_1$  ( $T_2$ ). Without loss of generality, the case where  $T_1 < T_2$  is considered for this study.

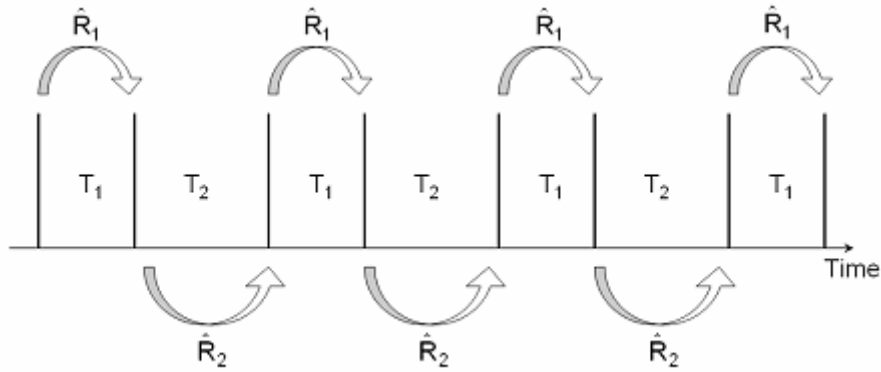


Fig. E.1. Staggered PRT Pulsing Scheme

## E.2. Extension of the unambiguous velocity

Figure E.2 shows the transfer functions of the aliased velocities  $v_1$  and  $v_2$  (assuming there are no estimation errors) with respect to the true velocity in the particular case where  $T_1/T_2 = 3/5$ . Since the true velocity  $v$  could be outside the unambiguous intervals determined by  $v_{a1}$  and  $v_{a2}$ ,  $v_1$  and  $v_2$  will in general alias in different ways. Therefore, the differences between  $v_1$  and  $v_2$  can be used to resolve the true velocity using a “Chinese Remainder Theorem”-like approach (see Fig. E.3).

As it will be shown later,  $v_1 - v_2$  is a piecewise constant function of the true velocity  $v$ . Accordingly, the goal is to find an interval (hopefully greater than the ones determined by  $v_{a1}$  and  $v_{a2}$ ) on which the constant values that  $v_1 - v_2$  takes are all different so that the proper Nyquist interval for  $v_1$  and  $v_2$  can be uniquely determined. Hence, a suitable dealiasing algorithm can be defined for that interval. That is, for a given set of aliased estimates  $\hat{v}_1$  and  $\hat{v}_2$ ,

the segment on which  $\hat{v}_1 - \hat{v}_2$  and  $v_1 - v_2$  are the closest is used to resolve the true velocity as shown in Fig. E.3.

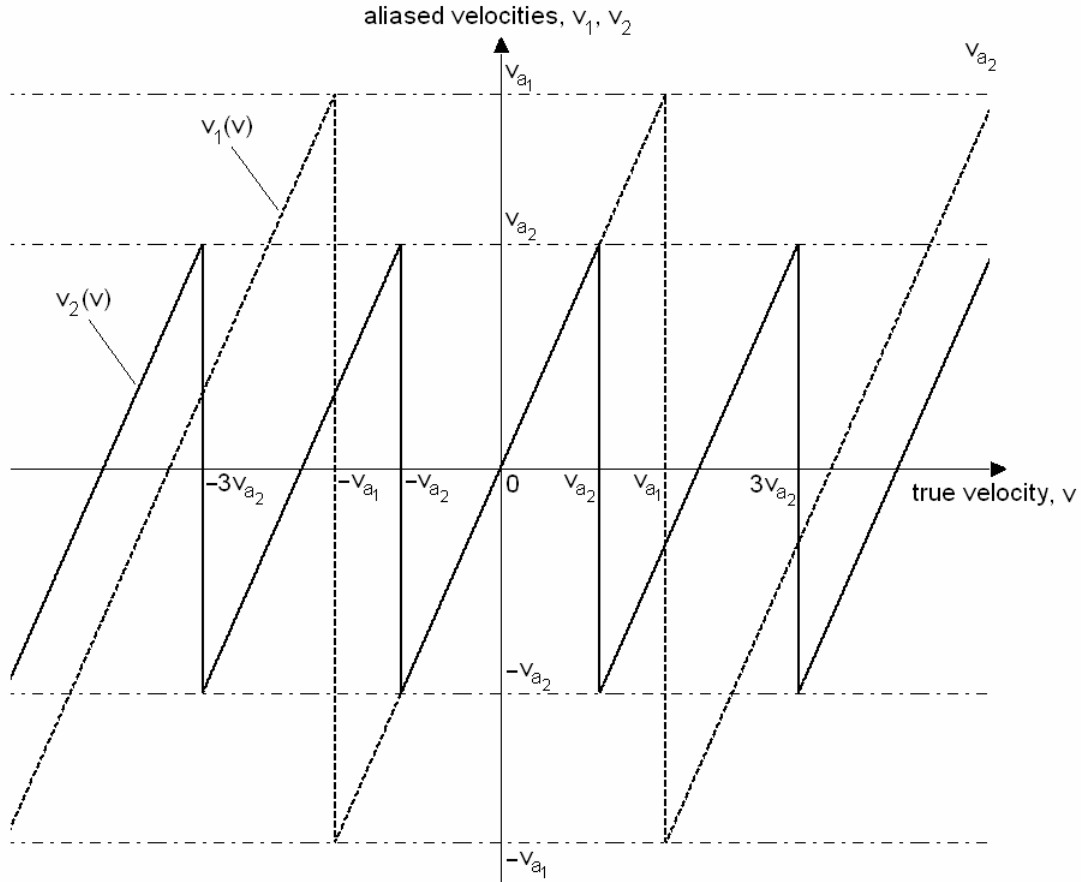


Fig. E.2. Aliased velocities versus the true velocity for  $\frac{T_1}{T_2} = \frac{3}{5}$

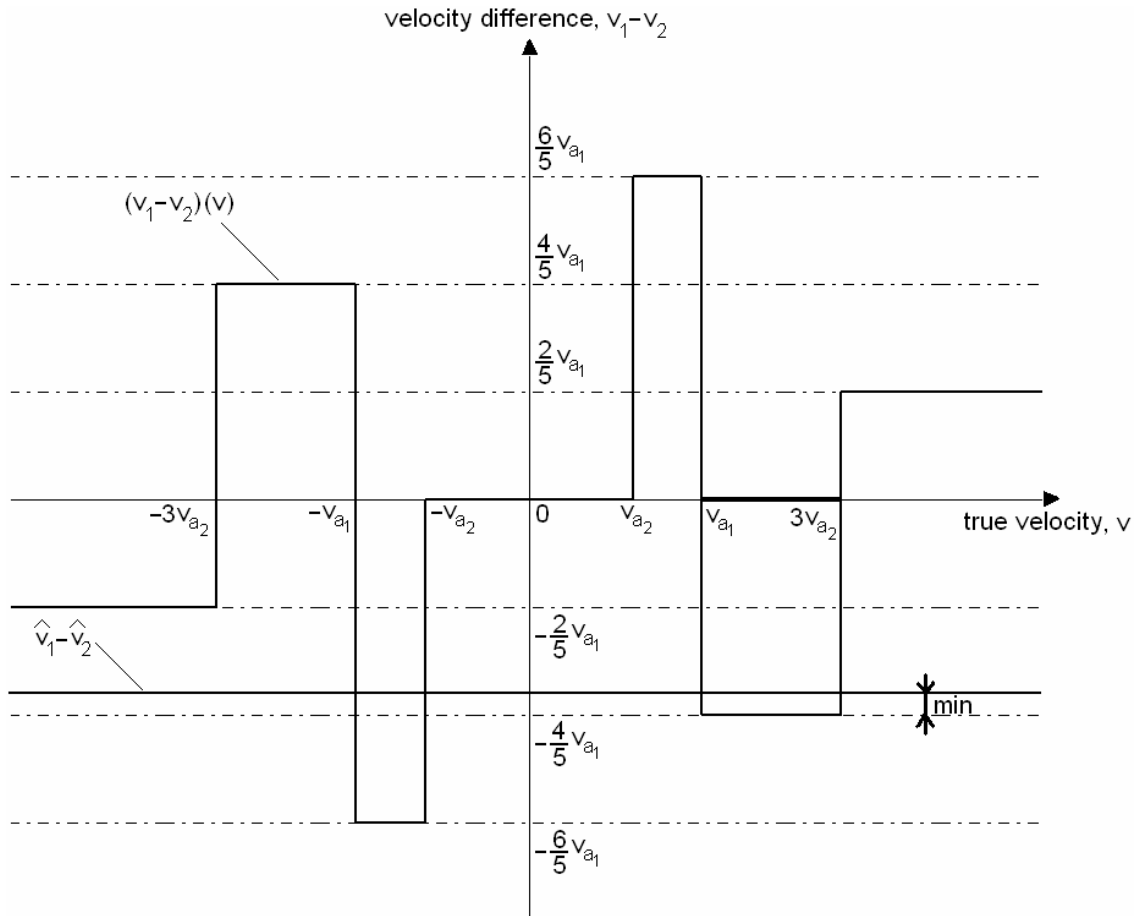


Fig. E.3. Aliased velocity difference  $v_1 - v_2$  versus the true velocity for  $T_1/T_2 = 3/5$ . Comparison between  $\hat{v}_1 - \hat{v}_2$  and  $v_1 - v_2$  for  $\hat{v}_1 - \hat{v}_2 = -7v_{a1}/10$ . The interval on which the difference between  $\hat{v}_1 - \hat{v}_2$  and  $v_1 - v_2$  is minimum is  $(v_{a1}, 3v_{a2})$ . The corresponding de-aliased  $v_{d1}$  is  $\hat{v}_1 - 2v_{a1}$  and the corresponding de-aliased  $v_{d2}$  is  $\hat{v}_2 - 2v_{a2}$ .

In view of this, the study of the expected velocity difference transfer function appears to be essential in designing the optimum velocity dealiasing algorithm in the staggered PRT technique.

### E.3. Analysis of the velocity difference transfer function

#### E.3.1. Equation of the velocity difference transfer function

Equations (E.1) and (E.2) can be rewritten as

$$v_1(v) = -\frac{v_{a1}}{\pi} \text{Arg}\{R_1(v)\}, \text{ and} \quad (\text{E.3})$$

$$v_2(v) = -\frac{v_{a2}}{\pi} \text{Arg}\{R_2(v)\}, \quad (\text{E.4})$$

where  $v$  is the true velocity,  $R_1(v) = A_1 e^{-j\pi v/v_{a1}}$  and  $R_2(v) = A_2 e^{-j\pi v/v_{a2}}$  are the expected autocorrelations ( $A_1, A_2 \in \mathbb{R}$ ). Equation (E.3) can be modified as

$$\begin{aligned} v_1(v) &= \frac{v_{a1}}{\pi} \left( \left[ -\text{Arg}\{R_1(v)\} + \pi \right] - \pi \right) \\ &= 2v_{a1} \left[ \frac{-\text{Arg}\{R_1(v)\} + \pi}{2\pi} \right] - v_{a1} \\ &= 2v_{a1} \Sigma(v) - v_{a1}, \end{aligned}$$

where  $\Sigma(v) = \frac{-\text{Arg}\{R_1(v)\}}{2\pi} + \frac{1}{2}$ . Note that  $\Sigma(v)$  is a sawtooth function with respect to the true

velocity as shown in Fig. E.4. Therefore,  $v_1(v)$  can be written using an alternate representation

for the sawtooth function as

$$v_1(v) = 2v_{a1} \text{frac} \left\{ \frac{v}{2v_{a1}} + \frac{1}{2} \right\} - v_{a1}, \quad (\text{E.5})$$

where  $\text{frac}\{x\}$  is the fractional part of  $x$  which is obtained by subtracting the integer part of  $x$

from  $x$ . A similar analysis can be done for  $v_2(v)$  to find

$$v_2(v) = 2v_{a2} \text{frac} \left\{ \frac{v + v_{a2}}{2v_{a2}} \right\} - v_{a2}. \quad (\text{E.6})$$

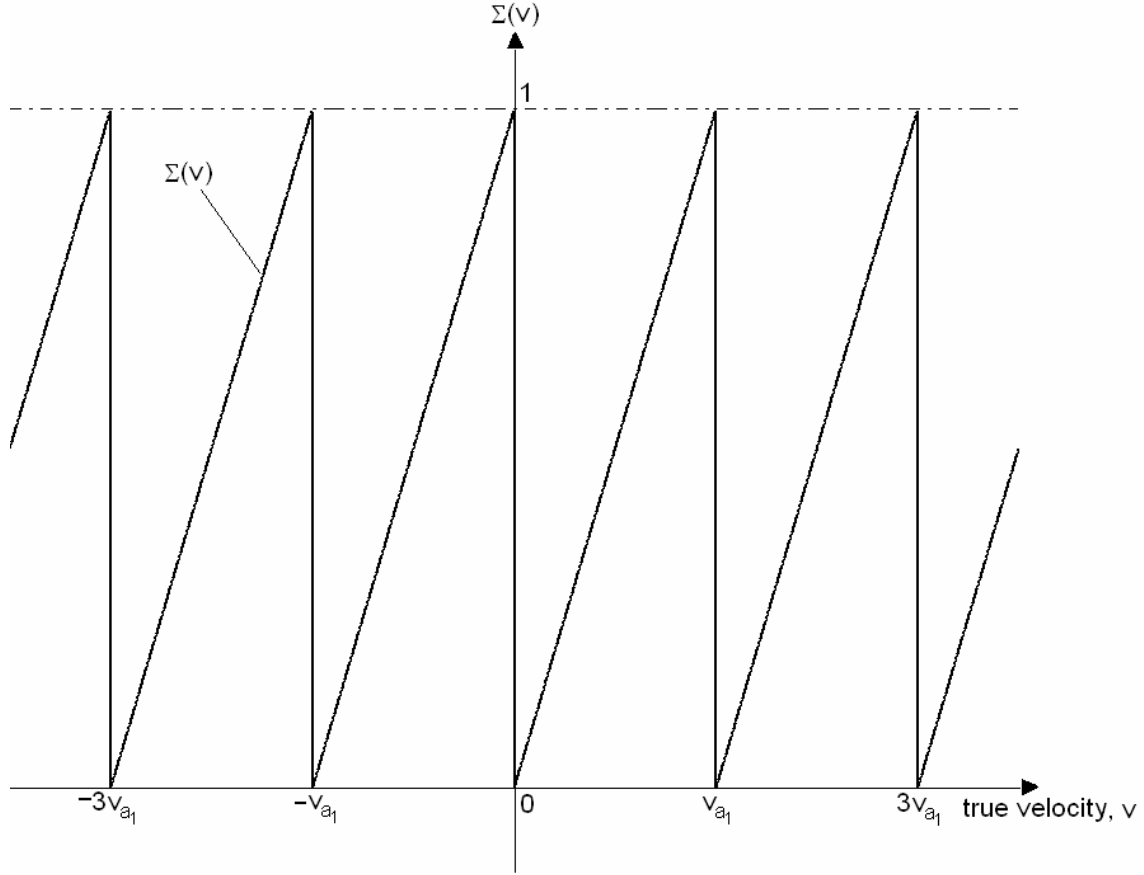


Fig. E.4.  $\Sigma(v)$  vs. the true velocity

The equation of the expected velocity difference transfer function is obtained by subtracting (E.6) from (E.5) as

$$(v_1 - v_2)(v) = v_1(v) - v_2(v),$$

$$(v_1 - v_2)(v) = v_{a2} - v_{a1} + 2v_{a1} \text{frac} \left\{ \frac{v + v_{a1}}{2v_{a1}} \right\} - 2v_{a2} \text{frac} \left\{ \frac{v + v_{a2}}{2v_{a2}} \right\}. \quad (\text{E.7})$$

Consider the case where the ratio  $T_1/T_2$  is a rational number (there is no loss of generality in doing this because  $T_1$  and  $T_2$  are always defined as multiples of a predetermined system clock unit). Let  $T_1/T_2 = m/n$  where  $m$  and  $n$  are relatively prime integers and  $1 \leq m < n$  because we assumed  $T_1 < T_2$ . Using the relation between the maximum unambiguous velocity and the PRT we get

$$\frac{T_1}{T_2} = \frac{v_{a2}}{v_{a1}} = \frac{m}{n}. \quad (\text{E.8})$$

By introducing (E.8) into (E.7), the expected velocity difference transfer function becomes

$$(v_1 - v_2)(v) = \left(1 - \frac{n}{m}\right)v_{a2} + 2\frac{n}{m}v_{a2} \text{frac} \left\{ \frac{v + \frac{n}{m}v_{a2}}{2\frac{n}{m}v_{a2}} \right\} - 2v_{a2} \text{frac} \left\{ \frac{v + v_{a2}}{2v_{a2}} \right\}.$$

Let's consider the transformation  $x = \frac{v}{v_{a2}}$  (since  $v$  is a real number,  $x$  is also a real number).

Then,

$$(v_1 - v_2)(v) = \frac{v_{a2}}{m} f(x), \quad (\text{E.9})$$

where  $f(x) = m - n + 2n \text{frac} \left\{ \frac{mx + n}{2n} \right\} - 2m \text{frac} \left\{ \frac{x + 1}{2} \right\}.$

According to (E.9), the properties of  $(v_1 - v_2)(v)$  will be immediately derived from those of  $f(x)$ . The next section focuses on the study of the function  $f(x)$  from a mathematical point of view.

### E.3.2. Properties of $f(x)$

Several properties of  $f(x)$  that are useful for the design of an efficient staggered PRT velocity dealiasing algorithm are presented here.

#### Periodicity

$f(x)$  is a  $2n$ -periodic function.

#### **Proof**

$$\begin{aligned} f(x+2n) &= m - n + 2n \operatorname{frac}\left\{\frac{m(x+2n)+n}{2n}\right\} - 2m \operatorname{frac}\left\{\frac{x+2n+1}{2}\right\} \\ &= m - n + 2n \operatorname{frac}\left\{\frac{mx+n}{2n} + m\right\} - 2m \operatorname{frac}\left\{\frac{x+1}{2} + n\right\} \\ &= m - n + 2n \operatorname{frac}\left\{\frac{mx+n}{2n}\right\} - 2m \operatorname{frac}\left\{\frac{x+1}{2}\right\}. \end{aligned}$$

Therefore,  $f(x+2n) = f(x)$ ; i.e.,  $f(x)$  is a  $2n$ -periodic function.

#### Discontinuity points

The discontinuity points of  $f(x)$  are induced by the third and fourth terms of  $f(x)$  due to the  $\operatorname{frac}$  function. Hence, there are two types of discontinuity points, those induced by the term  $\operatorname{frac}\left\{\frac{mx+n}{2n}\right\}$ , denoted by the set  $\{x_k^{(1)}\}$ , and those induced by the term  $\operatorname{frac}\left\{\frac{x+1}{2}\right\}$ , denoted by the set  $\{x_k^{(2)}\}$ , where  $k \in \mathbb{Z}$ .

Since  $f(x)$  is a  $2n$ -periodic function, let's consider  $f(x)$  only on the interval  $[-n, n)$ . Next, we will prove that

$$1) \quad x_k^{(1)} = (2k-1)\frac{n}{m}, \text{ where } k \in \left[ \frac{3-m}{2}, \frac{m-1}{2} \right] \text{ if } m \text{ is odd and } k \in \left[ \frac{2-m}{2}, \frac{m}{2} \right] \text{ if } m \text{ is even,}$$

$$2) \quad x_k^{(2)} = 2k-1, \text{ where } k \in \left[ \frac{3-n}{2}, \frac{n-1}{2} \right] \text{ if } n \text{ is odd and } k \in \left[ \frac{2-n}{2}, \frac{n}{2} \right] \text{ if } n \text{ is even, and}$$

3)  $\{x_k^{(1)}\} \cap \{x_k^{(2)}\} = \emptyset$ ; i.e., each  $x_k^{(1)}$  and each  $x_k^{(2)}$  define a unique discontinuity point and there are  $(m+n-2)$  discontinuity points if  $m$  and  $n$  are odd and  $(m+n-1)$  otherwise.

**Proof**

1) The discontinuity points of the term  $\text{frac}\left\{\frac{mx+n}{2n}\right\}$  appear if  $\text{frac}\left\{\frac{mx+n}{2n}\right\} = 0$ . This

equivalent to finding  $k \in \mathbb{Z}$  such that  $\frac{mx+n}{2n} = k$ . Then, these discontinuity points occur if

$$x = (2k-1)\frac{n}{m}. \text{ Thus, } x_k^{(1)} = (2k-1)\frac{n}{m}.$$

If  $m$  is odd, the smallest discontinuity point of the form  $x_k^{(1)}$  for  $f(x)$  restricted to  $[-n, n)$  is

$$\left(2\frac{3-m}{2}-1\right)\frac{n}{m} = -n + 2\frac{n}{m} \text{ and } \left(2\frac{2-m}{2}-1\right)\frac{n}{m} = -n + \frac{n}{m} \text{ if } m \text{ is even (since } -n \text{ is not a}$$

discontinuity point for  $f(x)$  restricted to  $[-n, n)$ , the smallest discontinuity point is the closest

discontinuity point to the right of  $-n$ ). Moreover, if  $m$  is odd, the largest discontinuity point of the

$$\text{form } x_k^{(1)} \text{ for } f(x) \text{ restricted to } [-n, n) \text{ is } \left(2\frac{m-1}{2}-1\right)\frac{n}{m} = n - 2\frac{n}{m} \text{ and } \left(2\frac{m}{2}-1\right)\frac{n}{m} = n - \frac{n}{m} \text{ if}$$

$m$  is even (since  $n$  is not a discontinuity point for  $f(x)$  restricted to  $[-n, n)$ , the largest discontinuity point is the closest discontinuity point to the left of  $n$ ). Therefore,

$$k \in \left[ \frac{3-m}{2}, \frac{m-1}{2} \right] \text{ if } m \text{ is odd and } k \in \left[ \frac{2-m}{2}, \frac{m}{2} \right] \text{ if } m \text{ is even.}$$

2) Similarly, the discontinuity points of the term  $\text{frac}\left\{\frac{x+1}{2}\right\}$  appear if  $\text{frac}\left\{\frac{x+1}{2}\right\} = 0$ .

This is equivalent to finding  $k \in \mathbb{Z}$  such that  $\frac{x+1}{2} = k$ . Then, these discontinuity points occur if

$$x = 2k - 1. \text{ Thus, } x_k^{(2)} = 2k - 1.$$

If  $n$  is odd, the smallest discontinuity point of the form  $x_k^{(2)}$  for  $f(x)$  restricted to  $[-n, n)$  is

$$2 \frac{3-n}{2} - 1 = -n + 2 \text{ and } 2 \frac{2-n}{2} - 1 = -n + 1 \text{ if } n \text{ is even (since } -n \text{ is not a discontinuity point for}$$

$f(x)$  restricted to  $[-n, n)$ , the smallest discontinuity point is the closest discontinuity point to

the right of  $-n$ ). Moreover, if  $n$  is odd, the largest discontinuity point of the form  $x_k^{(2)}$  for  $f(x)$

restricted to  $[-n, n)$  is  $2 \frac{n-1}{2} - 1 = n - 2$  and  $2 \frac{n}{2} - 1 = n - 1$  if  $n$  is even (since  $n$  is not a

discontinuity point for  $f(x)$  restricted to  $[-n, n)$ , the largest discontinuity point is the closest

discontinuity point to the left of  $n$ ). Therefore,  $k \in \left[ \frac{3-n}{2}, \frac{n-1}{2} \right]$  if  $n$  is odd and  $k \in \left[ \frac{2-n}{2}, \frac{n}{2} \right]$

if  $n$  is even.

3) Let's assume that there exist  $k$  and  $l$  such that  $x_k^{(1)} = x_l^{(2)}$ . This would imply that

$$(2k-1) \frac{n}{m} = 2l-1; \text{ i.e., } \frac{m}{n} = \frac{2k-1}{2l-1}. \text{ However, } |2k-1| < m \text{ (because } k \in \left[ \frac{3-m}{2}, \frac{m-1}{2} \right] \text{ if } m \text{ is}$$

odd and  $k \in \left[ \frac{2-m}{2}, \frac{m}{2} \right]$  if  $m$  is even) and the equation  $\frac{m}{n} = \frac{2k-1}{2l-1}$  is not possible since  $m$  and  $n$  are relatively prime integers. Therefore, each  $x_k^{(1)}$  and each  $x_k^{(2)}$  define a unique discontinuity point.

If  $m$  and  $n$  are odd, then there are  $\frac{m-1}{2} - \frac{3-m}{2} + 1 = m-1$  discontinuity points of the form  $x_k^{(1)}$  and  $\frac{n-1}{2} - \frac{3-n}{2} + 1 = n-1$  discontinuity points of the form  $x_k^{(2)}$ . Therefore, there are  $(m+n-2)$  discontinuity points for  $f(x)$  on  $[-n, n)$ .

If  $m$  is odd and  $n$  is even, then there are  $\frac{m-1}{2} - \frac{3-m}{2} + 1 = m-1$  discontinuity points of the form  $x_k^{(1)}$  and  $\frac{n}{2} - \frac{2-n}{2} + 1 = n$  discontinuity points of the form  $x_k^{(2)}$ . Therefore, there are  $(m+n-1)$  discontinuity points for  $f(x)$  on  $[-n, n)$ .

Similarly, if  $m$  is even and  $n$  is odd, there are  $(m+n-1)$  discontinuity points for  $f(x)$  on  $[-n, n)$ .

Note that  $m$  and  $n$  can not be both even since they are relatively prime.

Piecewise constant function

- 1)  $f(x)$  is a piecewise constant function.
- 2) For each discontinuity point  $x_k$ , where  $x_k \in \{x_k^{(1)}\} \cup \{x_k^{(2)}\}$ ,  $f(x_k) = f(x_k^+)$ . Hence, the values of  $f(x)$  are the values of  $f(x)$  at the discontinuity points.

**Proof**

- 1) Let  $x_k$  and  $x_l$  be two consecutive discontinuity points ( $x_k < x_l$ ). Let  $y \in (x_k, x_l)$ .

$$\begin{aligned} f(y) &= m - n + 2n \operatorname{frac}\left\{\frac{my+n}{2n}\right\} - 2m \operatorname{frac}\left\{\frac{y+1}{2}\right\} \\ &= m - n + my + n - 2p(y)n - my - m + 2q(y)m, \end{aligned}$$

where  $p(y) = \frac{my+n}{2n} - \operatorname{frac}\left\{\frac{my+n}{2n}\right\}$  and  $q(y) = \frac{y+1}{2} - \operatorname{frac}\left\{\frac{y+1}{2}\right\}$  are integers such that

$$0 < \frac{my+n}{2n} - p(y) < 1 \text{ and } 0 < \frac{y+1}{2} - q(y) < 1. \text{ Thus,}$$

$$f(y) = 2q(y)m - 2p(y)n. \tag{E.10}$$

The fraction  $\operatorname{frac}\left\{\frac{mx+n}{2n}\right\}$  is a piecewise continuous function. More specifically, it is continuous on  $(x_k, x_l)$ . Thus, the function  $\frac{mx+n}{2n} - \operatorname{frac}\left\{\frac{mx+n}{2n}\right\}$  is continuous on  $(x_k, x_l)$  as sum of continuous functions on  $(x_k, x_l)$ . Moreover, it takes only integer values (since the

fractional part of  $\frac{mx+n}{2n}$  is being subtracted to  $\frac{mx+n}{2n}$ ); therefore, this function is constant on  $(x_k, x_l)$ . Hence,  $p(y) = p$ , where  $p \in \mathbb{Z}$ .

Similarly,  $\text{frac}\left\{\frac{x+1}{2}\right\}$  is a piecewise continuous function. More specifically, it is continuous on  $(x_k, x_l)$ . Thus, the function  $\frac{x+1}{2} - \text{frac}\left\{\frac{x+1}{2}\right\}$  is continuous on  $(x_k, x_l)$  as sum of continuous functions on  $(x_k, x_l)$ . Moreover, it takes only integer values; therefore, this function is constant on  $(x_k, x_l)$ . Hence,  $q(y) = q$ , where  $q \in \mathbb{Z}$ .

Finally, (E.10) becomes

$$\forall y \in (x_k, x_l) \quad f(y) = 2qm - 2pn.$$

Hence, for  $x_k$  and  $x_l$  two consecutive discontinuity points,  $f(x)$  is constant on  $(x_k, x_l)$ . In other words,  $f(x)$  is a piecewise constant function.

2) Let's consider  $f(x)$  on  $[-n, n)$ . The function  $\text{frac}\left\{\frac{mx+n}{2n}\right\}$  is continuous on  $[x_k^{(1)}, x_{k+1}^{(1)})$  for each  $x_k^{(1)}$  and the function  $\text{frac}\left\{\frac{x+1}{2}\right\}$  is continuous on  $[x_k^{(2)}, x_{k+1}^{(2)})$  for each  $x_k^{(2)}$ . Therefore, for  $x_k$  a discontinuity point,  $f(x)$  is continuous on the right at  $x_k$ . Since  $f(x)$  is  $2n$ -periodic, this can be generalized to the whole real line; i.e., for  $x \in (-\infty, \infty)$ .

### Symmetry

$\forall x \in \mathbb{R} \setminus \{x_k^{(1)}\} \cup \{x_k^{(2)}\}$   $f(x)$  is an odd function of  $x$ .

### **Proof**

Let  $x \in \mathbb{R} \setminus \{x_k^{(1)}\} \cup \{x_k^{(2)}\}$ . Then,

$$f(-x) = m - n + 2n \operatorname{frac} \left\{ \frac{-mx + n}{2n} \right\} - 2m \operatorname{frac} \left\{ \frac{-x + 1}{2} \right\}.$$

Let  $q$  and  $r$  be the quotient and the remainder of the Euclidian division of  $(-mx + n)$  by  $2n$ , respectively.  $q$  is an integer and  $0 < r < 2n$  ( $r \neq 0$  since  $x$  is not a discontinuity point). Therefore,

$$2n \operatorname{frac} \left\{ \frac{-mx + n}{2n} \right\} = r = -mx + n - 2qn. \text{ Since } 0 < 2n - r < 2n \text{ and } 2n - r = mx + n + 2qn, -q \text{ and}$$

$2n - r$  are the quotient and the remainder of the Euclidian division of  $(mx + n)$  by  $2n$ ,

$$\text{respectively.} \quad \text{Therefore,} \quad 2n - r = 2n \operatorname{frac} \left\{ \frac{mx + n}{2n} \right\}; \quad \text{i.e.,}$$

$$2n - 2n \operatorname{frac} \left\{ \frac{-mx + n}{2n} \right\} = 2n \operatorname{frac} \left\{ \frac{mx + n}{2n} \right\}.$$

Similarly, it can be proved that  $2m - 2m \operatorname{frac} \left\{ \frac{-x + 1}{2} \right\} = 2m \operatorname{frac} \left\{ \frac{x + 1}{2} \right\}$ . Hence,

$$\begin{aligned} f(-x) &= m - n + 2n - 2n \operatorname{frac} \left\{ \frac{mx + n}{2n} \right\} - 2m + 2m \operatorname{frac} \left\{ \frac{x + 1}{2} \right\} \\ &= n - m - 2n \operatorname{frac} \left\{ \frac{mx + n}{2n} \right\} + 2m \operatorname{frac} \left\{ \frac{x + 1}{2} \right\}. \end{aligned}$$

Then,  $f(-x) = -f(x)$  and  $\forall x \in \mathbb{R} \setminus \{x_k^{(1)}\} \cup \{x_k^{(2)}\}$   $f(x)$  is an odd function of  $x$ .

### E.3.3. Values of the function

As proved in paragraph 3.2.3, the constant values of  $f(x)$  are the values of  $f(x)$  at the discontinuity points. Since  $f(x)$  is a  $2n$ -periodic function, all the different constant values of  $f(x)$  are the values of  $f(x)$  at all the discontinuity points in  $[-n, n)$ . Thus, there are three types of values

$$1) \quad y_k^{(1)} = f(x_k^{(1)}) = m - n - \text{mod}(2kn + m - n, 2m), \text{ where } k \in \left[ \frac{3-m}{2}, \frac{m-1}{2} \right] \text{ if } m \text{ is odd and}$$

$$k \in \left[ \frac{2-m}{2}, \frac{m}{2} \right] \text{ if } m \text{ is even,}$$

$$2) \quad y_k^{(2)} = f(x_k^{(2)}) = m - n + \text{mod}(2km + n - m, 2n), \text{ where } k \in \left[ \frac{3-n}{2}, \frac{n-1}{2} \right] \text{ if } n \text{ is odd and}$$

$$k \in \left[ \frac{2-n}{2}, \frac{n}{2} \right] \text{ if } n \text{ is even, and,}$$

$$3) \quad y^{(3)} = f(-n) = \begin{cases} m & \text{if } m \text{ is even and } n \text{ odd} \\ -n & \text{if } n \text{ is even and } m \text{ odd} \\ m-n & \text{if } m \text{ and } n \text{ odd} \end{cases}$$

The constant values of  $f(x)$  are integers.

**Proof**

1) Let's compute  $y_k^{(1)} = f(x_k^{(1)})$ . Then,

$$\begin{aligned} y_k^{(1)} &= m - n + 2n \operatorname{frac} \left\{ \frac{m(2k-1)\frac{n}{m} + n}{2n} \right\} - 2m \operatorname{frac} \left\{ \frac{(2k-1)\frac{n}{m} + 1}{2} \right\} \\ &= m - n + 2n \operatorname{frac} \{k\} - 2m \operatorname{frac} \left\{ \frac{2kn + m - n}{2m} \right\}. \end{aligned}$$

Hence, since  $\forall x, y \in \mathbb{Z} \operatorname{mod}(x, y) = y \operatorname{frac} \left\{ \frac{x}{y} \right\}$ ,  $y_k^{(1)} = m - n - \operatorname{mod}(2kn + m - n, 2m)$ .

2) Let's compute  $y_k^{(2)} = f(x_k^{(2)})$ . Then,

$$\begin{aligned} y_k^{(2)} &= m - n + 2n \operatorname{frac} \left\{ \frac{m(2k-1) + n}{2n} \right\} - 2m \operatorname{frac} \left\{ \frac{(2k-1) + 1}{2} \right\} \\ &= m - n + 2n \operatorname{frac} \left\{ \frac{2km + n - m}{2n} \right\} - 2m \operatorname{frac} \{k\}. \end{aligned}$$

Hence,  $y_k^{(2)} = m - n + \operatorname{mod}(2km + n - m, 2n)$ .

3) Let's compute  $y^{(3)} = f(-n)$ . Then,

$$\begin{aligned} y^{(3)} &= m - n + 2n \operatorname{frac} \left\{ \frac{-mn + n}{2n} \right\} - 2m \operatorname{frac} \left\{ \frac{-n + 1}{2} \right\} \\ &= m - n + 2n \operatorname{frac} \left\{ \frac{1 - m}{2} \right\} - 2m \operatorname{frac} \left\{ \frac{1 - n}{2} \right\} \\ &= \begin{cases} m - n + n & \text{if } m \text{ is even and } n \text{ odd} \\ m - n - m & \text{if } n \text{ is even and } m \text{ odd} \\ m - n & \text{if } m \text{ and } n \text{ odd} \end{cases}. \end{aligned}$$

$$\text{Hence, } y^{(3)} = \begin{cases} m & \text{if } m \text{ is even and } n \text{ odd} \\ -n & \text{if } n \text{ is even and } m \text{ odd} \\ m-n & \text{if } m \text{ and } n \text{ odd} \end{cases}$$

*E.3.4. Uniform spacing of the values*

- 1) The constant values of  $f(x)$  on  $[-n, n)$  are all different, and there are  $(m+n-1)$  values if  $m$  and  $n$  are odd and  $(m+n)$  otherwise. The absolute value of the difference between two constant values is higher or equal to 2.
- 2) The maximum value of  $f(x)$  is  $(m+n-2)$  if  $m$  and  $n$  are odd and  $(m+n-1)$  otherwise.
- 3) Since  $f(x)$  is odd, the minimum value of  $f(x)$  is  $-(m+n-2)$  if  $m$  and  $n$  are odd and  $-(m+n-1)$  otherwise. Therefore, since there are  $(m+n-1)$  constant values if  $m$  and  $n$  are odd and  $(m+n)$  values otherwise, the constant values of  $f(x)$  are evenly spaced by  $\Delta = 2$ .

***Proof***

1) Let's consider the difference between two constant values of  $f(x)$  on  $[-n, n)$ . There are five cases:

a) Let's consider the difference for two discontinuity points of the form  $x_k^{(1)}$ . Let  $k, l$  be integers in the interval  $\left[\frac{3-m}{2}, \frac{m-1}{2}\right]$  if  $m$  is odd or in the interval  $\left[\frac{2-m}{2}, \frac{m}{2}\right]$  if  $m$  is even,

with  $k \neq l$ . Then,

$$\begin{aligned}
\Delta_{k,l}^{(1)} &= y_k^{(1)} - y_l^{(1)} \\
&= [m - n - \text{mod}(2kn + m - n, 2m)] - [m - n - \text{mod}(2ln + m - n, 2m)] \\
&= -\text{mod}(2kn + m - n, 2m) + \text{mod}(2ln + m - n, 2m) \\
&= -(2kn + m - n - 2p_k m) + (2ln + m - n - 2p_l m),
\end{aligned}$$

where  $p_k$  and  $p_l$  are integers such that  $0 < 2kn + m - n - 2p_k m < 2m$  and

$$0 < 2ln + m - n - 2p_l m < 2m; \quad \text{i.e.,} \quad \frac{2k-1}{2} \frac{n}{m} - \frac{1}{2} < p_k < \frac{2k-1}{2} \frac{n}{m} + \frac{1}{2} \quad \text{and}$$

$$\frac{2l-1}{2} \frac{n}{m} - \frac{1}{2} < p_l < \frac{2l-1}{2} \frac{n}{m} + \frac{1}{2}. \quad \text{Since } p_k \text{ and } p_l \text{ are integers, } p_k = \left\lfloor \frac{2k-1}{2} \frac{n}{m} + \frac{1}{2} \right\rfloor \text{ and}$$

$$p_l = \left\lfloor \frac{2l-1}{2} \frac{n}{m} + \frac{1}{2} \right\rfloor, \text{ where } \lfloor x \rfloor \text{ indicates the integer part of } x. \text{ Therefore,}$$

$$\Delta_{k,l}^{(1)} = 2[(l-k)n + (p_k - p_l)m].$$

Thus, the values of  $\Delta_{k,l}^{(1)}$  are even integers. Moreover, if  $m$  is odd,  $(k-l) \in [2-m, m-2] \setminus \{0\}$  and

$$(p_k - p_l) \in \left[ (2-m) \frac{n}{m} - 1, (m-2) \frac{n}{m} + 1 \right]. \quad \text{If } m \text{ is even, } (k-l) \in [1-m, m-1] \setminus \{0\} \text{ and}$$

$$(p_k - p_l) \in \left[ (1-m) \frac{n}{m} - 1, (m-1) \frac{n}{m} + 1 \right].$$

Let's assume there exist  $k$  and  $l$  such that  $\Delta_{k,l}^{(1)} = 0$ . In that case,  $(l-k)n + (p_k - p_l)m = 0$ ; i.e.,

$$\frac{p_k - p_l}{k - l} = \frac{n}{m}. \quad \text{However, } |k - l| < m \text{ and the equation } \frac{p_k - p_l}{k - l} = \frac{n}{m} \text{ is not possible since } m \text{ and } n$$

are relatively prime integers. Since  $\Delta_{k,l}^{(1)}$  are even integers,  $\forall k, l \quad |\Delta_{k,l}^{(1)}| \geq 2$ .

b) Let's consider the difference for two discontinuity points of the form  $x_k^{(2)}$ . Let  $k, l$  be integers in the interval  $\left[\frac{3-n}{2}, \frac{n-1}{2}\right]$  if  $n$  is odd or in the interval  $\left[\frac{2-n}{2}, \frac{n}{2}\right]$  if  $n$  is even, with  $k \neq l$ . Then,

$$\begin{aligned}\Delta_{k,l}^{(2)} &= y_k^{(2)} - y_l^{(2)} \\ &= \left[ m - n + \text{mod}(2km + n - m, 2n) \right] - \left[ m - n + \text{mod}(2lm + n - m, 2n) \right].\end{aligned}$$

Therefore,  $\Delta_{k,l}^{(2)} = 2\left[(k-l)m + (q_l - q_k)n\right]$  with  $q_k = \left\lfloor \frac{2k-1}{2} \frac{m}{n} - \frac{1}{2} \right\rfloor$  and  $q_l = \left\lfloor \frac{2l-1}{2} \frac{m}{n} - \frac{1}{2} \right\rfloor$ .

Thus, the values of  $\Delta_{k,l}^{(2)}$  are also even integers. Moreover, if  $n$  is odd,  $(k-l) \in [2-n, n-2] \setminus \{0\}$

and  $(q_k - q_l) \in \left[ (2-n)\frac{m}{n} - 1, (n-2)\frac{m}{n} + 1 \right]$ . If  $n$  is even,  $(k-l) \in [1-n, n-1] \setminus \{0\}$  and

$$(q_k - q_l) \in \left[ (1-n)\frac{m}{n} - 1, (n-1)\frac{m}{n} + 1 \right].$$

Let's assume there exist  $k$  and  $l$  such that  $\Delta_{k,l}^{(2)} = 0$ . In that case,  $(k-l)m + (q_l - q_k)n = 0$ ; i.e.,

$\frac{q_k - q_l}{k-l} = \frac{m}{n}$ . However,  $|k-l| < n$  and the equation  $\frac{q_k - q_l}{k-l} = \frac{m}{n}$  is not possible since  $m$  and  $n$  are

relatively prime integers. Since  $\Delta_{k,l}^{(2)}$  are even integers,  $\forall k, l \quad \left| \Delta_{k,l}^{(2)} \right| \geq 2$ .

c) Let's consider the difference for two discontinuity points, one of the form  $x_k^{(1)}$ , and the other of the form  $x_k^{(2)}$ . Let  $k$  be an integer in the interval  $\left[\frac{3-m}{2}, \frac{m-1}{2}\right]$  if  $m$  is odd or in the

interval  $\left[\frac{2-m}{2}, \frac{m}{2}\right]$  if  $m$  is even, and  $l$  be an integer in the interval  $\left[\frac{3-n}{2}, \frac{n-1}{2}\right]$  if  $n$  is odd or

in the interval  $\left[\frac{2-n}{2}, \frac{n}{2}\right]$  if  $n$  is even.

$$\begin{aligned}\Delta_{k,l}^{(3)} &= y_k^{(1)} - y_l^{(2)} \\ &= \left[ m - n - \text{mod}(2kn + m - n, 2m) \right] - \left[ m - n + \text{mod}(2lm + n - m, 2n) \right] \\ &= -\text{mod}(2kn + m - n, 2m) - \text{mod}(2lm + n - m, 2n) .\end{aligned}$$

Since  $0 < \text{mod}(2kn + m - n, 2m) < 2m$  and  $0 < \text{mod}(2lm + n - m, 2n) < 2n$ ,  $\Delta_{k,l}^{(3)} \leq -1 - 1 = -2$ .

Therefore,  $\forall k, l \quad \left| \Delta_{k,l}^{(3)} \right| \geq 2$ .

d) Let's consider the difference between the values of  $f(x)$  at one discontinuity point of the form  $x_k^{(1)}$  and  $y_l^{(3)}$ . Let  $k$  be an integer in the interval  $\left[\frac{3-m}{2}, \frac{m-1}{2}\right]$  if  $m$  is odd or in the interval  $\left[\frac{2-m}{2}, \frac{m}{2}\right]$  if  $m$  is even. Let's compute  $\Delta_k^{(4)} = y_k^{(1)} - y^{(3)}$  considering several cases for the parity of  $m$  and  $n$ .

- If  $m$  is even and  $n$  odd,

$$\Delta_k^{(4)} = m - n - \text{mod}(2kn + m - n, 2m) - m .$$

Thus,  $\Delta_k^{(4)} = -n - \text{mod}(2kn + m - n, 2m) \leq -2$  since  $0 < \text{mod}(2kn + m - n, 2m) < 2m$ . Therefore,

$\forall k \quad \left| \Delta_k^{(4)} \right| \geq 2$ .

- If  $n$  is even and  $m$  odd,

$$\begin{aligned}
\Delta_k^{(4)} &= m - n - \text{mod}(2kn + m - n, 2m) + n \\
&= m - \text{mod}(2kn + m - n, 2m) \\
&= m - 2kn - m + n + 2p_k m \\
&= (1 - 2k)n + 2p_k m,
\end{aligned}$$

with  $p_k = \left\lfloor \frac{2k-1}{2} \frac{n}{m} - \frac{1}{2} \right\rfloor$ . Since  $n$  is even,  $\Delta_k^{(4)}$  are even integers. Let's assume there exists  $k$

such that  $\Delta_k^{(4)} = 0$ . In that case,  $\frac{2p_k}{2k-1} = \frac{n}{m}$ . However,  $|2k-1| < m$  and the equation  $\frac{2p_k}{2k-1} = \frac{n}{m}$

is not possible since  $m$  and  $n$  are relatively prime integers. Since  $\Delta_k^{(4)}$  are even integers,

$$\forall k \quad \left| \Delta_k^{(4)} \right| \geq 2.$$

- If  $m$  and  $n$  are odd,

$$\begin{aligned}
\Delta_k^{(4)} &= m - n - \text{mod}(2kn + m - n, 2m) - m + n \\
&= -2kn - m + n + 2p_k m \\
&= (1 - 2k)n + (2p_k - 1)m,
\end{aligned}$$

with  $p_k = \left\lfloor \frac{2k-1}{2} \frac{n}{m} - \frac{1}{2} \right\rfloor$ . Since  $m$  and  $n$  are odd,  $\Delta_k^{(4)}$  are even integers. Let's assume there

exists  $k$  such that  $\Delta_k^{(4)} = 0$ . In that case,  $\frac{2p_k - 1}{2k-1} = \frac{n}{m}$ . However,  $|2k-1| < m$  and the equation

$\frac{2p_k - 1}{2k-1} = \frac{n}{m}$  is not possible since  $m$  and  $n$  are relatively prime integers. Since  $\Delta_k^{(4)}$  are even

integers,  $\forall k \quad \left| \Delta_k^{(4)} \right| \geq 2$ .

e) Let's consider the difference between the values of  $f(x)$  at one discontinuity point of the form  $x_k^{(2)}$  and  $y^{(3)}$ . Let  $k$  be an integer in the interval  $\left[\frac{3-n}{2}, \frac{n-1}{2}\right]$  if  $n$  is odd or in the interval  $\left[\frac{2-n}{2}, \frac{n}{2}\right]$  if  $n$  is even. Let's compute  $\Delta_k^{(5)} = y_k^{(2)} - y^{(3)}$  considering several cases for the parity of  $m$  and  $n$ .

- If  $m$  is even and  $n$  odd,

$$\begin{aligned}\Delta_k^{(5)} &= m - n + \text{mod}(2km + n - m, 2n) - m \\ &= -n + \text{mod}(2km + n - m, 2n) \\ &= -n + 2km + n - m - 2q_k n \\ &= (2k - 1)m - 2q_k n ,\end{aligned}$$

with  $q_k = \left\lfloor \frac{2k-1}{2} \frac{m}{n} - \frac{1}{2} \right\rfloor$ . Since  $m$  is even,  $\Delta_k^{(5)}$  are even integers. Let's assume there exists  $k$

such that  $\Delta_k^{(5)} = 0$ . In that case,  $\frac{2q_k}{2k-1} = \frac{m}{n}$ . However,  $|2k-1| < n$  and the equation  $\frac{2q_k}{2k-1} = \frac{m}{n}$  is

not possible since  $m$  and  $n$  are relatively prime integers. Since  $\Delta_k^{(5)}$  are even integers,

$$\forall k \quad \left| \Delta_k^{(5)} \right| \geq 2.$$

- If  $n$  is even and  $m$  odd,

$$\Delta_k^{(5)} = m - n + \text{mod}(2km + n - m, 2n) + n.$$

Thus,  $\Delta_k^{(5)} = m + \text{mod}(2km + n - m, 2n) \geq 2$  since  $0 < \text{mod}(2km + n - m, 2n) < 2n$ . Therefore,

$$\forall k \quad \left| \Delta_k^{(5)} \right| \geq 2.$$

- If  $m$  and  $n$  are odd,

$$\begin{aligned}
\Delta_k^{(5)} &= m - n + \text{mod}(2km + n - m, 2n) - m + n \\
&= 2km + n - m - 2q_k n \\
&= (2k - 1)m - (2q_k - 1)n,
\end{aligned}$$

with  $q_k = \left\lfloor \frac{2k-1}{2} \frac{m}{n} - \frac{1}{2} \right\rfloor$ . Since  $m$  and  $n$  are odd,  $\Delta_k^{(5)}$  are even integers. Let's assume there

exists  $k$  such that  $\Delta_k^{(5)} = 0$ . In that case,  $\frac{2q_k - 1}{2k - 1} = \frac{m}{n}$ . However,  $|2k - 1| < n$  and the equation

$\frac{2q_k - 1}{2k - 1} = \frac{m}{n}$  is not possible since  $m$  and  $n$  are relatively prime integers. Since  $\Delta_k^{(5)}$  are even

integers,  $\forall k \quad |\Delta_k^{(5)}| \geq 2$ .

From (a), (b), (c), (d) and (e), the constant values of  $f(x)$  on  $[-n, n)$  are all different and the absolute value of the difference between two constant values is higher or equal to 2.

2) Let's determine the maximum value of  $f(x)$ .

The maximal possible value for  $y_k^{(2)}$  is obtained if  $\text{mod}(2km + n - m, 2n) = 2n - 1$ . In that case,

$y_k^{(2)} = m + n - 1$ . Is there really any  $k \in \mathbb{Z}$  such that  $\text{mod}(2km + n - m, 2n) = 2n - 1$ ? The

following equivalences are true;

$$\exists k \in \mathbb{Z} / \text{mod}(2km + n - m, 2n) = 2n - 1$$

$$\Leftrightarrow \exists k, q \in \mathbb{Z} / 2km + n - m = 2qn + 2n - 1$$

$$\Leftrightarrow \exists k, q \in \mathbb{Z} / (1 - 2k)m + (2q + 1)n = 1.$$

Therefore, the goal is to find  $k, q \in \mathbb{Z}$  such that

$$(1-2k)m+(2q+1)n=1, \tag{E.11}$$

that is, to find odd integers  $A$  and  $B$  such that  $Am+Bn=1$ .

A corollary of the Fundamental Theorem of Arithmetic for  $m$  and  $n$  relatively prime integers assures the existence of  $C$  and  $D$  integers such that  $Cm+Dn=1$ .

Let's assume  $m$  odd and  $n$  even. In that case, since  $Dn$  is even,  $C$  is odd for the equation  $Cm+Dn=1$  to be true; but  $D$  can be either even or odd. However, there exist  $A$  and  $B$  odd integers such that  $Am+Bn=1$  (if  $D$  is odd, let's take indeed  $\begin{cases} A=C \\ B=D \end{cases}$  and  $\begin{cases} A=C+n \\ B=D-m \end{cases}$  if  $D$  is even).

Let's assume now  $m$  even and  $n$  odd. In that case, since  $Cm$  is even,  $D$  is odd for the equation  $Cm+Dn=1$  to be true; but  $C$  can be either even or odd. However, there exist  $A$  and  $B$  odd integers such that  $Am+Bn=1$  (if  $C$  is odd, let's take indeed  $\begin{cases} A=C \\ B=D \end{cases}$  and  $\begin{cases} A=C+n \\ B=D-m \end{cases}$  if  $C$  is even).

Thus, if  $m$  is odd and  $n$  is even or if  $m$  is even and  $n$  is odd, there exist  $A$  and  $B$  odd integers such that  $Am+Bn=1$ . Therefore, there exist  $k, q \in \mathbb{Z}$  such that (E.11) is true ( $k = \frac{1-A}{2}$  and  $q = \frac{B-1}{2}$ ). Ultimately, if  $m$  is odd and  $n$  is even or if  $m$  is even and  $n$  is odd, there exists  $k \in \mathbb{Z}$

such that  $y_k^{(2)} = m+n-1$ . Moreover,  $\forall l \in \mathbb{Z} \quad m+n-1 > y_l^{(1)}$  (since

$0 < \text{mod}(2kn + m - n, 2m) < 2m$ ) and  $m + n - 1 > y^{(3)}$ . Thus, the maximum value of  $f(x)$  is  $(m + n - 1)$  if  $m$  is odd and  $n$  is even or if  $m$  is even and  $n$  is odd.

If  $m$  and  $n$  are odd, (E.11) is never true. Therefore, if  $m$  and  $n$  are odd, the maximum possible value for  $y_k^{(2)}$  is obtained if  $\text{mod}(2km + n - m, 2n) = 2n - 2$ . In that case,  $y_k^{(2)} = m + n - 2$ . Is there really any  $k \in \mathbb{Z}$  such that  $\text{mod}(2km + n - m, 2n) = 2n - 2$ ? The following equivalences are true;

$$\begin{aligned} & \exists k \in \mathbb{Z} / \text{mod}(2km + n - m, 2n) = 2n - 2 \\ & \Leftrightarrow \exists k, q \in \mathbb{Z} / 2km + n - m = 2qn + 2n - 2 \\ & \Leftrightarrow \exists k, q \in \mathbb{Z} / (1 - 2k)m + (2q + 1)n = 2. \end{aligned}$$

Therefore, the goal is to find  $k, q \in \mathbb{Z}$  such that

$$(1 - 2k)m + (2q + 1)n = 2, \quad (\text{E.12})$$

that is, to find odd integers  $A$  and  $B$  such that  $Am + Bn = 2$ .

A corollary of the Fundamental Theorem of Arithmetic for  $m$  and  $n$  relatively prime integers assures the existence of  $C$  and  $D$  integers such that  $Cm + Dn = 1$ ; i.e.,  $2Cm + 2Dn = 2$ . The problem is that  $2C$  and  $2D$  are even. However, there exist  $A$  and  $B$  odd integers such that

$Am + Bn = 2$  ( $\begin{cases} A = 2C + n \\ B = 2D - m \end{cases}$  for example). Therefore, there exist  $k, q \in \mathbb{Z}$  such that (E.12) is true

$(k = \frac{1 - A}{2}$  and  $q = \frac{B - 1}{2})$ . Thus, if  $m$  and  $n$  are odd, there exists  $k \in \mathbb{Z}$  such that  $y_k^{(2)} = m + n - 2$ .

Moreover,  $\forall l \in \mathbb{Z} \quad m+n-2 > y_l^{(1)}$  (since  $0 < \text{mod}(2kn+m-n, 2m) < 2m$ ) and  $m+n-2 > y^{(3)}$ .

Thus, the maximum value of  $f(x)$  is  $(m+n-2)$  if  $m$  and  $n$  are odd.

#### E.4. Characteristics of the expected velocity difference transfer function

Equation (E.9) can be used to derive the characteristics of  $(v_1 - v_2)(v)$  from those of  $f(x)$ . The

most interesting properties of  $(v_1 - v_2)(v)$  are listed below.

If  $\frac{T_1}{T_2} = \frac{m}{n}$  where  $m$  and  $n$  are relatively prime integers and  $T_1 < T_2$ , then

- 1)  $(v_1 - v_2)(v)$  is a  $2nv_{a2}$ -periodic ( $2mv_{a1}$ -periodic) function.
- 2)  $(v_1 - v_2)(v)$  is a piecewise constant function. There are two types of discontinuity points on  $[-nv_{a2}, nv_{a2})$ 
  - $v_k^{(1)} = (2k-1)v_{a1}$ , where  $k \in \mathbb{Z}$ ,  $k \in \left[\frac{3-m}{2}, \frac{m-1}{2}\right]$  if  $m$  is odd and  $k \in \left[\frac{2-m}{2}, \frac{m}{2}\right]$  if  $m$  is even, and
  - $v_k^{(2)} = (2k-1)v_{a2}$ , where  $k \in \mathbb{Z}$ ,  $k \in \left[\frac{3-n}{2}, \frac{n-1}{2}\right]$  if  $n$  is odd and  $k \in \left[\frac{2-n}{2}, \frac{n}{2}\right]$  if  $n$  is even.

Moreover,  $\{v_k^{(1)}\} \cap \{v_k^{(2)}\} = \emptyset$ ; i.e., each  $v_k^{(1)}$  and  $v_k^{(2)}$  define a unique discontinuity point on  $[-nv_{a2}, nv_{a2})$ . There are  $(m+n-2)$  discontinuity points on  $[-nv_{a2}, nv_{a2})$  if  $m$  and  $n$  are odd and  $(m+n-1)$  otherwise.

3)  $(v_1 - v_2)(v)$  is an odd function of the true velocity  $v$  for all  $v \in \mathbb{R} \setminus \{v_k, k \in \mathbb{Z}\}$ , where  $\{v_k, k \in \mathbb{Z}\}$  is the set of the discontinuity points of  $(v_1 - v_2)(v)$ .

4) The constant values of  $(v_1 - v_2)(v)$  on  $[-nv_{a2}, nv_{a2})$  are all different and are evenly spaced by  $\Delta = 2 \frac{v_{a2}}{m} \left( \Delta = 2 \frac{v_{a1}}{n} \right)$ . There are  $(m+n-1)$  constant values if  $m$  and  $n$  are odd and  $(m+n)$  otherwise.

5) The maximum value of  $(v_1 - v_2)(v)$  is  $\frac{v_{a2}}{m}(m+n-2)$  if  $m$  and  $n$  are odd and  $\frac{v_{a2}}{m}(m+n-1)$  otherwise.



## **Appendix F. Staggered PRT Algorithm (AEL description)**

The following is the algorithm enunciation language description of the proposed staggered PRT algorithm with DC removal in lieu of ground clutter filter. This algorithm has been implemented and tested in real-time on NSSL's KOUN radar in Norman, OK.

